**UNIVERSIDAD AUTÓNOMA DE MADRID**

**FACULTAD DE CIENCIAS**

**DEPARTAMENTO DE FÍSICA DE MATERIALES**


# Contrast agents for cardiovascular optical imaging at molecular level

## Doctor thesis

Jie Hu

Madrid, 2018

**UNIVERSIDAD AUTÓNOMA DE MADRID**

**FACULTAD DE CIENCIAS**

**DEPARTAMENTO DE FÍSICA DE MATERIALES**


# Contrast agents for cardiovascular optical imaging at molecular level

## Doctor thesis

Jie Hu

Supervisor:

Prof. JOSÉ GARCÍA SOLÉ

Dr. EMMA MARTÍN RODRÍGUEZ

Tutor:

Prof. DANIEL JAQUE GARCÍA

Doctor program:

Física de la Luz y la Materia

Madrid, June, 2018

To my parents

# Acknowledgements

Like Camino de Santiago, you finished your camino when you arrived at Catedral de Santiago de Compostela, but the end is not there, the end is in the west of the mainland, where you can see the sunset on the sea…

During these three years, I have learned a lot about optics, such as light source, objectors, mirrors, lenses, filters, CCD and InGaAs detector. In addition, some knowledge about cells, arteries and animals. Thanks for the FIG members helping me to learn these things. Even more, I have seen the cardiovascular surgery in human bodies. I cann't forget the moment, when Pepe, Dani and me were in hospital to do my first work on cardiovascular disease. At that moment, we didn't know how to do the experiment, we just kept discussing with the doctors and playing with gold nanoparticle and OCT catheter. That was the first time I stayed in the surgery room, and played with clinical techniques. I want to say the first step of my Ph.D was started from there, and that experience keep me going on and on in cardiovascular disease.

Foremost, I would like to thank my supervisor Dani, who made my dream to study abroad come ture, and makes this thesis a possibility. I am very appreciate him for teaching me how to do experiments, analyze data and draw sexy figures. He is the man who helps me to get new samples to do research, always pushes me to work and stays in the lab work with me. I still remember his effort in helping me to get collaboration with other groups, providing me such amount of opportunities to attend conferences, and encouraging me to talk with other researchers. Sometimes, we went to the right place but wrong conference, he said I deserved to enjoy the scenery and relax. In case of football, he is a fans of Atlético Madrid, but he also supports my team Real Madrid. I never forgot the time we watched the final Champions League between Real Madrid and Liverpool on the plane in Poland.

I also thank my co-supervisor Pepe, for untiring discussions about theory and data analyses, and effort in improving my oral presentation. I want thanks him for carefully revising my thesis, and I have learned a lot in writing. I remember for the first work, we have good results, but we didn't know how to analyze them, and what is the main focus of that work. He kept giving me the ideas

to deal with those data. In the discussion about gold nanoshells for cells imaging, we didn't know what were the red spots in the HeLa cells, and how the incubation time affected the number of GNSs in HeLa cells. We have done a lot of work, but the results were still not very good, and we didn't know what was the next step, at that moment, we lost temper. But finally we got the paper published in *Nano Research*. Then I learnt how to take the responsibility to do the experiment, and from then on, strangely, I prefer to have an argument with him, because I know, only in this way, I can learn things. As we know, he is a Madridista and he likes football very much. I cann't forget the precious moment I played football with him in the field, and also the moment I watched the Champions league between Real Madrid and PSG at his house. He was so kind, and often, he lent me his season card to watch La Liga in Santiago Bernabéu stadium. You can not imagine the jealous from my friends.

My sincerest thanks extend to my co-supervisor Emma, she is such a nice woman, without her help, the thesis would be impossible. She spent almost all the time to take care of my thesis. It was her who always came my office, and gave me intellectual suggestions on writing the thesis. At this moment, I would like to thanks her husband, Dirk. Both of them teach me how to do the synthesis, this would be helpful for my future. Without helping from them, the functionalization of nanoparticles for bioapplication would be impossible. Thanks them for colorful topics in every day's coffee time, we shared photos, we discussed what our plan for the weekend and what are places of interests to visit. Sometimes, we complained about the long under review time for a paper. Thanks them and their family for the invaluable gift for my birthday from Netherland, they always made me feel working at home. I really like their daughter, Almudela, who is almost 1 year old and with big blue eyes. Every time, she appears in our office, it seems the angle is there, you cann´t pay no attention to her, she always make your life much more relax. I remember there was a day, when I said goodbye to her, she feels very sad, I don´t know if it will happen again when I leave here.

I would also like to thank Patri, actually I would like to say she is my professional optical technique. She helped me to build dark field microscopy setup. Every time when I didn´t know how to solve the problem in Andor, she always known how to manage it. I cann´t forget the bad thing I did, the first day when I was in the lab, I left the lab without switching off the Ti: Sapphire, and she helped me to switch it off. From then on, I started try to build a good habit in doing

experiment. She is very good at in sport activities, and she pushed me to practice Karate. Now I am much more stronger than before.

I thank Lucía for listening my complains and encouraging me all the time. Without sharing the experience with you, I will be completely lost in doing research. In particularly, she is my translator in the lab, it seems only she can understand my Chinese-English. Indeed, I also thanks for her kind remind in organizing everything, and make things much easier in the lab. I want to mention the medieval festival we went in Alcalá de Henares, that was my first time to visit a place with foreign friends, thanks for her interesting instruction about the history and delicious food there.

I want to thank Paloma, she is a girl who works very hard and almost the last one left the lab, and she never complains. I always take her as an example and encourage myself to work like her.

I thank Paco for offering me the cells to do the experiment, without these cells, *in vitro* experiment would be impossible. I remember the first time we used OCT catheter to detect HeLa cells, which was an unexpected finding, and makes my thesis much more interesting now.

I also thank to Nuria for offering me the arteries to do the *ex vivo* experiment. She was always available whenever Dani ask her to provide the arteries.

I would like to express my gratitude to all current and former members of FIG group, in particular, Harrison, Ruiyun. Blanca, Antonio, Erving and Uéslen, thanks for their kind help. They made my life much more easier than expected.

I thank to David and Alejandro, who have shared the office with me. They are so kind heart guys and always give me a hand when I was suffering. They always smile, bring the light to me, and make me happy. Fortunately, we have shared a good moment in the football field.

I am also very grateful to our collaborators. Thanks Dr. Fernando Rivero, Dr. Río Aguilar Torres and Prof. Fernando Alfonso (Hospital Universitario de la Princesa) for providing us the OCT equipment, and pushing us to keep on through time to time of meetings. Thanks Prof. Pilar Rivera Gil, Paula and Dr. Dionysia Tsoutsi (Universitat Pompeu Fabra) for providing us gold nanostars, and teaching me how to do flowing experiment. Thanks José A. Sánchez-Gil and Diego Romero (Instituto de Estructura de la Materia (IEM-CSIC)) for providing the simulation data of extinction,

scattering and absorption spectra of gold nanoparticles. Thanks Prof. Horacio Lamela Rivera, Dr Luca llegio, and Dr Daniel Gallego (Universidad Carlos III de Madrid) for their help in doing photoacoustic experiment.

I would like to thank my football team in Getafe and UAM, and my basketball team in UAM. Thanks them for making my spare time much more interesting. These famous players in football teams are Tian Bing, Ye Tang Ye, Zhang Lu, Deng Xiangxing, Li Wenda, and Wu Beilun. In basketball teams, they are Yansheng, Liu Jian, Huayu, Qinglong, Tiancun, Xiyan, Shaoliang, Zhaoyu, Lizhi, Li Chuan, Yuwen, Gaole, Ingyu, Yuhao and Xuejun. I would like to thanks my classmates who were also supported by CSC, we have a very good memory during my Ph.D studies. They are Li Xiong, Jinbao, Yuyang, Chen Yu, Jingya, Fu Can. Particularly, I would like to thanks Deng Xiangxing, who should be mentioned above. He is my good friend, we have many nice trips and we always encourage each other to work hard. I also want to thank Junqing, Longfei and Yukun, we have enjoyed a lot of Chinese restaurant in Madrid and shared the experience in finding a job. I want to extend my grateful to my friends in China, who always take care of me, and enjoy the sceneries I shared with them, and shared their colorful life with me, they are Wang Han, Huang Jianhui, Gong Guoliang, Lu Dasheng, Chen Sijie, Han Xuequn, Wang Zhenqiang, Zhang Jifa, Du Binbin…

Thanks to all the foundations for supporting my life and study during these three years. They are the Ph.D grant from China Scholarship Council (CSC, No. 201506650003) and Spanish Ministerio de Economía y Competitividad under Project (No. MAT2016-75362-C3-1-R).

Finally, I want to thanks my family. It has been for 10 years since I sat in the classroom, and attent the college entrance examination. At that time, I promised to myself that I need to finish the exam very well in order to attend a good university and then I can support my family. But 10 years later, I am still a student, and I cann't do anything for my family. They always support me without any conditions. When they were suffering, they tried to avoid to tell me in order to make my focus on the study. Especially this year, all of them are suffereing injury in their left hands, and cann't work for a long time. Due to lack of money, my father has to go back to work without total recovery, and my mother has to stay at home and make food for herself. I can not imagine what is the situation now with my parents, and I can do nothing for them. They never complain it to me and

just keep asking me to focus on experiment and thesis. Thanks for my sister and sister in law to take care of them, and supporting my study abroad. Thanks for my nephew, he is the guy who always make me happy. I would like to thanks my grandma, when I was a child, it was her who got up very early and prepared the breakfast for me. Even she was dead, she is still aliving in my heart.

To all of you, thanks.

# Contents

# Summary

In this thesis, contrast agents for cardiovascular optical imaging at molecular level have been investigated. The investigation is mainly based on intravascular optical coherence tomography (IV-OCT), and the combination of IV-OCT and fluorescence imaging. Cardiovascular disease is the main cause of the death in the world. Until now, IV-OCT as an minimally invasive technique has been used for *in vivo* evaluation of unstable plaque in atherosclerosis and stent placement. The development of nanometric contrast agents for IV-OCT would help to visualize the atherosclerosis process at molecular level. By combining the IV-OCT with fluorescence imaging, the contrast agent would be fully used and provide a high resolution of cardiovascular imaging.

First, the contrast enhancement provided by different kind of gold nanoparticles have been investigated by IV-OCT. The function of IV-OCT is determined by the static and pull back option in IV-OCT system. IV-OCT allows the detection of single gold nanoparticles due to its high sensitivity.

Second, due to the IV-OCT signal is based on the scattering ability of the sample, the scattering properties of gold nanoshells (GNSs), nanorods, and nanostars have been systematically investigated by numerical simulation, photo-thermal method, infrared dark field microscopy, photoacoustic and IV-OCT. GNSs have been determined to be a good scatterers for IV-OCT.

Third, the GNSs as contrast for cell and tissue imaging by IV-OCT have been investigated. The incubation of GNSs in HeLa and Jurkat cells produced a high OCT contrast enhancement. The internalized of GNSs in these cells have been confirmed by dark field microscopy and TEM. A OCT contrast enhancement after injected of GNSs in tissue is also obtained.

Finally, the quantum dots (QDs) which can be excited by IV-OCT laser and show an emission in third biological window have been investigated. Due to the high sensitivity of IV-OCT, these QDs also give OCT contrast enhancement. The QDs used for OCT and fluorescence dual imaging

has been systematically investigated in colloidal, tissue and in the artery. From the fluorescence imaging of QDs excited by the pull-back IV-OCT laser could provide the morphology of artery.

In conclude, the investigated GNSs and QDs would be very useful for cardiovascular optical imaging at molecular level. The functionalization of these nanoparticles would make them specially target to the cardiovascular disease site, and provide a high resolution imaging for visualization of atherosclerosis process.

Key words: cardiovascular disease, atherosclerosis plaque, IV-OCT, fluorescence imaging, gold nanoshells, quantum dots.

# Resumen

En esta tesis se han investigado diversos agentes de contraste para imagen cardiovascular a nivel molecular. Las investigaciones se basan fundamentalmente en la técnica de Tomografía Óptica Coherente Intravascular (TOC-IV). Actualmente, las enfermedades cardiovasculares son la causa de la mayoría de los decesos en el mundo. Desde hace unos años, la TOC-IV se ha venido utilizando como técnica mínimamente invasiva para la implantación de stents y la detección y evaluación de placas de ateroesclerosis. El desarrollo de agentes de contraste nanométricos, ayudaría a detectar dichas placas a nivel molecular. Además, si se combinan las técnicas de TOC-IV con la de imagen por fluorescencia, dichos agentes de contraste permitirán imágenes cardiovasculares de alta resolución.

En primer lugar, se ha investigado el nivel de contraste en las señales de TOC-IV dado por diversas nanopartículas de oro, tanto a nivel de imágenes estáticas como a nivel de imágenes dinámicas, utilizando las distintas funciones que la TOC-IV proporciona. Se ha determinado que la TOC-IV es capaz de detectar nanopartículas de oro individuales, dada la gran sensibilidad de ésta técnica de imagen.

En segundo lugar, dado que la TOC-IV se basa en la radiación esparcida por las diversas muestras, se han investigado diversos tipos de nanopartículas de oro (nano-bastoncillos, nano-estrellas y nano-esferas dobles (sílice-oro)) mediante diversas técnicas, incluyendo microscopía de campo oscuro, espectroscopia foto acústica y, naturalmente, TOC-IV, concluyéndose que las nano-esferas dobles (GNSs, de la traducción al inglés; “gold nano-shells”) son los mejores agentes de contraste para TOC-IV.

En tercer lugar, se ha investigado el contraste producido por los GNSs tanto en células como en tejidos, dadas las excelentes propiedades de estas nanopartículas. Para ello, se han incubado en células HeLa cómo en células Jurkat, demostrando que se mejora el contraste en la señal de TOC-IV dada por estas células una vez que se internalizan en ellas los GNSs. Este incremento de contraste se ha verificado también mediante microscopía de campo oscuro. Además, se ha demostrado que los GNSs insertados en tejidos incrementan el contraste en la señal de TOC-IV.

Finalmente, se han investigado nanopartículas de cristales semiconductores (puntos cuánticos) que emiten en la tercera venta biológica al ser excitados por el láser del sistema TOC-IV. Dada la alta sensibilidad del TOC-IV, estos puntos cuánticos aumentan el contraste de la señal tomográfica, de manera que actúan como dobles sondas ópticas, TOC y fluorescencia, tanto en sistemas coloidales como en arterias y tejidos.

En consecuencia, las nanopartículas investigadas, tanto puntos cuánticos como nanopartículas de oro, podrían ser muy útiles para imagen cardiovascular a nivel molecular, siempre que se funcionalicen convenientemente para anclarse al sitio dañado. Esto proporciona altas posibilidades de imagen con alta resolución en la formación de placas de aterosclerosis.

Palabras clave: Enfermedades cardiovasculares, placas de arterosclerosis, Tomografía óptica coherente, nanopartículas de oro, puntos cuánticos

# Chapter 1 Introduction and motivation

## 1.1 Cardiovascular diseases

Cardiovascular diseases (CVDs) are the main cause of death in the worldwide, representing 32% of all the death. The data was get from OECD. Stat,[1] by selecting variables with causes of mortality and diseases of the circulatory system, years are from 2012 to 2014. In China, the problem is more serious, around 0.29 billion suffers, and a leading cause of death, which account for 42.61 % in the urban area, according to the report on cardiovascular disease in China (2016). The main dangerous factors for cardiovascular disease are hypertension, cigarette smoking, hyperlipidemia, diabetes, insufficient physical activity, and air pollution.

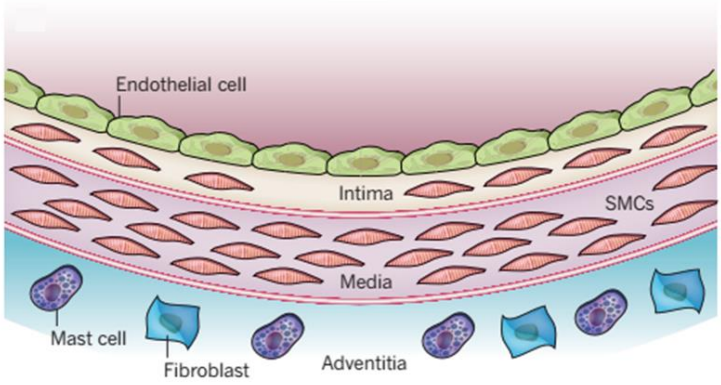


**Figure 1.1** The normal structure of the artery.[2]

Atherosclerosis is the key pathogenesis of cardiovascular diseases. It refers to the development of atheromatous plaques in the arteries,[2] notably in arterial branch points and bifurcations.[3] The normal structure of the artery consists of three layers. The adventitia layer, which is connected to the tissue, contains mast cells, nerve ending and microvessels as shown in **Figure 1.1**.[2] The tunica media composed of smooth muscle cells (SMCs) embedded in a complex extracellular matrix. The intimal layer, contains SMCs and an endothelial cell monolayer which exposures to the blood.[2] In healthy conditions, the arterial endothelial cells resist the adhesion of circulating immune cells to them.[4] Under atherogenic stimuli, such as hypertension, dyslipidaemia and cigarette smoking, the changes in the endothelial permeability and the composition of the extracellular matrix in the tunica media lead to entry and accumulation of low density lipoprotein (LDL) particles in the subendothelial, as shown in **Figure 1.2**.[5, 6] Once trapped in the subendothelium, some of the LDL particles are oxidized, and thus cause the activation of the endothelial cells.[7] The activated

endothelial cells express chemokines, that promote the recruitment of the monocytes to the vessel wall and directional migration by interact with cognate chemokine receptors on the monocytes, such as vascular cell adhesion molecule 1 (VCAM-1) and intercellular adhesion molecule 1 (ICAM-1). A number of monocytes in the early atherosclerotic lesions differentiate into macrophages, and ingest oxidized lipoproteins via scavenger receptors.[5, 8, 9] The accumulation of lipid droplets in the cytoplasm of the macrophages, promote lipid-laden macrophages to become foam cells, denote the atherosclerosis. Foam cells can secrete additional extracellular matrix molecules. Extracellular matrix molecules are composed of certain collagen, elastin, proteoglycans and glycoproteins. They interact with cells and generate signals to control the behaviors of the cells.[10] In atherosclerosis, they promote lipoprotein accumulation and recruitment of monocytes.[8] Under prolonged endoplasmic reticulum (ER) stress, foam cells die from apoptosis and necrosis and the cellular lipids are deposited in the artery. In the early atherosclerosis lesions, which is called inflammation resolution, efferocytosis (the process that dying or dead cells are cleared by phagocytic cells) is efficient and can rapidly clear the apoptotic macrophages. In advanced lesions, so called no inflammation resolution, the efferocytosis is not efficient, the apoptotic macrophages start undergo secondarily necrotic, and necrotic macrophages coalesce into necrotic cores. In the lipid-rich necrotic cores, the death of the smooth muscle cells and degrading cap collagen would thin the fibrous cap and promote the plaque vulnerable to rupture. In this process, two kind of proteases: matrix metalloproteinases (MMP) and cysteine proteases play an important role in arterial wall extracellular matrix degradation and remodeling.[11-14] If there is no inflammation resolution, the fibrous cap breaches leading to the luminal thrombosis and arterial occlusion.[8]

In the past few decades, molecular imaging has been developed to be a strong method to visualize specific molecular process *in vivo* due to the fast development in imaging agents and technologies. Molecular imaging can also make a significant contribution to the atherosclerosis imaging. Normally, the application of molecular imaging to a special disease need to address the following four question.[15, 16] (1) Is there any molecular target corresponding to the disease of interest? (2) Is there an affinity ligand that will bind to the target? Usually, the suitable molecular target and ligand could be found in the literature. (3) What is the appropriate molecular imaging system to provide the optimal resolution, sensitivity, and depth penetration for the disease? (4) What kind of molecular agent is needed for the selected imaging system to detect the molecular target?

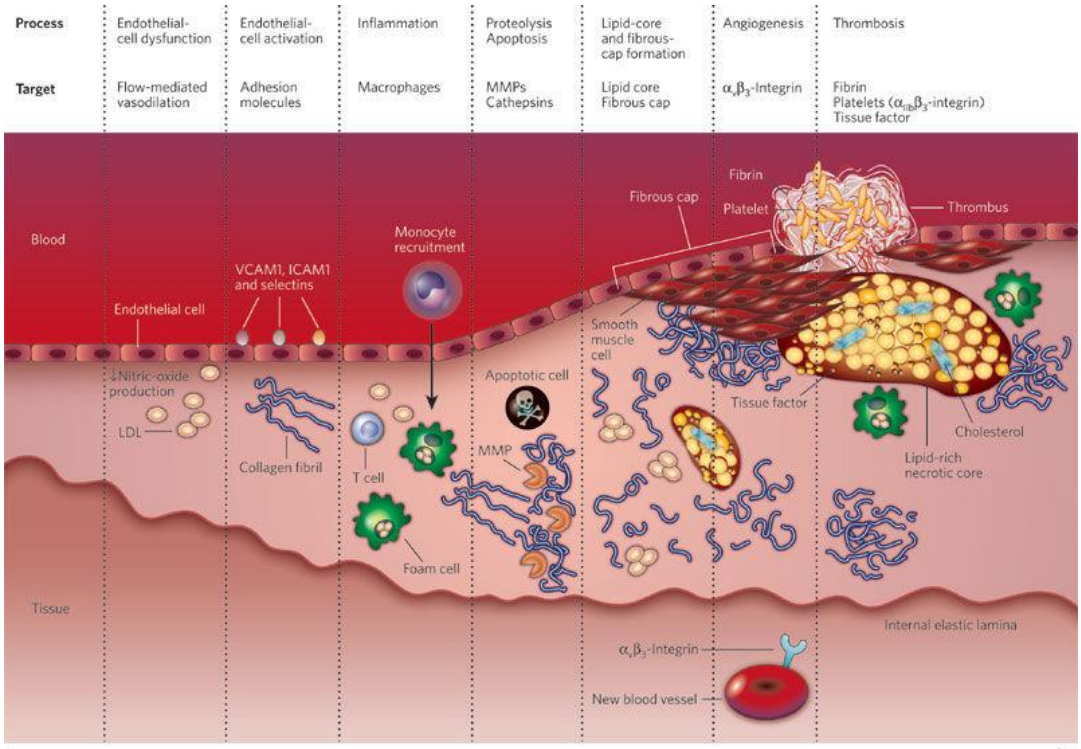


**Figure 1.2** The development of an atherosclerotic lesion, potential targets for molecular imaging at each stage are listed on the top.[6]

For the first and second questions, different diseases and processes have different molecular targets and ligands as shown in **Figure 1.2**.[6] For example, in the early stages of atherosclerosis, the endothelial cell dysfunction and activation caused by the hemodynamic and inflammatory factors, lead to the expression of VCAM-1, ICAM-1 and selectins (P and E)[7] on these dysfunctional cells. The corresponding antibodies could act as affinity ligands, such as VCAM-1-targeting peptides.[17, 18] In the inflammation, the macrophages differentiated from monocytes can be used as a target. Macrophages phagocytosis can be used as a target strategy to deliver the nanoparticles (NPs). For example, their phagocytosis of LDL in the atherosclerosis process has used the iron NPs conjugated with lectinlike oxidized LDL receptor-1 antibody to specifically target to the macrophages.[19] In the angiogenesis, the target is $\alpha_v\beta_3$ integrin.

Molecular imaging studies of atherosclerosis are expected to be useful in the following clinical scenarios:[20] (1) identifying patients with high-risk of cardiovascular complications, (2) characterizing the vulnerability of the lesions, (3) evaluating novel atherosclerotic therapies, and (4) selecting individualized treatment strategies for the particular vulnerable plaques. In the

following section, I will talk about the imaging techniques and corresponding contrast agents, and how they are used for the above clinical scenarios.

## 1.2 Cardiovascular imaging techniques based on light

### 1.2.1 Optical coherence tomography

#### 1.2.1.1 *Theory*

Optical coherence tomography (OCT), which was discovered by David Huang and co-workers in 1991, is very similar to ultrasonic pulse-echo imaging.[21] It uses low coherence interferometry to collect the scattering light from the tissue microstructures. OCT has very high resolution, around 15 μm and can detect backscattered light as small as $10^{-10}$ times of the incident intensity.[21] Due to these high resolution and sensitivity of the OCT, it has been widely used in medical areas, such as ophthalmology and vascular surgery.[22-25]

In the particularly case of cardiovascular disease, the intravascular OCT (IV-OCT) was used. It uses a single optical fiber (catheter) that can illuminate to the artery by rotating and being pulled back along the artery,[24] and at the same time, recording the backscattered light produced by the artery. The reflected light then interferes with the light from reflected mirror at coupler, and then is sent to the detector. The detector signal is converted to the reflectivity profile by using Fourier analysis..

#### 1.2.1.2 *Applications of IV-OCT*

Due to the high resolution of the OCT, it has been widely used to investigate the coronary atherosclerosis. The normal structure of the artery as seen by IV-OCT, is shown in **Figure 1.3 (a)**. A healthy artery is formed by different layers, the intima (I), the internal elastic lamina (IEL), the media (M), the external elastic lamina (EEL) and the adventitia (A). In the figure inside the artery there is a catheter, with a diameter around 1 mm. In addition, the IV-OCT is also able to reveal the morphology of atherma plaques, as shown in **Figure 1.3**. Therefore, it is possible to distinguish different type of plaques, e.g. fibrous plaques with homogeneous and signal rich regions (**Figure 1.3 (a))**, fibrocalcific plaques with well delineated and signal poor regions with sharp borders (**Figure 1.3 (b))**, and lipid rich plaques with signal poor regions and diffuse borders (**Figure 1.3 (c))**.[26] IV-OCT is also useful for measuring vessel lumen diameter, which is very important for

selecting a suitable size of stent at a target site and helping the stent placement.[27] In **Figure 1.3 (a)**, the diameter of the artery is around 2 mm. In **Figure 1.3 (c)**, we see the fibrous cap, whose thickness plays an important role in the plaque rupture. It has been observed that if the cap thickness is less than 65 μm, the plaque can easy to break, and cause an acute thrombus.[28] Therefore, OCT has also been used to measure the thickness of the fibrous cap as a marker of the plaque vulnerability. A study about association of the statin therapy with reduced coronary plaque rupture by OCT, showed the OCT measured thickness of the fibrous cap under stain therapy (78μm) tend to increase than that of without stain therapy (49μm).[29] In this case, after the stain therapy, the coronary plaques tend to become more stable.

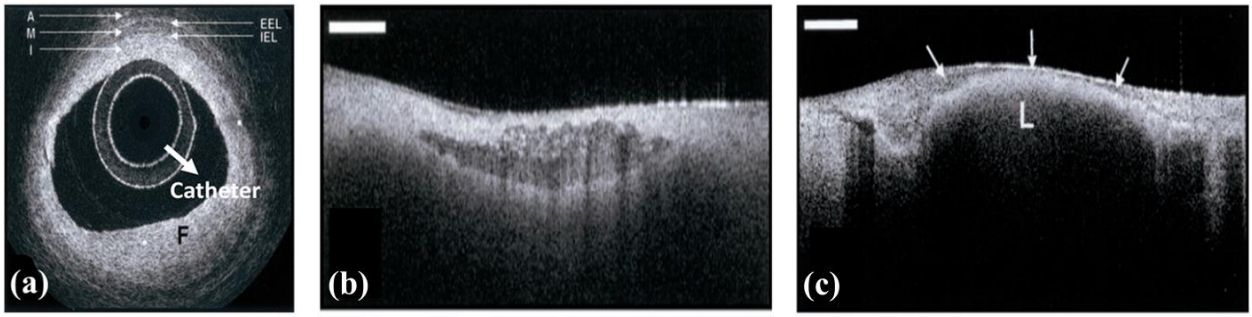


**Figure 1.3 (a)** OCT image of a fibrous coronary plaque showing a homogeneous, signal-rich interior (F). An area of intimal hyperplasia is seen opposite fibrous lesion, demonstrating intima (I, with intimal hyperplasia), internal elastic lamina (IEL), media (M), external elastic lamina (EEL), and adventitia (A). **(b)** OCT image of a fibrocalcific aortic plaque showing a sharply delineated region with a signal-poor interior. **(c)** OCT image of a lipid-rich carotid plaque showing a signal-poor lipid pool (L) with poorly delineated borders beneath a thin homogeneous band, corresponding to fibrous cap (arrows).[26] Bar=500μm

To avoid the attenuation that light suffers in the artery caused by the red blood cells, the blood is completely removed with a saline flush before taking the OCT image.[24] Xu and coworkers probed that it is possible to identify the plaque composition from the IV-OCT signal by studying the attenuation and the backscattering coefficient of different plaques. They found that the backscattering coefficient had different values for calcification ($4.9\pm1.5 mm^{-1}$), for fibers ($18.4\pm6.4 mm^{-1}$) and for lipid pool ($28.1\pm8.9 mm^{-1}$), and the same happened to the attenuation coefficients ($5.7\pm1.4 mm^{-1}$, $6.4\pm1.2 mm^{-1}$ and $13.7\pm4.5\ mm^{-1}$, respectively).[30]

Other strategy for the characterization of atherosclerotic plaques is based on the study of macrophages. Macrophages are inflammatory cells and they can release tissue factors and cause plaque rupture.[31] Some studies have shown that it is possible to detect the presence of macrophages by OCT.[32-34] As shown in **Figure 1.4**, which compares a fibrous cap with low density of macrophages to one with high density of macrophages, the OCT intensity is much higher in the case of high macrophages content **(d)**. Macrophages can be identified in the low content macrophage fibrous cap after doing the logarithm of the OCT image, and combining the images with the ones given by histology.

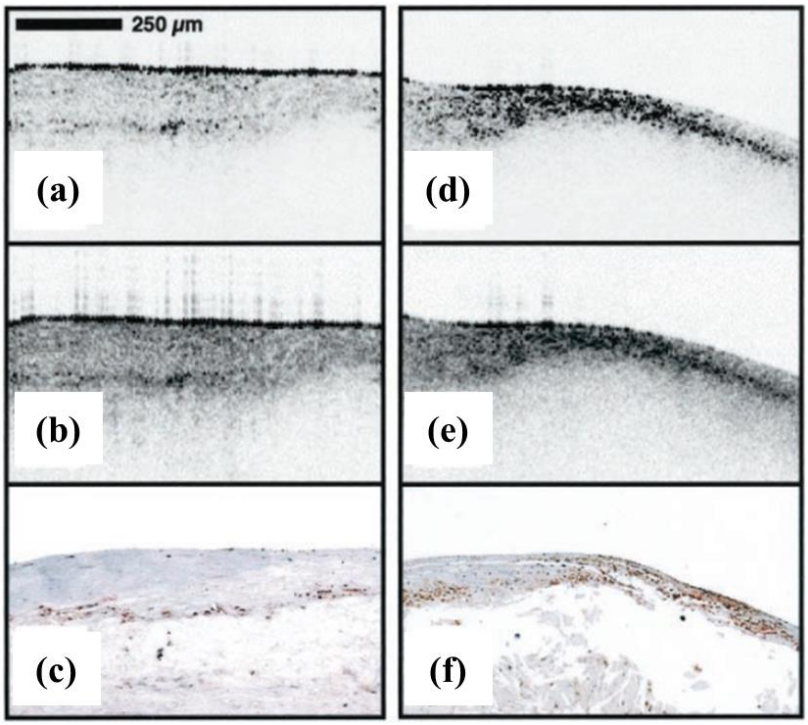


**Figure 1.4** Raw **(a)** and logarithm base 10 **(b)** OCT images of a fibroatheroma with a low density of macrophages within the fibrous cap. **(c)**, Corresponding histology for **(a)** and **(b)** (CD68 immunoperoxidase; original magnification ×100). Raw **(d)** and logarithm base 10 **(e)** OCT images of a fibroatheroma with a high density of macrophages within the fibrous cap. **(f)**, Corresponding histology for **(d)** and **(e)** (CD68 immunoperoxidase; original magnification ×100).[32]

Currently, the IV-OCT is widely used for characterization of plaque type, fibrous cap thickness, plaque rupture, and evaluation of intracoronary stenting.[24, 35, 36] However, due to the lack of molecular contrast, the molecular process under the atherosclerosis, as we discussed in the first

part, can not be visualized by IV-OCT. Therefore, the use of contrast agent would help IV-OCT to detect the atherosclerosis process at molecular level.

### 1.2.2 Photoacoustic imaging

#### 1.2.2.1 *Theory*

Photoacoustic (PA) imaging has become a strong tool in biological imaging due to its high contrast, high resolution and high penetration depth. In PA imaging, the tissue is irradiated by a short pulse laser with a duration of nano-second. The absorption of the light energy by the tissue induces a slight temperature increment,[37] which causes a thermoelastic expansion. This generates a sound or stress wave (acoustic wave) that can propagate through the tissue. Once the acoustic wave reaches to the tissue surface, it can be detected with an ultrasound transducer.[38, 39]

Normally, PA imaging is considered dependent on the absorption coefficient due to small difference in the mechanical and thermodynamic properties of different tissues.[39] The absorption coefficient spectrum of endogenous tissue chromophores is shown in **Figure 1.5**. The differences of the absorption coefficient of a single chromophore at different wavelength and chromophores at the same wavelength allow the differentiation of the tissue type by properly choosing the PA excitation wavelength.[38] For example, by measuring the multiwavelength PA signal of the blood vessel, the obtained concentration of oxyhaemoglobin and deoxyhaemoglobin can be used to determine the blood oxygen saturation.[40, 41]

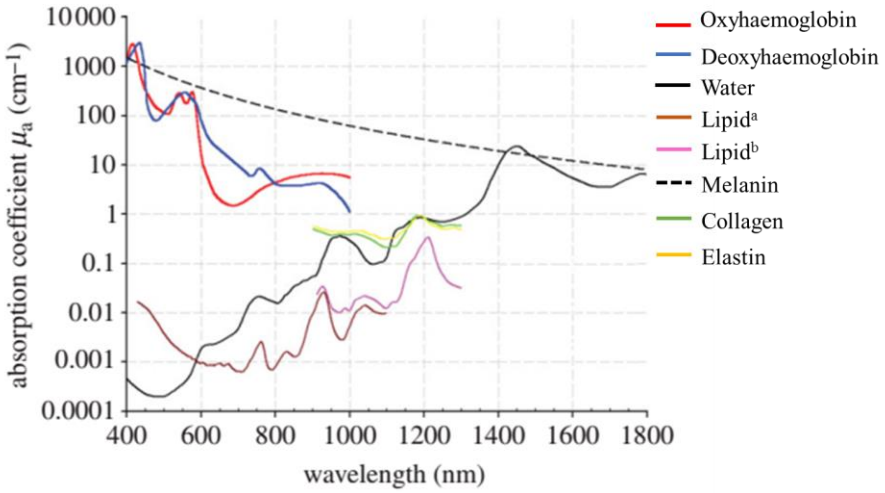


**Figure 1.5** Absorption coefficient spectra of endogenous tissue chromophores.[42]

For PA imaging, penetration depth is dependent on the attenuations of the light and the acoustic wave.[42] In biological tissues, the light transfer is dominated by scattering.[43] Therefore, the scattered light can go through into deep of the tissue even they almost lose their original incidence direction.[43] However, these photons can still produce an acoustic wave, and this signal could still be detect by the transducer because the acoustic scattering in the tissue is two or three order of the magnitude weaker than that of light. Thus a high penetration depth for PA imaging is possible. For example, the reported penetration depth achieved in human breast is 4 cm.[44] The spatial resolution is limited to sub-millimetric due to the acoustic attenuation, and also is determined by the width of the pulse laser, width impulse response and focal diameter of the transducer, and the center frequency of the received PA signal.[37, 42]

#### 1.2.2.2 *Applications to cardiovascular diseases*

Due to its high penetration depth and not bad spatial resolution, PA imaging has been widely used in biomedicine.[37, 38, 42] In the case of cardiovascular disease, intravascular PA (IV-PA) has been used for the identification of vulnerable plaque. In IV-PA, the axial resolution is 100μm, lateral resolution is 500μm and the penetration depth is 5 mm.[38] In the absorption spectra shown in **Figure 1.5**, the absorption of lipid shows a strong absorption around 1200 nm. In 2010, by using a 1200 nm laser as light source for IV-PA imaging, Wang et.al successfully got *ex vivo* image of the lipid in atherosclerosis rabbit aorta based on the different optical absorption spectrum of the fat in the near infrared range.[45] Furthermore, a big number of contrast agents have been used to get PA molecular images of the various stages of the atherosclerosis disease progression.[46, 47] In lipid rich necrotic cores, the elevated expression of matrix metalloproteinase-2 is one of the clinical features. In 2016, Huan et.al used the GNRs conjugated with the matrix metalloproteinase-2 antibody as a high efficient IV-PA probe to detect the matrix metalloproteinase-2 in atherosclerosis.[48] The GNRs could target the matrix metalloproteinase-2 due to the antibody, and thus increased the absorption of the matrix metalloproteinase-2, and a high IV-PA enhancement was achieved which could provide a precise morphology to visualize the area of the distribution of matrix metalloproteinase-2 in the arterial walls.[48]

IV-PA is currently undergoing refinement, although it has shown its capability of imaging the atherosclerosis disease. Many important aspects face the real-time clinical imaging still need to be solved, such as the optimal image acquisition sequence, laser source and catheter design.[38]

### 1.2.3 Fluorescence imaging

#### *1.2.3.1 Fluorescence imaging technique*

Fluorescence imaging is a technique that allows acquisition of data at high speed and visualization of biological process in the dynamic conditions.[49] Typically it uses light source (a laser or white light with an excitation filter) to excite a fluorescent molecule, and the emitted signals with different spectral characteristics can be isolated by emission filter and captured by a CCD camera (detector range: 400 – 1000 nm) or an InGaAs camera (detector range 0.9-1.7 μm).[50] This technique has two challenges. First is the limited penetration depth due to the absorption and scattering of light due to the tissue. Therefore, it is very important to select the excitation and emission wavelengths in the region known as biological windows which are shown in **Figure 1.6**.[51] The first biological window (I-BW) extends from 700 to 950 nm, and corresponds to the end of the visible absorption band from hemoglobin to the beginning of water absorption band around 980 nm.[51] The second biological window (II-BW) is found from 1 to 1.35μm, in this window, the scattering coefficient is reduced and a deeper penetration depth is expected in this range. The third biological window (III-BW) is in the range from 1.5 to 1.8μm, the tissue autofluorescence is almost zero in this range, which could allow getting a high optical contrast after using a contrast agent that emits fluorescent signals in this range[52]. In second place is the need of appropriate contrast agents. Differently from OCT and PA that can image the tissue based on the scattering and absorption properties of the tissue without using exogenous agents, fluorescence imaging strongly depends on contrast agent, due to the weak fluorescence given by most tissues.[53] The contrast agent has to be biologically stable in the organism, specially target the disease site, and produce fluorescence imaging contrast.[54] Common contrast agents emitting in BW have been widely used for fluorescence imaging, such as ICG, cyanine dyes, quantum dots, single-walled carbon nanotubes and rare earth nanoparticles.[55]

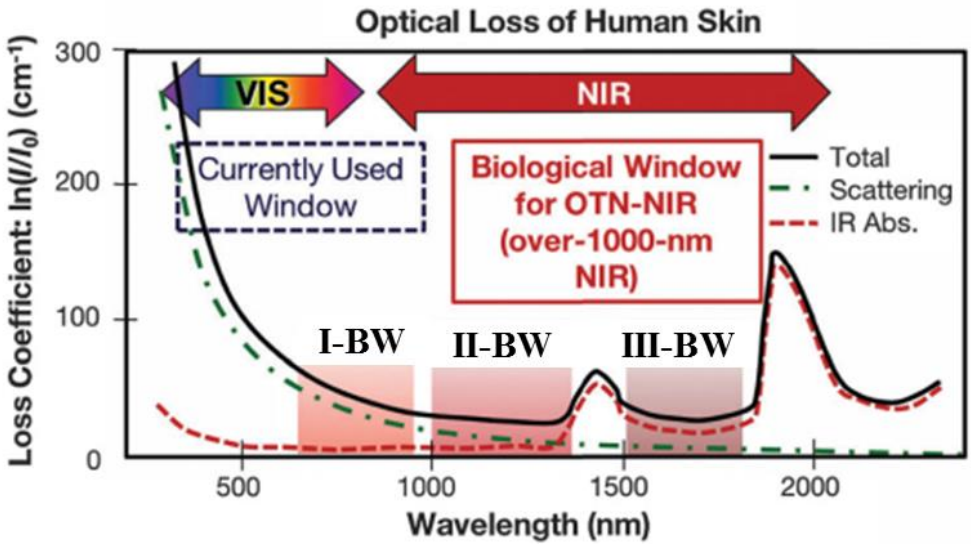


**Figure 1.6** Absorption spectrum of human skin showing the first (I-BW), second (II-BW) and third (III-BW) biological windows

### *1.2.3.2 Application to cardiovascular disease*

During the last ten years, the huge progress in clinical intracoronary optical imaging lead to the development of the near infrared spectroscopy catheter, which has been approved by the FDA.[56, 57] Intravascular near infrared fluorescence (NIRF) imaging is a catheter based technique, in which the excitation light is introduced to the artery by using a catheter, simultaneously, the emission signal from the tissue is collected by the catheter and sent to the detector. Two dimensional fluorescence images of the artery could be achieved by rotating and pull back the catheter. It has been used to measure the disease activity within the cardiovascular.[58] In 2011, Claudio et al exploited the indocyanine green (ICG) as a contrast agent to imaging the atherosclerosis plaques.[59] ICG is a FDA approved dye, could be quickly absorbed by lipid-rich plaques and cells. In addition, ICG has a strong absorption in 785 nm, and emission at 815 nm, these absorption and emission band are located in the I-BW. Therefore, ICG is expected to produce a high fluorescence contrast. In this work, within 20 minutes injection, the sufficient contrast enhancement could be used *in vivo* detection of lipid-rich, inflamed, coronarysized plaques in atherosclerotic rabbits. What's more, *in vitro* and human atheroma specimen studies showed that the ICG prefer to target the lipid rich macrophages. At the same year, a dual-modality (OCT and NIRF) intra-arterial catheter for simultaneous microstructural and molecular imaging *in vivo* was reported by Hongki et al.[60] The

NIRF has a highly sensitive detection of Cyanine7 (Cy7), NIRF imaging of the fibrin-coated stent *in vitro* and *in vivo*, thrombus and heterogeneous protease activity have been obtained by using this technique.[60]

However, most of the contrast agent for intravascular NIRF imaging are dyes that are highly susceptible to photobleaching, which will affect the sensitivity of the detection.[53] Up to now, most of the emission of these dyes are located in the first biological window, and the autofluorescence of the tissue has a high effect on the NIRF signal. There, new contrast agent are strongly needed for intravascular NIRF imaging.

## 1.3 Contrast agents

Nowadays, it is assumed that an efficient fight against CVDs requires a great effort in social education for the introduction of healthy life habits and, in parallel, a significant improvement in the diagnosis techniques. These techniques should improve in two distinct directions: Firstly, cost reduction is mandatory, as convectional techniques (such as X-Ray assisted catheterization) require expensive and complicate apparatus. Secondly, these conventional techniques fail, in most of the cases, to provide molecular information of CVDs, so that the design and development of specifically designed therapies are not possible. Nanotechnology can simultaneously overcome these two challenges. The reduced size and high surface to volume ratio characteristic of nanoparticles (NPs), makes them especially suitable for molecular imaging.[61, 62] It has been already demonstrated that NPs bound to specific affinity ligands, such as monoclonal antibodies, and so enabling non-invasive phenotypic characterization of atherosclerosis plaques. At the same time, the use of NPs also opens the door to the development of cost-effective and minimally invasive diagnosis and imaging tools. In particular, the use of optical NPs as a contrast agents, i.e. NPs capable of producing scattered light, luminescence or acoustic waves under light illumination, would allow the use of cost effective laser light sources for cardiovascular imaging instead of more complicated apparatus (such as MRI, X-Ray, SPET… and so on).[61, 63-65] Because of these two reasons, the scientific community is already considering optical NPs as reliable and powerful tools for the next generation of imaging probes for the cardiovascular system.[4, 66-68]

### 1.3.1 Gold nanoparticles (GNPs)

Nowadays, GNPs have received a particular attention for bio applications, such as photothermal therapy and medical imaging (OCT and PA). These widely applications of GNPs are due to the following respects. First, they can be easily synthesized with different shapes and with tunable optical properties. Second, they are biocompatible, can be functionalized with different ligand and delivered to the disease sites.[69] This part, I will focus on optical properties of GNPs and their applications for cardiovascular disease.

*Optical properties of GNPs:* Surface plasmon resonance is the most important optical property of the GNPs. It consists of a collective oscillation of conduction electrons induced by the electromagnetic field of light. As shown in **Figure 1.7 (a)**, after irradiated by light, the conduction electrons oscillate coherently to the incident light. This results the absorption and scattering properties of the GNPs. The oscillations wavelength strongly depends on the morphology of the GNPs, for example, for GNRs, as shown in **Figure 1.7 (b),** they have two oscillations, transverse and longitudinal, thus induce two extinction peaks in the extinction spectra.[70] Furthermore, the surrounding medium also affects the resonance wavelength.[71]

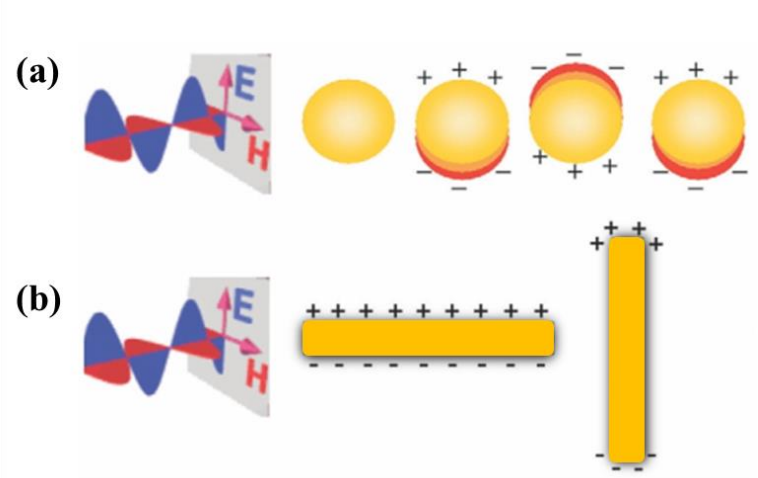


**Figure 1.7** (a) Schematic drawing of the interaction of an electromagnetic radiation with a gold nanosphere. A dipole is induced, which oscillates in phase with the electric field of the incoming light. (b) Transverse and longitudinal oscillation of electrons in a gold nanorod.[70]

Gustav Mie solved the Maxwell's equations for small spheres ($d \ll \lambda$) obtaining an expression that can predict the scattering and absorption properties of the particles.[72, 73] The expression that he obtained for the extinction coefficient $C_{ext}$ can be written as:

$$C_{ext} = \frac{24R^3\varepsilon_m^{3/2}}{\lambda}\frac{\varepsilon_2}{(\varepsilon_1 + 2\varepsilon_m)^2 + {\varepsilon_2}^2} \tag{1.1}$$

where $R$ is the radius of the GNPs, $\varepsilon_m$ is the medium dielectric constant, $\lambda$ is the wavelength of the incident light, $\varepsilon_1$ and $\varepsilon_2$ are respectively the real and imaginary part of the complex dielectric function for small particles, and they are frequency dependent. Thus the extinction properties of the small particles strongly depend on the dielectric constants of the metal, its surrounding medium and its volume.[51, 72] However, the Mie theory cannot be used to predict the optical properties of nanoparticles with size larger than 20nm or explain the near infrared extinction spectra of nanoparticles.[51]. In 1912, Gans developed a solution to explain the extinction properties of the prolate spheroid. [74].The estimated extinction coefficient given by Gans[74] is:

$$C_{ext} = \frac{8\pi^2R^3\varepsilon_m^{3/2}}{3\lambda}\sum_j \frac{\left(1/P_j^2\right)}{\left\{\varepsilon_1 + \left[\left(1-P_j\right)/P_j\right]\varepsilon_m\right\}^2 + \varepsilon_2^2} \tag{1.2}$$

where $Pj$ includes the depolarization factors for the each axis of the particle; $P_a$, $P_b$ and $P_c$. For gold nanorods (a > b = c), the depolarization factors are defined as

$$P_a = \frac{1-r^2}{r^2}\left[\frac{1}{2r}\ln\left(\frac{1+r}{1-r}\right) - 1\right];\ P_b = P_c = \frac{1-P_a}{2} \tag{1.3}$$

where r is corresponded to the aspect ratio ($r = \sqrt{1-(b/a)^2}$). The wavelength $\lambda_{max}$ longitudinal plasmon resonance depend on the aspect ratio and medium dielectric constant has been derivated by El-Sayed et al[71]:

$$\lambda_{max} = 33.34\varepsilon_m\frac{b}{a} - 46.31\varepsilon_m + 472.31 \tag{1.4}$$

For more complicated GNPs, such as gold nanoshells (GNSs) and gold nanostars (GNSTs), some numerical methods have been developed to explain the absorption and scattering properties of these GNPs. For example, discrete dipole approximation (DDA), finite difference time domain and finite element method.[75, 76]

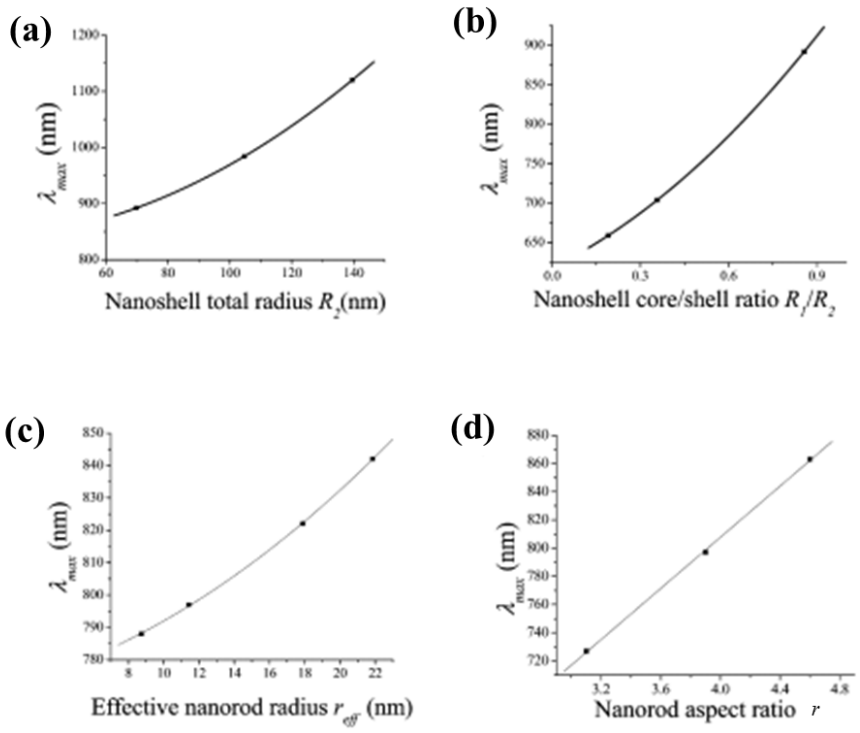


**Figure 1.8.** Tunability of the plasmon resonance maximum in nanoparticles. Variation of surface plasmon extinction maximum $\lambda_{max}$ with **(a)** nanoshell total radius $R_2$ at fixed $R_1/R_2 = 0.857$, **(b)** nanoshell core/shell ratio $R_1/R_2$ at fixed $R_2 = 70$ nm, **(c)** nanorod effective radius $r_{eff}$ at fixed aspect ratio $r = 3.9$, and **(d)** nanorod aspect ratio $r$ at fixed $r_{eff} = 11.43$ nm (and straight line fit).[77]

Based on the methods that have been developed to explain the extinction spectra of the GNPs, the extinction peak of the GNPs can be tuned to the near infrared region, in the biological windows, which is very useful for applications in biology and medicine. For example, GNPs can act as a contrast agent for bioimaging and be used for photothermal therapy[72]. For GNSs, the maximum plasmon extinction $\lambda_{max}$ can be tuned from 800 to 1200 nm, when increasing the nanoshell total radius $R_2$ from 60 to 140 nm, while fixes the nanoshells core/total ratio $R_1/R_2$ at 0.857 as shown in **Figure 1.8 (a)**. In addition, this tunable property can be achieved by fixing the $R_2$ at 70 nm and increasing the ratio $R_1/R_2$ as shown in **Figure 1.8 (b)**. In the case of the GNRs, the maximum

plasmon resonance can be shifted by changing the size (effective radius, which is given by $r_{eff} = (3V/4\pi)^{1/3}$) and the aspect ratio ($r$) as shown in **Figure 1.8 (c)** and **(d)**. Particularly, when fixes the effective radius, the maximum surface plasmon extinction increases linearly as function of the aspect ratio $r$.

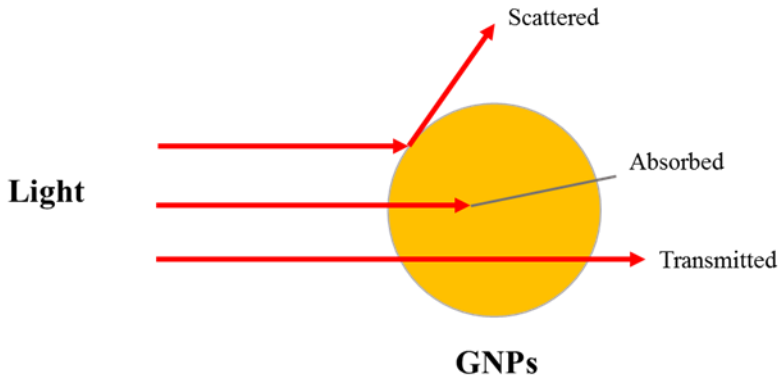


**Figure 1.9** Interaction between light and GNPs

As we already know, when the light excites the GNPs, it can be scattered and absorbed by the GNPs, or pass through the GNPs, as illustrated in **Figure 1.9**. The absorption cross section and scattering cross section determine the extinction cross section of the GNPs. Photothermal therapy and PA application strongly depend on the absorption property of the GNPs.[69, 78] However, OCT, which detects the back scattered light of the material, is strongly dependent on the scattering coefficient of the GNPs[69]. Therefore, the understanding of the absorption and scattering properties of GNPs will make full use of the GNPs. In 2006, Prashant et al calculated the absorption and scattering properties of GNPs of different sizes, shapes and compositions.[77] As shown in **Figure 1.10**,[77] for GNSs, when the core radius $R_1$ is 120 nm, and the total radius $R_2$ is 155 nm, the scattering cross section start to play a big role in the extinction cross section after the extinction wavelength at 600nm. They also gave a prediction to the scattering/absorption ratio ($C_{sca}/C_{abs}$) of GNPs based the morphology of the GNPs. They found that the $C_{sca}/C_{abs}$ ratio of GNSs increases when increasing the total radius $R_2$ while fixing the $R_1/R_2$ ratio. They also found that the ratio increases when increasing the $R_1/R_2$ ratio while fixing the $R_2$. As for gold nanorods (GNRs), the aspect ratio ***r*** is the ratio of the nanorod dimension along the long axis to that along the short axis. The $C_{sca}/C_{abs}$ of GNRs increases when increasing the effective radius $r_{eff}$, while fixing the aspect ratio ***r***. but it is very hard for $C_{sca}/C_{abs}$ ratio to increase to more than 1. The aspect ratio doesn't

show a strong effect on the $C_{sca}/C_{abs}$ ratio when fixing the effective radius $r_{eff}$. Therefore, they conclude that the absorption cross section is always the dominant factor in the extinction cross section of the GNRs.

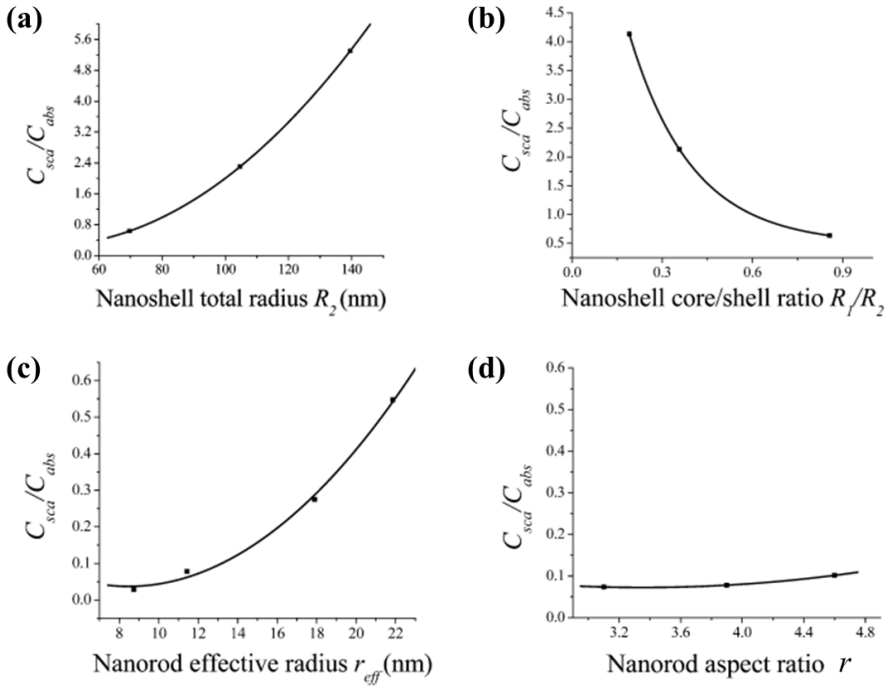


**Figure 1.10** Tunability of the ratio of scattering to absorption of nanoparticles. Variation of $C_{sca}/C_{abs}$ with **(a)** nanoshell total radius $R_2$ at fixed $R_1/R_2 = 0.857$, **(b)** nanoshell core/shell ratio $R_1/R_2$ at fixed $R_2 = 70$ nm, **(c)** nanorod effective radius $r_{eff}$ at fixed aspect ratio $R = 3.9$, and **(d)** nanorod aspect ratio $r$ at fixed $r_{eff} = 11.43$ nm

*Applications:* Due to their strong absorption and scattering cross section and their strong sensitivity to the environment, GNPs have been widely used for photo-thermal therapy, optical contrast for OCT and PA, and biosensing.[69, 78-80]

In 2015, Adam de la Zerda et al used the GNRs for OCT imaging of living mice eyes, with an OCT operating 860 ±48nm wavelength. The quantifying GNRs detection limit in mouse cornea was achieved by injecting different concentration of GNRs (peaking at 780 nm) in mice corneas, the limit detection concentration is 0.5 nM. The OCT contrast enhancement was achieved after mice injected with 10 μL of GNRs at 50 nM indicated by the white arrow, compared to OCT cross section image of mice only injected with balanced saline solution (BSS) and non-injected mice as

shown in **Figure 1.11**. The contrast enhancement is due to the scattering of GNRs. Therefore, they demonstrated that GNRs could be used for OCT contrast enhancement.

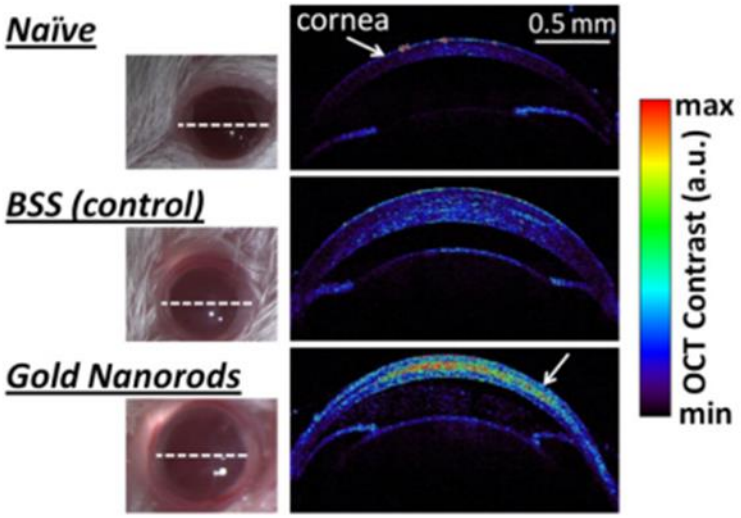


**Figure 1.11** OCT detection of GNRs in living mice corneas. Left: Optical eye images for mice corneas were injected with 10 μL of GNR at 50 nM (lower), and control mice corneas were injected with 10 μL of balanced saline solution (BSS) (middle) or not injected at all (upper). Right: OCT cross section images through the mice eyes (left column, white dotted line).[81]

In addition to GNPs as a contrast agent based on the scattering properties, they also can be used as a contrast agent based on the absorption properties. Gold nanocages, which has tunable extinction properties has been studied as an absorption contrast agent for OCT by Younan Xia's group.[82] As shown in **Figure 1.12 (a)**, the gold nanocages show a high absorption coefficient, being the absorption efficiency and cross section calculated by DDA 87% and $7.63 \times 10^{-11}$ $cm^2$, respectively.[82] The OCT image and signal distribution as function of depth showed a high OCT signal attenuation in deeper depth compared to that of portion without gold nanocages, as shown in **Figure 1.8 (b)** and **(c).** This is due to high absorption cross section and low scattering cross section of gold nanocages.

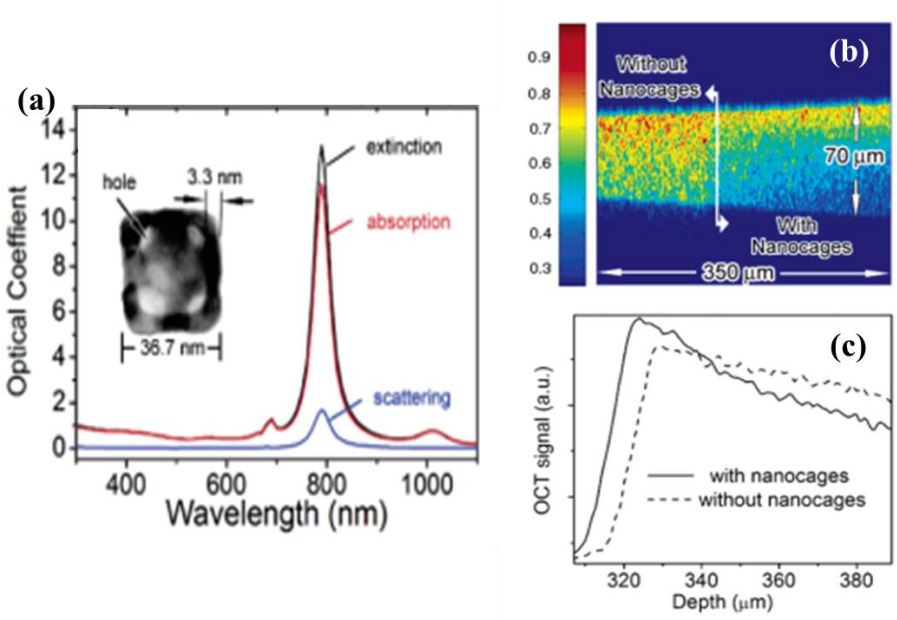


**Figure 1.12 (a)** DDA calculated extinction, absorption and scattering coefficients of gold nanocages based on the dimensions provided by the TEM image in the inset. **(b)** OCT image of a gelatin phantom embedded with $TiO_2$. The left portion did not contain any gold nanocages, while the right portion contained 1 nM of gold nanocages. **(c)** Plots of the OCT signals on a log scale as a function of depth.

Furthermore, GNPs have been used as optical contrast agent for PA imaging, due to their absorption cross section.[46] In cardiovascular diseases, the matrix metalloproteinases play an important role in weakening the plaque caps and promoting rupture.[48] Therefore, the quantification of the matrix metalloproteinases in atherosclerosis plaque is important in cardiovascular disease treatment. Qin et al used GNRs conjugated with matrix metalloproteinases-2 antibodies for IV-PA imaging detection of matrix metalloproteinases-2 in atherosclerosis plaque.[48] The matrix metalloproteinase-2 antibody can lead the GNRs specially target to the matrix metalloproteinases. As shown in **Figure 1.13**, the IV-PA images show the structure of the aorta and the strong intensity area is produced by the GNRs, which indicate the area containing matrix metalloproteinase. The area of the bright PA signal region is almost the same as provided by the silver staining and immunofluorescence, thus GNRs can be used as a promising probe for IV-PA imaging quantitative detection of distribution of matrix metalloproteinases-2.[48]

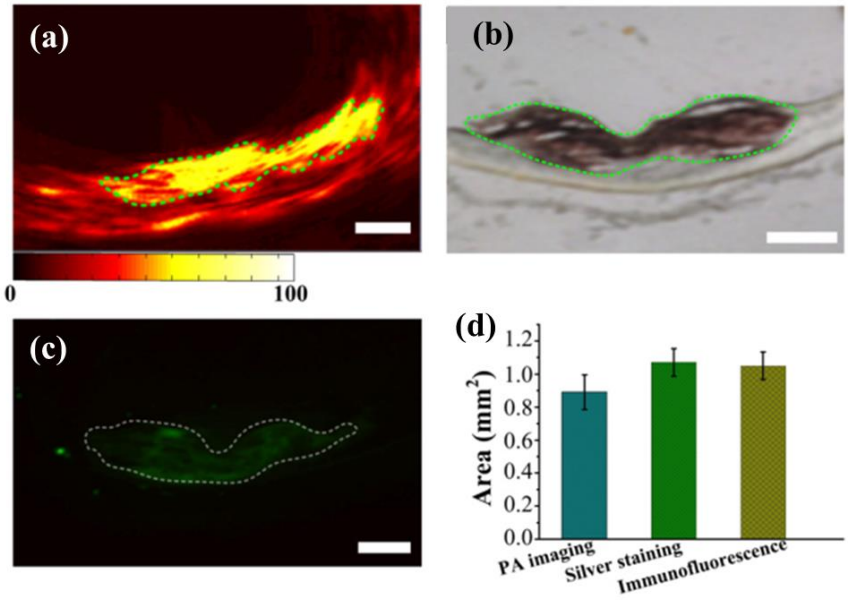


**Figure 1.13 (a)** The photoacoustic image of the aorta containing plaque **(b)** Histological section of silver stained (for labeling GNRs) aorta containing plaque from rabbits intravenously (ear) injected with GNRs (1 mL, 1 mM) following 6 h circulation. **(c)** The immunofluorescence result of matrix metalloproteinases-2 in the adjacent cross-sections. **(d)** Area of distribution of matrix metalloproteinases-2 measured using PA, histological section of silver staining, and immunofluorescence methods, respectively.[48]

### 1.3.2 Quantum dots (QDs)

QDs are nanosizes semiconductor crystals that have been extensively used in fluorescence imaging due to their small size, strong emission intensity and excellent photostability compared to the molecular probes.[55, 83-86] Their tunable optical properties obtained by changing their size make them interesting for bioimaging, and their strong emission intensity could provide deep tissue imaging. In this part, I will focus on the optical properties of the QDs and their applications for cardiovascular imaging.

*Optical properties:* For a bulk crystal, the optical properties of the material only depend on the chemical composition. However, when studying a nanosized crystal, the size of the particle starts to change the optical properties of the material. Particularly, in small semiconductors, the electronic structure changes from continuous bands to discrete or quantized electronic levels, due to the apparition of electron-hole bound system. The energy of the electron and hole quantized levels can be written as[87]

$$E_{l,n}^{e,h} = \frac{\hbar^2 {\phi_{l.n}}^2}{2m_{e,h}\alpha^2} \tag{1.5}$$

where $\hbar$ is the reduced Planck constant, $\phi_{l.n}$ are the root of the Bessel functions, which depend on the principal quantum numbers *n* (1, 2, 3,…) and the angular momentum quantum number (0, 1, 2, 3…, corresponding to *s*, *p*, *d*,…, orbitals)[88], $m_{e,h}$ is the electron and hole effective mass respectively, a is the crystal radius. Obviously, the energy of the electron and hole quantized level decreases when increases the nanocrystal size.

Besides the quantization energy, the Coulomb interaction between the bounded electron and hole also affects the optical properties of the QDs.[89] The Coulomb energy is on the order of $e^2/\varepsilon a$, where $\varepsilon$ is the semiconductor dielectric constant. Comparing the quantization energy and Coulomb energy, they all increase with decreasing the radius of the semiconductor but in different order. Therefore, in large QDs, the Coulomb interaction is much more important than the quantization energy. On the contrary, when the radius of the QDs is very small, the quantization energy produces main effect to the optical properties of the QDs.

Quantum confinement effects play an important role when the size of the nanocrystal reaches to the natural length of the electron and hole, this is known as Bohr radius $a_B$, which is calculated in analogy to the hydrogen atom Bohr radius $a_0$ (0.529nm). Thus $a_B$ is given as [89]

$$a_B = \varepsilon \frac{m_0}{m^*} a_0 \tag{1.6}$$

where $m^*$ is the effective mass, $m_0$ is the mass of the electron. When the electron and hole are confined together, they can form an exciton. The effective mass of the exciton is $m_{exc}^* = m_e^* \times m_h^*/(m_e^* + m_h^*)$, $m_e^*$ and $m_h^*$ is the effective of the electron and hole, respectively. After introduced the effective mass of electron, hole and exciton in Equation (1.6), we can get the Bohr radius for electron, hole and exciton respectively. For example, for the CdSe QDs, $m_e^*$ is 0.13 $m_0$, $m_h^*$ is 0.45 $m_0$, ε is 10.1, therefore, the exciton Bohr radius for CdSe QDs is 5.3 nm.[90] In case of PbS QDs, , $m_e^*$ is 0.087 $m_0$, $m_h^*$ is 0.083 $m_0$, ε is 17, the electron, hole and exciton Bohr radius ($a_{B,e}$, $a_{B,h}$ and $a_{B,\,exc}$) for PbS QDs is 10, 11 and 21 nm respectively.[91, 92] The Bohr radius determinates three kinds of quantum confinements regime.[91] When a > $a_B$, there is a weak confinement regime. In the intermediate confinement regime, the QDs crystal radius is less than

the electron Bohr radius but larger than the hole Bohr radius ($a_{B,h}$, < $a$ < $a_{B,e}$). Strong confinement regime happens when the QDs crystal radius is less than Borh radius ($a < a_B$), In this case, the exciton energy is given by

$$\hbar\omega_v = E_g + E_v^h(a) + E_v^e(a) - 1.8\frac{e^2}{\varepsilon a} \tag{1.7}$$

where $E_g$ is the energy gap of the semiconductor and it also depends on the size of the QDs, the Coulomb interaction is calculated by the first order perturbation theory[87].

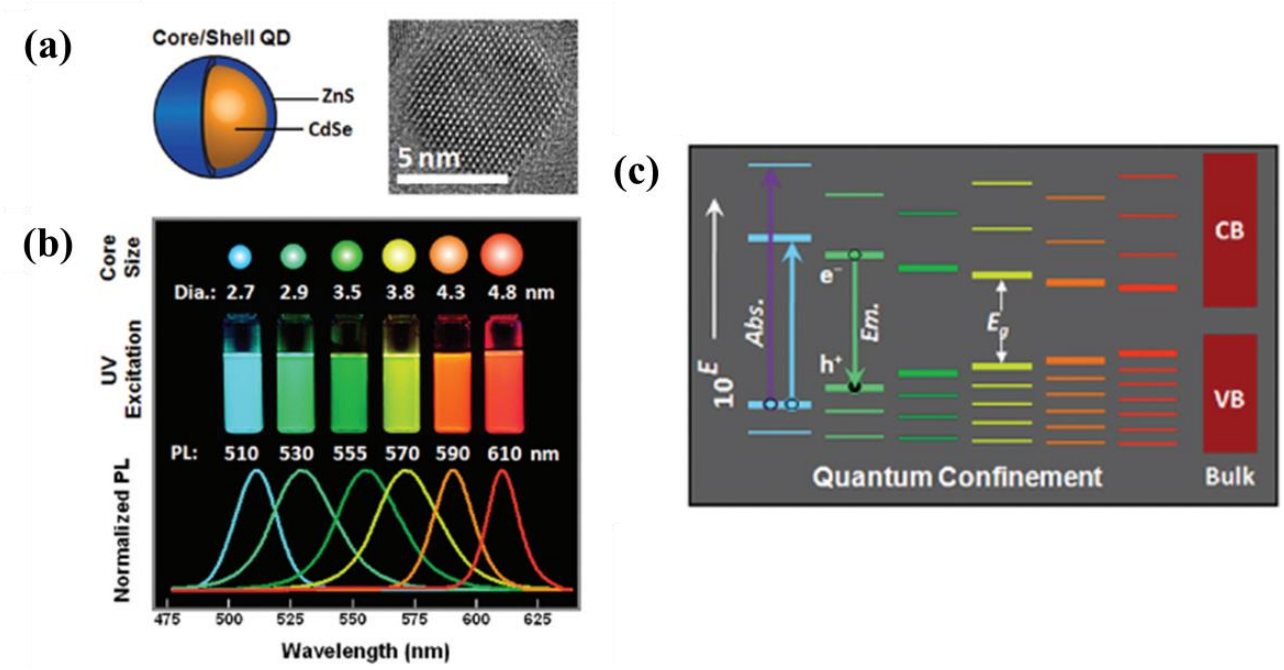


**Figure 1.14 (a)** Carton drawing and TEM a ZnS/CdSe QD. **(b)** Core size of ZnS/CdSe QDs and their corresponding fluorescence imaging and emission spectra. **(c)** The corresponding energy gap and energy level of the ZnS/CdS QDs corresponding to their core size.[93]

**Figure 1.14** shows the optical properties of ZnS/CdSe QDs.[93] In **Figure 1.14 (b)**, when the size of the core changes from 2.7 nm to 4.8 nm, the emission spectra show a red shift from 510 nm to 610 nm. Also in **Figure 1.14 (c)**, the quantum confinement of the exciton lead to a decreasing energy band gap when increases the core size. Therefore, by changing the size of the QDs, we can get the emission we want for specific applications. In the case of the PbS, as shown in **Figure 1.15**, the emission peak can be tuned from 752 to 1520 nm when increasing the size of PbS QDs from

2.35 to 5.61 nm.[94] Thus the emission spectra of PbS can be tuned from I-BW to III-BW, which will be very useful for different applications.

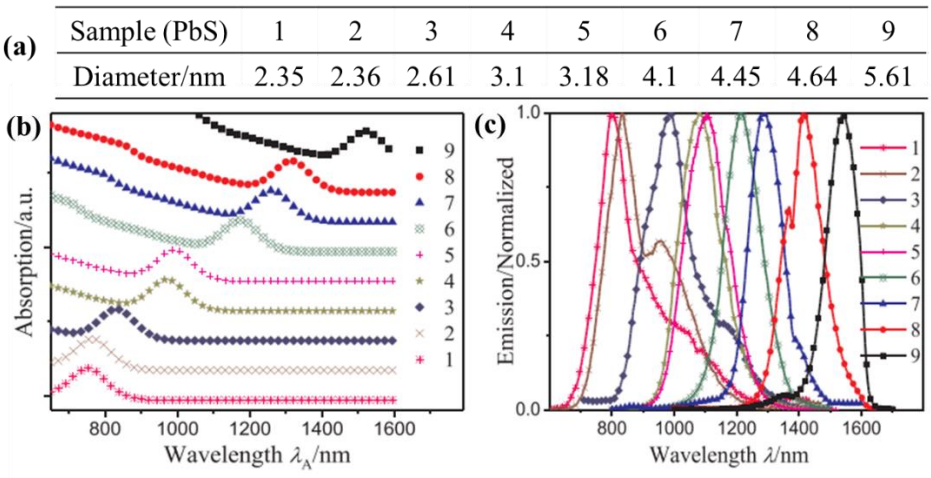


**Figure 1.15 (a)** Different size of PbS QDs. **(b)** Normalized absorption of PbS QDs. **(c)** Normalized emission spectra of PbS QDs.[94]

Applications

Compared to fluorescent dyes, QDs have some advantages, such as long Stokes shift, broad band excitation spectra, narrow emission bands and high photostability, thus they has been widely used for high resolution cellular imaging, single particle tracking of biological process and *ex* and *in vivo* imaging.[95, 96] Furthermore, different QDs can be excited by single light source, therefore, QDs can be used for simultaneously multicolor imaging.[97]

Particularly, QDs have been used for cardiovascular imaging. In 2016, Chenxin Wu and his coworkers used ICG@PEG-$Ag_2S$ for atherosclerosis targeting and imaging *in vivo*.[98] The $Ag_2S$ QDs show a strong emission in NIR-II (peaking at 1200 nm).[99] As shown in **Figure 1.16**, the infrared fluorescence imaging of the aortas show two bright areas, which indicate the atherosclerotic plaques and macrophages, these are due to the lipophilicity of the $Ag_2S$ QDs surface to the atherosclerosis environment.[98] The existence of the macrophages and atherosclerosis in these areas were convinced by the Hematoxylin–eosin (H&E) and mouse F4/80 antibody staining of the dissected aortas as shown in **Figure 1.16 (b)** and **(c)**.

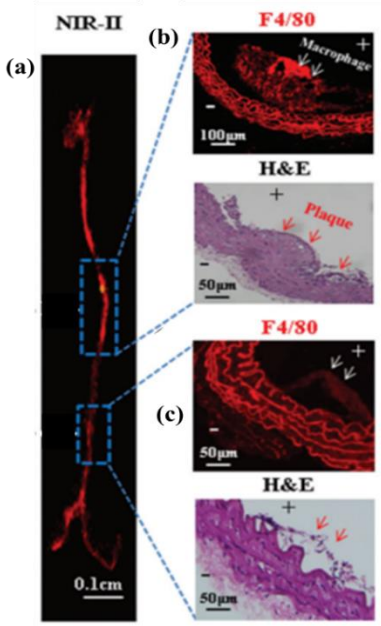


**Figure 1.16 (a)** NIR-II fluorescence imaging of the aortas, the aortas were harvested from the ApoE$^{-/-}$ mice after intravenous injection of ICG@PEG-$Ag_2S$. **(b, c)** Hematoxylin–eosin (H&E) and mouse F4/80 antibody staining of the dissected aortas corresponding to panel **(a)**. White arrows indicate macrophages and red arrows indicate atherosclerotic plaques.[98]

## 1.4 Targeting strategy

Targeting strategy is very important for improving the efficiency of NPs localizing to the disease site and avoiding the fast clearance of NPs by the liver. Based on the properties of NPs and different pathologies of disease, there are several targeting strategies that have been used to deliver the NPs to the disease sites.

### 1.4.1 Passive targeting strategy

*Enhanced vascular permeability*: Enhanced vascular permeability is one of the main mechanisms for passive targeting of diseases. This effect has been well investigated in cancer therapy, it also exists in atherosclerosis due to the inflammation and rapidly formed of the leaky microvessels in intima of the plaque. The vascular permeability allows NPs to penetrate the vascular wall and accumulate in the inflammation sites.[100] There are several factors that should be taken into consideration, such as the size, shape and surface coating of the NPs,[101, 102] and these factors affect the clearance and circulation time of NPs in the vascular.[100]

*Magnetically guided nanoparticles*: The magnetic NPs could be used to image the atherosclerosis plaque as they can be guided to the disease site by using an external magnetic field.[103, 104] This is the so called magnetically guided nanoparticles strategy. It is based on the enhanced vascular permeability, and could improve the margination and accumulation of NPs in the inflammation place.[100]

*Shear induced target*: For advanced atherosclerosis, one of the symptoms is the stenosis, which results in the change of the wall shear stress. Take advantage of this effect, the shear stress sensitive NPs can specially targeting to the plaques. Rui et al reported the use of up conversion NPs for molecular imaging of vulnerable atherosclerosis.[105] Based on the different wall shear stress in the mouse, the NPs can specially target low shear stress site, where has vulnerable plaques. These results have been confirmed by optical and MRI imaging, and the histological analyses.

### 1.4.2 Active targeting strategy

An scheme of the active targeting strategy has been given in **Figure 1.2**. The specially functionalized NPs could be used to target specific disease sites. In this section, some examples of using NPs to target endothelial cells and microphages have been discussed. More targeting strategies related to different imaging techniques are shown in **Table 1.1**.

*Endothelial cells*: Due to their directly exposure to the bloodstream, endothelial cells has been the main target of conjugated NPs for cardiovascular disease. Andrew et al studied the molecular imaging with OCT by using microparticles conjugated with different antibodies.[106] First they used tumour necrosis factor (TNF-α) to activate the human umbilical endothelial cells (HUVECs), this step helps the expression of the VCAM-1, platelet endothelial cell adhesion molecule (PECAM-1) and E-selectin on endothelial cells. The results show that under static conditions, NPs conjugated with antibody bind to PECAM-1, E-selectin, VCAM-1 and E-selectin+VCAM-1. Under flow conditions with increasing shear stress, PECAM-1-NPs bind great numbers than other antibody-NPs. Furthermore, the binding of NPs to endothelial cells has been study in *ex-vivo* coronary arterioles under different shear stress. The VCAM-1-NPs specially targeted to the TNF-α simulated arterioles. Due to the scattering properties of this NP, the binding of E-selectin+VCAM-1-NPs to the simulated endothelial cells show a high OCT intensity than basal without any binding NPs under different shear stress. Therefore, the OCT molecular imaging was

achieved by active targeting strategy.[106] By using another technique, photoacoustic imaging, Seunghan et al successfully detected and monitored the inflammatory response of HUVECs. After simulated by TNF-α, HUVECs could be expressed by cell adhesion molecules such as the ICAM-1 and E-selectin. The antibody-GNRs were used to target these molecules, due to the specific targeting and high absorption properties of these GNRs, a high PA signal was achieved for the simulated HUVECs, Therefore, PA imaging could be used to monitor the inflammation response by combining the active targeting strategy.

**Table 1.1** Contrast agents (CAs) for cardiovascular imaging

| CAs | Imaging techniques/conditions | $\lambda_{exc}$ (nm) | $\lambda_{em}$(nm) | Functionalization | Targeting | Disease | Refs |
|---|---|---|---|---|---|---|---|
| Cy 5.5 | *In vivo* fluorescence imaging | 550 | 680 | Thrombin | NA | Thrombosis | 107 |
| Cy7 | *Ex vivo* fluorescence imaging | 485 | 525 | Fibrin | NA | Atherosclerosis | 108 |
| Cy5.5 | *In vivo* and *ex vivo* fluorescence imaging | NA | NA | Profilin-I | NA | Atherosclerosis | 109 |
| $NaGdF_4$:Yb,Er | Visible fluorescence imaging. | 980 | 400-750 | Osteopontin | NA | Atherosclerosis | 105 |
| ICG@$Ag_2S$ | Fluorescence imaging (*ex vivo*) and PA (in vivo) | 800 | 1200 | C18/PEG | NA | Atherosclerosis | 110 |
| Gadolinium(III)–GNRs | PA (*In vitro*, *in vivo* and *ex vivo* ) | NA | 520, 710 | mPEG-SH | Macrophage | Atherosclerotic inflammation | 111 |
| GNRs | PA (*Ex vivo*) | 695 | 700 | polyclonal matrix metallopeptidase-2 antibody | Polyclonal matrix metallopeptidase-2 | Atherosclerotic plaques | 48 |
| GNRs | PA (*In vitro*) | 700 | 700 | anti-ICAM-1 | Human umbilical vein endothelial cells (HUVECs) | Inflammatory | 112 |
| GNSs | PA (*In vitro* and *in vivo*) | NA | 710 | VCAM-1 antibody | NA | Atherosclerotic plaque | 113 |
| GNPs | IV-PA (Phantom and *ex vivo*) | 680 | 530 | PEG | Macrophage | Atherosclerotic plaques | 114 |
| GNRs | PA (*In vitro*) | 715;800 | 715;800 | anti-ICAM-1 antibody and anti-E-selectin antibody | Human umbilical vein endothelial cells (HUVECs) | Endothelial inflammation | 115 |
| PbS QDs | OCT (*Ex vivo*) | 1320 | 1550 | DSPE-PEG-amine-coated | NA | NA | 116 |
| Nanorose | Photothermal OCT (*Ex vivo*) | 1328 | NA | Dextran | Macrophage | NA | 117 |
| Magnetic microspheres | Intravascular Magnetomotive-OCT | 1310 nm | NA | RGD | $\alpha_v\beta_3$ integrins | atherosclerotic plaque | 118 |
| Microparticles of iron oxide | OCT (*In vitro* and *ex vivo*) | 1250-1350 | NA | Anti-VCAM-1, E-selectin, PECAM-1 | HUVEC | atherosclerotic plaque | 106 |

**NA: Not available**

*Macrophages*: Macrophages play an important role in the atherosclerosis progression because they ingest the oxidized lipoproteins and lead to their differentiation into foam cells. Therefore, macrophages imaging could be serve as biomarker of the atherosclerosis processes.[119] High-density lipoprotein HDL in macrophages helps the transport of the cholesterol to the liver for excretion. Therefore, HDL-based contrast agents could be used to visualize macrophages. In 2013, Marrache and co-workers developed (HDL)-mimicking NPs to detect macrophages apoptosis *in vitro*. The core of these NPs contain QDs, which is used for optical imaging. The fluorescence microscopy imaging showed the apoptotic macrophages by using these NPs compared to the nontargeted NPs.[120]

## 1.5 Motivation

IV-OCT is a high resolution clinical technique to characterize the atherosclerosis plaque. However, due to lack of contrast agent, the molecular processes under atherosclerosis progression can not be visualized by IV-OCT. A strong demand of contrast agent to improve the IV-OCT contrast has been called by the physicians. Based on the OCT technique, which collects the backscattered light, NPs that could provide high backscattered light can be used to enhance the OCT contrast. Therefore, the GNPs with high backscattered efficiency visualized by IV-OCT are discussed in **Chapter 3**. The scatter properties determination of GNPs by photo-thermal method, numerical simulation, dark field microscopy, PA are included in **Chapter 4**. Molecular OCT imaging of the cells and tissue produced by GNSs was also achieved, the results and discussion are given in **Chapter 5**. The fluorescence imaging of the atherosclerosis which is based on the contrast agent could provide the molecular imaging of the atherosclerosis procession. Thus, the combination of the fluorescence imaging and IV-OCT imaging could help to improve the accurate treatment of the CVD. In this case, PbS QDs were evaluated as a contrast agent for fluorescence imaging and IV-OCT in **Chapter 6**.

# Chapter 2. Experimental techniques

## 2.1. Preparation of nanoparticles

### 2.1.1. Synthesis and functionalization of GNPs

GNSTs (surfactant-free) were synthesized by Dionysia Tsoutsi (Integrative Biomedical Materials and Nanomedicine Lab, Department of Experimental and Health Sciences (DCEXS), Pompeu Fabra University (UPF)). The synthesis process followed a seed-mediated growth protocol, as previously reported by Yuan *et al.*[121] The following chemicals were used: Tetrachloroauric acid tetrahydrate ($HAuCl_4 \cdot 4H_2O$), trisodium citrate dihydrate ($C_6H_5O_7Na \cdot 2H_2O$), silver nitrate ($AgNO_3$), L(+)-ascorbic acid, and hydrochloric acid (HCl), all of them purchased from Sigma-Aldrich and used without further purification. Water was purified using a Milli-Q system (Millipore). Aqua regia was used to clean all the glassware prior to use. Gold spheres, used as seeds, were prepared by adding 15 mL of 1 wt % citrate solution to a 100 mL boiling solution of $HAuCl_4$ (1 mM) under stirring and additional boiling for 15 min. This is a standard citrate-stabilized protocol producing wine-red colored gold sols with an average diameter of around 12 nm. Next, 1 mL of the above seed solution was added to a 100 mL of 0.25 mM $HAuCl_4$ solution containing 100 μL of 1 M HCl at room temperature and under moderate stirring. Immediately afterwards, the addition of 1 mL of 0.01 M $AgNO_3$ and 500 μL of 0.1 M ascorbic acid was performed simultaneously and the solution was stirred for 30 s producing dark blue-black colloids. The nanostar dispersions were centrifuged at 4500 rpm for 20 min, redispersed in MiliQ-water and kept in the dark at 4 °C for long-term storage.

### 2.1.2. Synthesis and functionalization of QDs

Commercial CANdots® Series C ($\lambda_{em}$ ~ 1600 nm) PbS QDs in a toluene dispersion (10 mg/mL, 1 mL) were added after careful sonication to $CHCl_3$ (5 mL) while stirring at 23 ºC. In a second flask 1,2-distearoyl-*sn*-glycero-3-phosphoethanolamine-*N*-[amino(polyethylene glycol)-2000] ammonium salt (DSPE-PEG-amine) (21 mg) was dissolved in $CHCl_3$ (10 mL) and after complete dissolution added dropwise to the first mixture. The combined mixtures were stirred for 2 h at 23 ºC and then the organic solvent was removed under reduced pressure. The obtained DSPE-PEG-amine-coated QDs were then dispersed in distilled $H_2O$

## 2.2. Basic characterization

### 2.2.1. Transmission electron microscopy (TEM)

TEM is a microscopy technique in which an electron beam is accelerated and focused in a specimen (thickness <100 nm). The directions of the electrons change when they interact with the atoms in the specimen, the scattered electrons thus produces an image. After magnified and focused, the image can be seen on a fluorescence screen. The resolution of the TEM is higher 0.1 ~ 0.2 nm, due to the de Broglie wavelength of the electrons.[122] TEM is now widely used in the chemistry, physics and biology.

The TEM we used in this work is a JEOL JEM 1010 microscope operating at 80 kV. Samples were prepared by placing one drop of a diluted suspension of the nanoparticles in water onto a carbon coated copper grid and leaving it to dry at room temperature. The size distribution of NPs were determined by using ImageJ software.

### 2.2.2. Total reflection X-ray fluorescence (TXRF)

The concentration of PbS QDs was determined by using TXRF. TXRF uses X-ray to excite the sample, which is put on the reflector, the angle between the incident beam and the reflector is less than the 0.06°,[123] thus the total incident photons are reflected. The X-ray fluorescence from the sample is detected by putting a detector above the reflector. The detection limits is less than $10^{-12}$ g.[124]

The Pb-content was determined on a Bruker TXRF S2 PicoFox system, excitation by a Mo K radiation. Calculations based on the size of the QDs and the PbS structure revealed the concentration after ligand-addition as 0.6 mg/mL.

### 2.2.3. Extinction spectroscopy

The room temperature extinction spectrum of the colloidal solutions of nanoparticles were measured with a double beam absorption spectrometer (Perkin Elmer Lambda1050).

### 2.2.4. Photoluminescence spectroscopy

The emission spectra of the PbS QDs was measured under excitation with a single mode fiber-coupled 1280 nm laser diode. A long pass filter 1350 nm was put at the entrance slit of the Andor Sahmrock 193i spectrometer to remove the excitation laser. After being analyzed by the monochromator, the luminescence signal was collected by an InGaAs camera (Andor Idus DU490A).

### 2.2.5. Dark field microscopy (DFM) imaging system

The DFM imaging system used in this thesis, shown in **Figure 2.1** is composed of optical microscope (NIKON Eclipse E400), dark field condenser (Nikon, dry NA 0.95-0.80), and different objectives 50X (SLMPlan N, NA 0.35 WD 18 mm ), 40X (NA0.65, WD 0.65 mm), 20X (NA 0.40, WD 3.8 mm), and 10X (NA 0.25, WD 6.1 mm). The signal is collected by InGaAs infrared camera (top) and monochromatic (Shamrotic 193i). The visible image is detected by the EMCCD camera (iXon Ultra Andor) which is connected to the monochromator, and the infrared emission is detected by an iDus InGaAs detector (Andor). A filter wheel (Thorlabs) is located in front of the infrared camera, in order to select the wavelength at which DFM are acquired. This DFM is specially designed for experiment under flow conditions. A syringe pump is used to inject the solution of GNPs in the flowing chamber. Meanwhile, a temperature controller (Warner, TC-324C) is used to maintain the temperature in the flow chamber temperatures compatible with cell aviability. The flow chamber (RC-30WA) is located on the platform bewteen the dark field condenser and the objective.

The DFM working principle is shown in **Figure 2.2 (a)**. A halogen lamp is used to illuminate the specimen in the flowing chamber, and the central part of beam is blocked, so that only the light scattered by the specimen can enter the objective. In our case, the specimen is located in the flow chamber. The components of the chamber are shown in **Figure 2.2 (b)**, which contains a pressure plate on the top, a top coverslip plate, a top cover slip, a chamber forming gasket, a bottom cover slip, a base, and a stage adapter. Vacumn grease is used to connect the coverslip to the top coverslip plate and base. The temperature of the base is kept constant by the temperature controller (**Figure 2.1**). The cells are cultured on the bottom cover slip or top cover slip.The GNPs are introduced in the flow chamber by the small tube in the top coverslip plate.

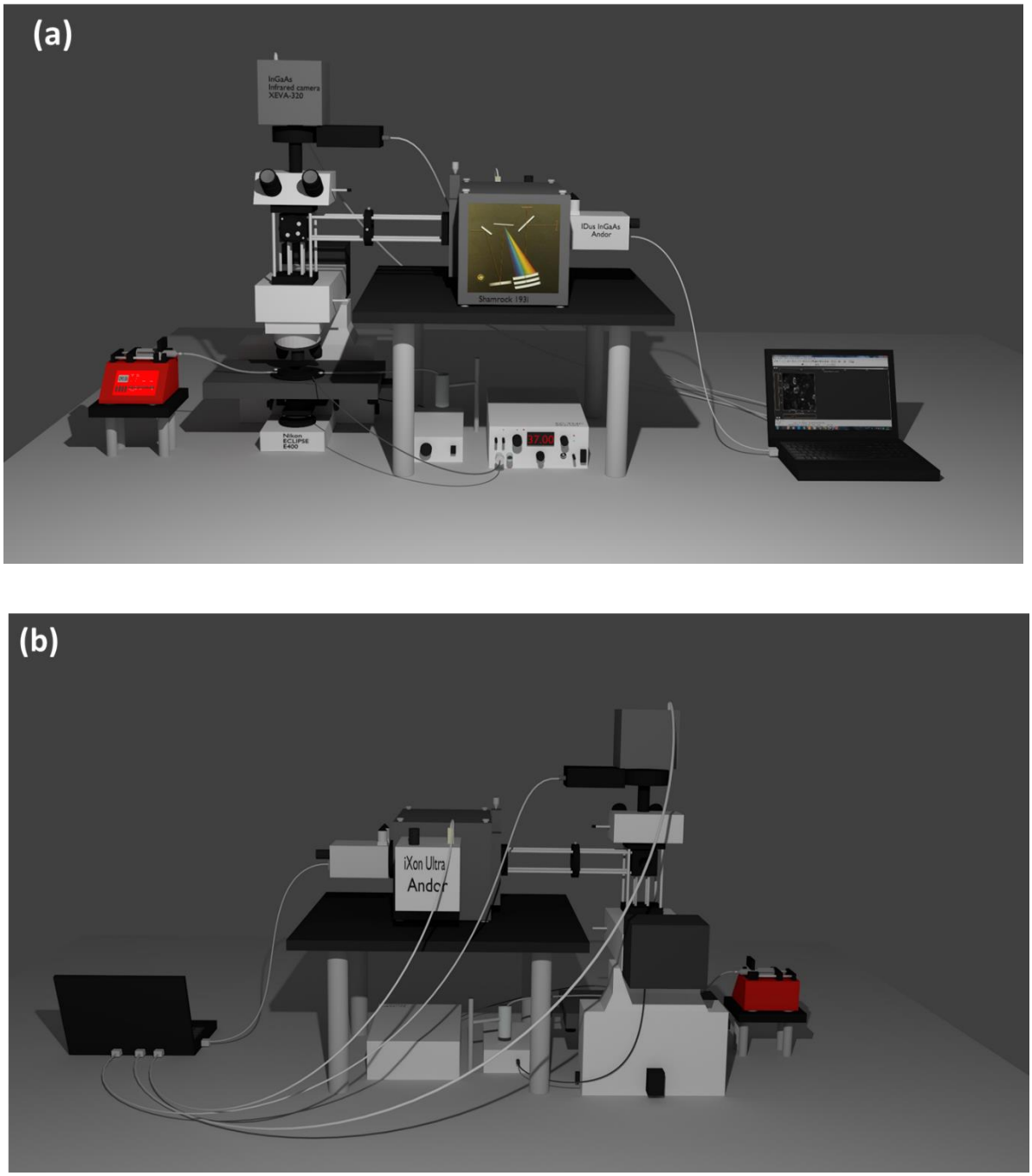


**Figure 2.1** Dark field microscopy imaging system and flowing configuration **(a)** front and **(b)** back side.

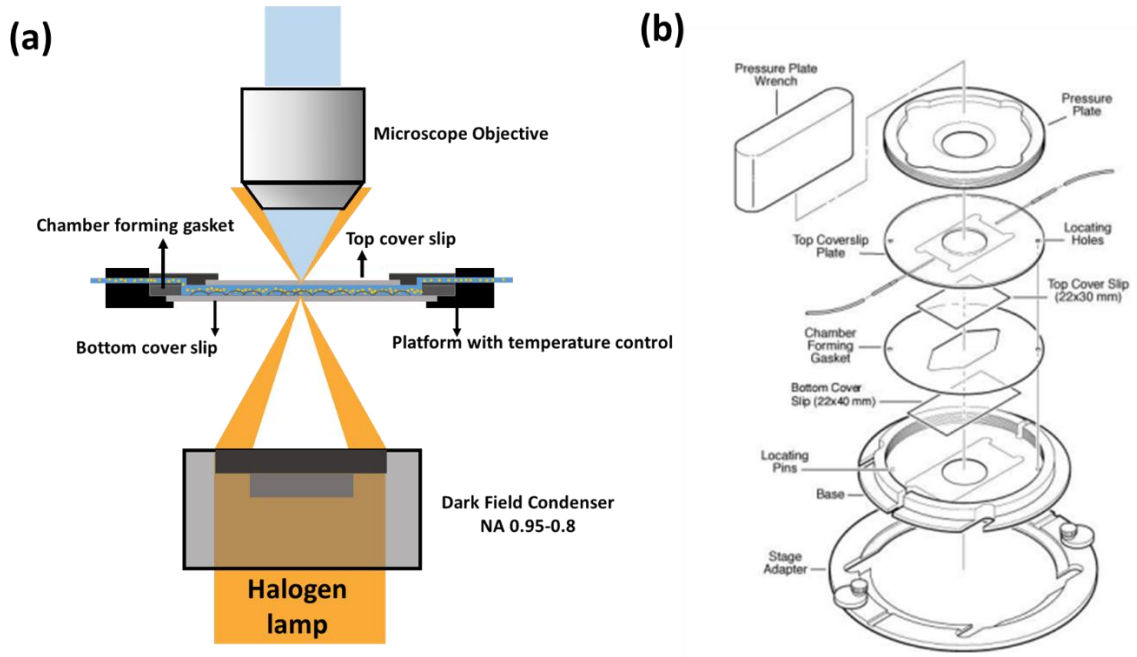


**Figure 2.2 (a)** DFM schematic for flowing experiment. **(b)** RC-30WA flowing chamber

### 2.2.6. Photothermal method and experiments

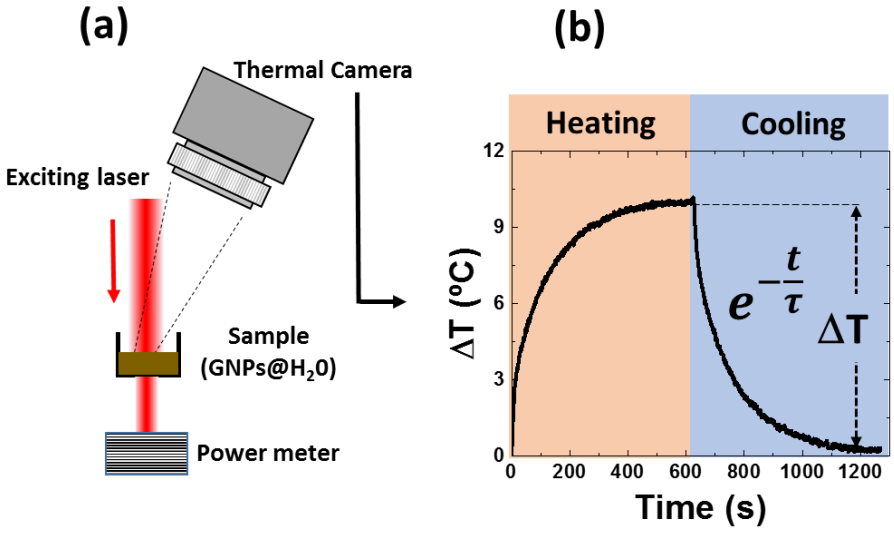


**Figure 2.3 (a)** Schematic diagram of the experimental set-up used for the determination of the scattering efficiency of GNPs under optical excitation in the II-BW. **(b)** Representative heating and cooling curve obtained from an aqueous solution of GNRs under 1280 nm optical excitation.

The photo-thermal experiments were used to determine the absorption and scattering efficiencies of the GNPs. The experimental setup is shown in **Figure 2.3**.

Briefly, a laser beam of power $P_0$ at the required wavelength is directed onto a cuvette containing a water solution with a certain concentration of GNPs (from now on the sample). A power meter measures the output power $P$ at the exit face of the sample. A fraction of the incident laser power is attenuated by the GNPs depending on their scattering and absorption properties.[125] Hence, the transmitted power can be defined as follows:

$$P = P_0 10^{-OD} \tag{2.1}$$

where $OD$ is the optical density of the sample that can be determined at different wavelengths from the experimentally measured extinction spectra of each sample. We used three different continuous wave (CW) laser diodes emitting at 808 nm, 980 nm, and 1280 nm. The fraction of laser power absorbed by the sample will result in an increment in sample´s temperature that is measured by using a thermal camera (FLIR E40bx) and record by FLIR tool program, as it is schematically indicated in **Figure 2.3 (a)**. The laser was kept on about 10 minutes (heating part of the **Figure 2.3 (b)**) until the temperature of the dispersion had reached a steady value. Then, it was turned off and the temperature was monitored until it was equal to the room temperature, thus we obtained the heating/cooling cycles, as the one shown in **Figure 2.3 (b)**. The experimental determination of $\eta_a(\lambda)$ requires the determination of temperature heating, $(\Delta T)_{max} = T_{max} - T_{amb}$ (where $T_{max}$ is the maximum temperature and $T_{amb}$ the ambient temperature) and the cooling decay time ($\tau$). Both magnitudes are schematically indicated in **Figure 2.3 (b)**. The heat rate balance equation accounting for these processes can be written as follows[126]:

$$mC_p \frac{dT}{dt} = Q_{GNP} + Q_r - Q_{ext} \tag{2.2}$$

where $m$ is the solvent mass, $C_P$ the constant pressure heat capacity, $T$ the sample temperature and $Q_{GNP}$ the heat power delivered by the gold nanoparticles in the water solution. In Equation (2.2), $Q_r$ is the heat power delivered by the solvent and the cuvette walls that can be measured for each particular case, and $Q_{ext}$ represents the external heat power losses, due to the temperature difference $\Delta T$ between the sample and the surrounding environment. This term can be expressed as:

$$Q_{ext} = hA\Delta T \tag{2.3}$$

where *h* is the heat-transfer coefficient and *A* is the cross sectional area for radiative heat transfer. As we have assumed (no luminescence) that the heat power delivered due to the GNPs is equal to the absorbed power, we can write:

$$Q_{GNP} = P_{abs} = P_0(1 - 10^{-OD})\eta \tag{2.4}$$

When the laser is turned off ($Q_{GNP}$=$Q_r$=0), Equations (2.2) and (2.3) lead to:

$$dt = -\frac{mC_p dT}{hA\Delta T} \tag{2.5}$$

whose solution is:

$$\Delta T = (\Delta T)_{max} \cdot e^{-t/\tau} \tag{2.6}$$

where the experimentally measurable decay time constant, $\tau$, is given by:

$$\tau = \frac{mC_p}{hA} \tag{2.7}$$

To determine the heating efficiency we can rewrite Equation (2.1) under steady state conditions (i.e. *dT/dt*=0) taking into account Equations (2.3) and (2.4):

$$\eta_a = 1 - \eta_s = \frac{\frac{mC_p\Delta T_{max}}{\tau} - Q_r}{P_0(1 - 10^{-OD})} \tag{2.8}$$

### 2.2.7. Optical coherence tomography

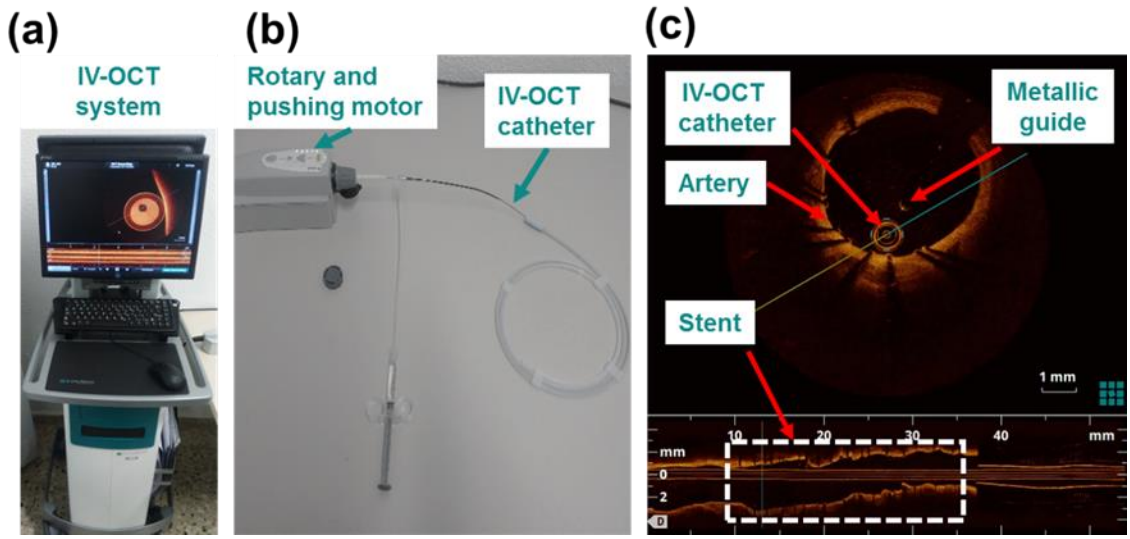


**Figure 2.4 (a)** IV-OCT system. **(b)** IV-OCT catheter and rotary and pushing motor. (c) IV-OCT cross-sectional image of artery.

For the experiments, the IV-OCT system used in this work is a commercially available system for intravascular imaging ((Dragonfly™ OPTIS™ Imaging Catheter. St Jude Medical.)), which is used for the treatment of patients at the Interventional Cardiology Unit University Hospital. **Figure 2.4** show the real IV-OCT system in our lab, which is consist of computer system, rotary and pushing motor and IV-OCT catheter. A cross-sectional image of artery is also presented in **Figure 2.4 (c)**, in which we can see the IV-OCT catheter, the structure of the artery, a stent that is used to expand the artery and metallic guide that is used to introduce the IV-OCT catheter. **Figure 2.5 (a)** shows a schematic diagram of the OCT clinical system. A compact 1320 nm wavelength laser is coupled to a single mode fiber (SMF) that is in turn incorporated into a 0.9 mm diameter catheter. The SMF inside the catheter is optically coupled to a frequency domain interferometric system that is constituted by different lenses and a rotating micro reflector that deviates the 1320 nm laser beam 90º in respect to the SMF. The whole optical system is externally driven so that it can to rotate at a constant angular frequency. As a consequence, as it is illustrated in **Figure 2.4**, the OCT catheter is continuously scanning the 1320 nm beam over a cross sectional plane perpendicular to it. The same optical system is used to collect the back-scattered 1320 nm signal and to couple it into the SMF. The collected signal is then sent to a fixed-arms interferometer equipped with a low

loss spectrometer for frequency domain OCT. The nominal axial resolution of the clinical intravascular OCT used in this work was close to 15 µm. In addition, the hydrophobic coated OCT catheter is mechanically and optically coupled to a motorized unit, allowing for pull-back imaging by retracting the catheter a total length of 5 cm at a speed of 20 mm/s. The scan diameter of the OCT is 10 mm. The maximum frame rate and lines per frame achievable by our OCT system are 100 and 500, respectively. The emission spectrum of the OCT laser is included in **Figure 2.5 (b).** The OCT spectrum consists of two lines, one at 1320 nm and another one at around 650 nm. This second line arises from the fact that the OCT catheter incorporates a visible (red) laser that it is used by clinicians to check if the catheter is fully operative before introducing it into the patient.

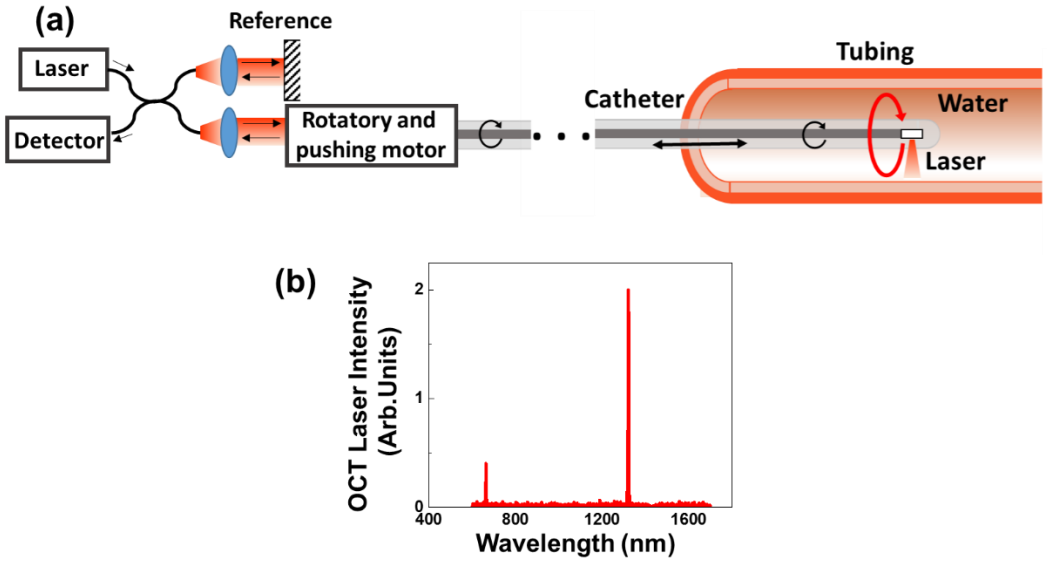


**Figure 2.5 (a)** Clinical IV-OCT set-up used all along in this work. **(b)** OCT laser spectra of the IV-OCT

The basic scheme of the low coherence interferometry (Michelson interferometry) used in OCT is shown in **Figure 2.6**. The light source is a polychromatic plane wave with the electric field $E_i = s\,(k,w)e^{i(kz-wt)}$. Here, $s\,(k,w)$ is the electric field amplitude, $k$ is the wavenumber and $w$ is angular frequency. The incident light is split by the beamsplitter into the sample and reference arms into two equal electric field. After returning from the reference reflector and the sample, the electric field for each arm is $E_R = \frac{E_i}{\sqrt{2}} r_R e^{i2kz_R}$ and $E_S = \frac{E_i}{\sqrt{2}}\left[r_S(z_S) \otimes e^{i2kz_S}\right]$, respectively. Where $r_R$ and $r_S(z_S)$ are the electric field reflectivity of the reference reflector and samples, $z_R$ and $z_S$ are the distance from the reference and sample arms to the beamsplitter, $\otimes$ denotes convolution, the

factor of 2 in the exponential is due to the path length in each arms. The returned light from the sample arm is called backscattered light. It interferes after the beam splitter and the result of the interference is detected by the detector, and produce a photocurrent, which can be expressed as $I_D(k,w) = \frac{\rho}{2}\langle|E_R + E_S|^2\rangle$. Here, ρ is sensitivity of the detector, the factor of 2 reflects the second pass of each field through the beamsplitter.[127] The received electric signal indicates the reflectivity profile at different depth of the sample, this reflectivity profile is called A scan, which contains information of spatial dimensions and location of structure. When the sample arm scans in lateral, a cross-sectional tomography at each depth is achieved, this is B scan. Thus two dimensional cross-sectional image of the sample is achieved by the OCT.

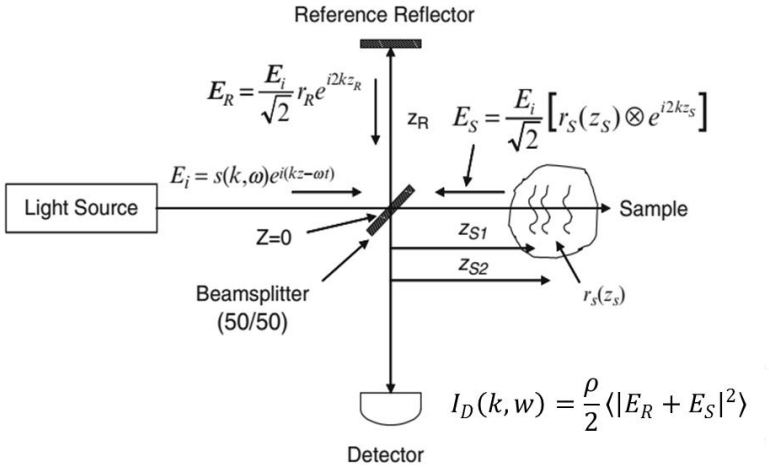


**Figure 2.6** Schematic of Michelson interferometry used in OCT[127]

Normally, the electric field reflectivity $r_S(z_S)$ in the biological tissue is continuous. Therefore the $r_S(z_S)$ could be written as $r_S(z_S) = \sum_{n=1}^{N} r_{Sn}\delta(z_S - z_{Sn})$, where $r_{Sn}$ corresponds to its electric field reflectivity $r_{S1}$, $r_{S2}$…, and pathlength from the beamsplitter to sample $z_{S1}$, $z_{S2}$…. The power reflectivity from each reflector in the sample and from reference reflector is given by the magnitude squared of the electric field reflectivity,[127] such as $R_R = |r_R|^2$ and $R_{S1} = |r_{S1}|^2$, therefore, $r_S = \sqrt{R_S(z_S)}$. The $r_S$ is reintroduced into the electric field from sample arm, thus $E_S = \frac{E_i}{\sqrt{2}}\left[\sum_{n=1}^{N} r_S(z_S)e^{i2kz_{Sn}}\right]$, and the detector current can be given:

$$I_D(k,w) = \frac{\rho}{2}\left\langle \left| \frac{s(k,w)}{\sqrt{2}} r_R e^{i(2kz_R - wt)} + \frac{s(k,w)}{\sqrt{2}} \sum_{n=1}^{N} r_{Sn} e^{i(2kz_{Sn} - wt)} \right|^2 \right\rangle \quad (2.9)$$

The angular frequency *w* is eliminated because the oscillation is so fast that the detector is not able to respond. Therefore, by using the Euler's rule: $e^{ix} = \cos x + \sin x$, the detector current can be written:[127]

$$\begin{aligned} I_D(k) &= \frac{\rho}{4}[S(k)(R_R + R_{S1} + R_{S2} + \cdots)] \text{ "}DC\ terms\text{"} \\ &+ \frac{\rho}{2}\left[S(k)\sum_{n=1}^{N}\sqrt{R_R R_{Sn}}(cos[2k(z_R - z_{Sn})])\right] \text{ "}Cross - correlation\ Terms\text{"} \\ &+ \frac{\rho}{4}\left[S(k)\sum_{n\neq m=1}^{N}\sqrt{R_{Sn} R_{Sm}}(cos[2k(z_{Sn} - z_{Sm})])\right] \text{"Auto} \\ &- \text{correlation Terms".} \end{aligned} \quad (2.10)$$

Here, $S(k) = \langle |s\ (k,w)|^2 \rangle$, which represents the power spectral dependence of the light source.[127] In Equation (2.10), the DC terms consists of the power spectral dependence of the light source multiplied by the power reflectivity of the reference reflector plus the sum of the sample reflectivities. It is an offset that is pathlength-independent to the detector current. The cross correlation terms, also called the interferometric terms, strongly depend on the light source wavenumber and the path length difference between the sample and reference arms. This is an interesting part for OCT imaging and is less intense than the DC terms. The auto-correlation terms is produced by the interference between the different sample reflectors. The best way to decrease the auto-correlation effect is to select the proper reference reflectivity to increase the contribution of the DC and interferometric terms in detector current. Therefore, a real detector current as function of wavenumber is well explained.

There are two kinds of OCT system, time domain OCT (TDOCT) and Fourier domain OCT (FDOCT). In TDOCT system, the light source is a broadband continous wave. The reference arm

consists of a mirror, which scans in length ($z_R$) in order to reconstruct the sample reflectivity profile, the reflected light from the reference and sample are recombined after pass the beamsplitter, and their interference fringes are detected by a single channel photoreceiver. The detector current $I_D(z_R)$ in TDOCT can be obtained by the integration of Equation (2.10) over all $k$:

$$I_D(\mathrm{z}_R) = \frac{\rho}{4}[S_0(R_R + R_{S1} + R_{S2} + \cdots)] \text{ "DC terms"}$$

$$+\frac{\rho}{2}\left[\mathrm{S}_0 \sum_{\mathrm{n=1}}^{\mathrm{N}} \sqrt{\mathrm{R_R R_{Sn}}}\, e^{-(z_R - z_{Sn})^2 \Delta k^2} (\cos[2k(z_R - z_{Sn})])\right] \quad (2.11)$$

"$Fringe\ Bursts$".

Here, $S_0 = \int_0^\infty S(k)dk$ is the integrated power of the light source. When the reference reflector distance $z_R$ is equal to the sample distance $z_{S1}$, for sample at position $z_{S1}$, the detector current is $I_D(\mathrm{z}_R) = \frac{\rho}{4}[S_0(R_R + R_{S1})] + \frac{\rho}{2}\left[\mathrm{S}_0\sqrt{\mathrm{R_R R_{S1}}}\right]$, as shown in **Figure 2.7**. In OCT system, a Gaussian-shaped light source spectrum is used due to the Fourier transform properties. The power of light source S($k$) and its inverse Fourier transform γ(z) are

$$\gamma(\mathrm{z}) = e^{-z^2 \Delta k^2} \overset{F}{\leftrightarrow} S(k) = \frac{1}{\Delta k\sqrt{\pi}} e^{-\left[\frac{(k-k_0)}{\Delta k}\right]^2}. \quad (2.12)$$

Here, $k_0$ ($k_0$=2π/λ$_0$) is the central wavenumber of the Gaussian shaped light source spectrum. Δ$k$ is spectral bandwidth, which is equal to half-width of the spectrum at 1/e of its maximum intensity. For the inverse Fourier transform γ(z), the full width at half the maximum (FWHM) is called "coherence length", $l_c$. Based on (2.12), we use 1/2 to substitute γ(z), then 1/2 $l_c$ is $\sqrt{\ln(2)}/\Delta k$.The coherence length in OCT is also called axial resolution, which can be expressed as $2\sqrt{\ln(2)}\,\lambda_0^2/\pi\Delta\lambda$.[127], therefore, the coherence length $l_c$ is:

$$l_c = \frac{2\sqrt{\ln(2)}}{\Delta k} = \frac{2\sqrt{\ln(2)}}{\pi}\frac{\lambda_0^2}{\Delta\lambda}. \quad (2.13)$$

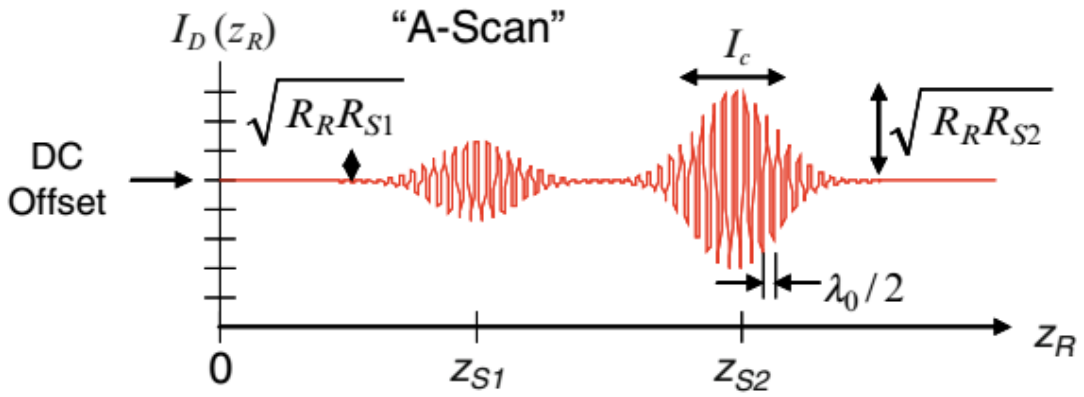


**Figure 2.7** A scan resulting from TDOCT[127], it includes DC offset, and the fringe burst between the light from the reference beam and sample beam at different distances ($Z_{S1}$ and $Z_{S2}$).

In the case of FDOCT, the reference beam is fixed, and the detector current is depend on the wavenumber. A Fourier analysis is used to reconstruct the reflectivity profile. There are two kinds of OCT based on the light source and detector. Spectral domain OCT (SDOCT), where a broadband light source and detector array are used, which allows the simultaneously capture of all spectral components of $I_D$(k), and swept source OCT, also called optical frequency domain imaging (OFDI), where a narrowband swept laser source is used. When the wavenumber of the source is swept, the spectral component of $I_D$(k) are captured in a single detector as function of time.[127]

Given the Fourier transform relation $\frac{1}{2}\left[\left(\delta(z+z_0)+\delta(z-z_0)\right)\right] \overset{F}{\leftrightarrow} \cos kz_0$ and the convolution property of Fourier transforms $x(z) \otimes y(z) \overset{F}{\leftrightarrow} X(k)Y(k)$, the inverse Fourier transform of Equation (2.10) will be

$$i_D(k) = \frac{\rho}{4}[\gamma(z)(R_R + R_{S1} + R_{S2} + \cdots)] \text{ "DC terms"}$$

$$+\frac{\rho}{4}\left[\gamma(z) \otimes \sum_{n=1}^{N} \sqrt{R_R R_{Sn}}\left(\delta\left(z \pm 2(z_R - z_{Sn})\right)\right)\right] \qquad (2.14)$$

"Cross-correlation Terms"

$$+\frac{\rho}{8}\left[\gamma(z)\otimes\sum_{n\neq m=1}^{N}\sqrt{R_{Sn}R_{Sm}}\left(\delta\left(z\pm 2(z_{Sn}-z_{Sm})\right)\right)\right]$$

$$"Auto-correlation\ Terms".$$

The resulting Fourier domain "A-scan" is shown in **Figure 2.8**.[127] At the zero position, only DC term appears in the detector current, this means the reflectivity profile appears at position of $z_R$, this is different from that of TDOCT, which appears at the beamsplitter. The distance different between the reference reflector and the sample is doubled, this is due to the fact that the interferometer measures the go and back distance to both reflectors.

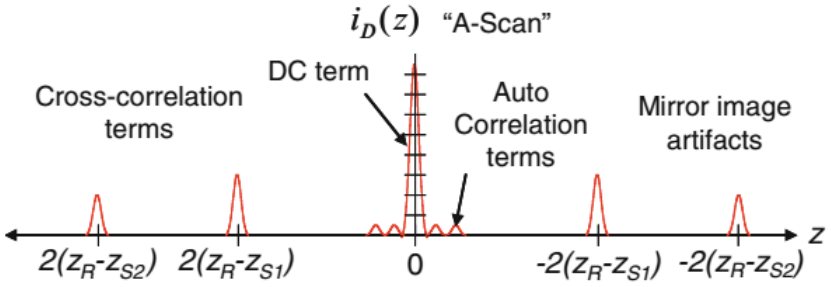


**Figure 2.8** A-scan resulting from FDOCT.[127]

**Table 2.1** Comparison between TDOCT and FDOCT

| Specifications | TDOCT | FDOCT |
|---|---|---|
| Axial scans/s | 5,000–10,000 | ~100,000 |
| Lines/frame | ~200 | ~500–1,000 |
| Max. frame rate, fps | 20 | ~200 |
| Max. pullback speed, mm/s | 2 | 20 |
| Axial resolution, μm | 15 | 10-15 |
| Lateral resolution, μm | 90 | 20-40 |
| Tissue penetration, mm | 1.5-3 | 2-3.5 |

Let's see the differences between TDOCT and FDOCT, the specifications of the TDOCT and FDOCT are shown in **Table 2.1**.[24] First, both of them show a high axial resolution than that of intravascular ultrasound (IVUS), in IVUS, the axial resolution is around 100μm.[128] Second, the

FDOCT system is faster than TDOCT, which is due to the fixed mirror in the reflector arms and the variable frequency light source or swept laser in FDOCT system. The IV-OCT is developed based on the FDOCT.

IV-OCT cross-sectional image analyze

*Integrated OCT intensity*: The IV-OCT video was imported in the ImageJ software, then an area without catheter , but inside the tubing was selected in the IV-OCT cross sectional image, we added this selected area in the ROI, and used the multi measure option to measure the intensity. The integrated intensity, intensity per pixel, maximum and minimum intensity could be obtained at the same time.

*Individual spot analysis*: Here we show you an example of how we analyzed the HeLa cells incubated with GNSs. The IV-OCT video was imported in the ImageJ software, first we need select the area where has GNSs and cells (inside the tubing) by change the contrast of the tubing and the catheter to zero (Brightness /Contrast option, adjust the minimum from 0 to 255). Then we change the image type to 8-bit. After this, we adjust the threshold from 0-255 to 37-355, because the threshold is the OCT intensity, and the intensity of the background is around 37, therefore, we adjust the threshold to remove the effect of the background. The statistics are carried out by using the analyze particles option, the size (pixel^2) is set to 3-30, as the size of the GNSs and cells are large than 1 pixel. Select the display results, and press ok, you will have the number of spots and max intensity per spot. Save it, import it to origin and do the frequency counts, you will have the number of spots for each spot intensity.

### 2.2.8. Infrared fluorescence imaging

For fluorescence imaging, the IV-OCT laser was used as an excitation source, a XEVA-320 infrared camera was used to take the infrared fluorescence imaging. This camera is based on an InGaAs two-dimensional array cooled down to 0 ºC that makes the detection of fluorescence images in the 900-1700 nm spectral range possible. A long pass filter 1350 nm was used to remove the effect from IV-OCT laser.

### 2.2.9. Photoacoustic experiment

The photoacoustic experiment was carried out in Optoelectronics and Laser Technology Group (GOTL), Universidad Carlos III de Madrid. With the permission from Prof. Horacio Lamela Rivera, and help by Luca Leggio and Daniel Gallego.

The photoacoustic signals were obtained by using a fiber-coupled Nd:YAG laser operating at 1064 nm and providing 8 ns width pulses as excitation source. The laser had a repetition rate of 1 kHz and a pulse energy of 10.5 μJ, leading to an average power of 10.5 mW. The GNPs were placed in a cuvette with thickness of 4 mm. In order to perform comparable measurements, the concentration of GNPs in the solutions was adjusted to provide an optical density (O.D.) of 10 at the laser wavelength (1064 nm). The photoacousti signals generated in the sample were detected by an ultrasound transducer mechanically attached to the cuvette. The signal generated by the ultrasound transducer was sent to a 40 dB pre-amplifier and collected by a digital oscilloscope.[129]

Basically, PA is also called optoacoustic or thermoacoustic imaging. In optoacoustic imaging, the photoacoustic signal is induced by the light, while in thermoacoustic imaging, the PA signal is produced by the radiofrequency.[37] For intravascular photoacoustic imaging (IV-PA), the light is delivered by an optic fiber and the signal is collected by the transducer in the same optic fiber. This technique is used for imaging the plaque structure and its composition in atherosclerosis.

An image of the tissue can be achieved by scanning the ultrasound.[38] The PA source strength $p_0$ can be estimated by

$$p_0 = \left(\beta c^2 / C_p\right)\mu_a F = \Gamma \mathrm{A}, \tag{2.15}$$

where $\beta$ is the isobaric volume expansion coefficient, $c$ is the speed of the sound in vacuum, $C_p$ is the specific heat at constant pressure of the sample, $\mu_\alpha$ is the absorption coefficient of the sample, $F$ is local energy density, $\Gamma$ is the Grüneisen parameter: $\Gamma = \beta c^2 / C_p$, A is the local energy deposition density: $\mathrm{A} = \mu_a F$.[37, 38]

## 2.3. *In vitro* experiment

### 2.3.1. HeLa and Jurkat cells; culture and incubation with Gold Nanoshells (GNSs)

Two different cell lines were investigated, i.e., HeLa cells and Jurkat cells. HeLa cells are an immortal cell line derived from human cervical cancer cells, with an epithelial phenotype. These cells divide an unlimited number of times *in vitro* under minimal survival conditions; accordingly, they are commonly used for cancer research[130]. In addition, as is typical for cancer cells, they are able to take up nanoparticles by passive targeting, usually by endocytosis. HeLa cells (ATCC CCL-2) were grown in Dulbecco's modified Eagle's medium with 10% fetal bovine serum (FBS). Jurkat cells are an immortalized line of human T lymphocytes. They (ATCC TIB 152) were grown in RPMI 1640 medium with 10% FBS. Both cell lines were cultured at 37 °C under 5% $CO_2$ and 95% humidity. Cells in exponential growth were used throughout all experiments. Incubation experiments were performed at 37 °C for 24 h using PBS solutions containing various concentrations of GNSs (0.05, 0.1, 0.5, 2.5, and 5 μg/mL). After incubation, cells were washed several times to remove excess GNSs that did not adhere or were not internalized by the cells. After incubation with GNSs, HeLa cells were trypsinized. The detached cells were resuspended in PBS and centrifuged at 1,000 rpm at 4 °C for 5 min. This step was repeated three times to eliminate excess NPs. Jurkat cells were resuspended without trypsinization in PBS and subjected to three cycles of centrifugation in order to eliminate excess GNSs.

### 2.3.2. Human Mammary Epithelial Cells culture, activation and evaluation of molecular expression

Human microvascular endothelial cell line (HMEC-1) was obtained from the American Type Culture Collection (Teddington, UK; ATCC, No CRL-3243) and was grown in 5% $CO_2$ at 37 °C in a medium containing endothelial basal medium MCDB 131 (Gibco), 10% heat-inactivated FBS, 1% L-glutamine, 100 μg/ml each penicillin and streptomycin, 100 nM hydrocortisone (Corning), and 10 ng/ml human epidermal growth supplement (EGF; Gibco BRL). For flow cytometry assay, the cells were cultured on 6-well plates (FALCON, USA). Only cells with less than 12 passages were used in the present study.

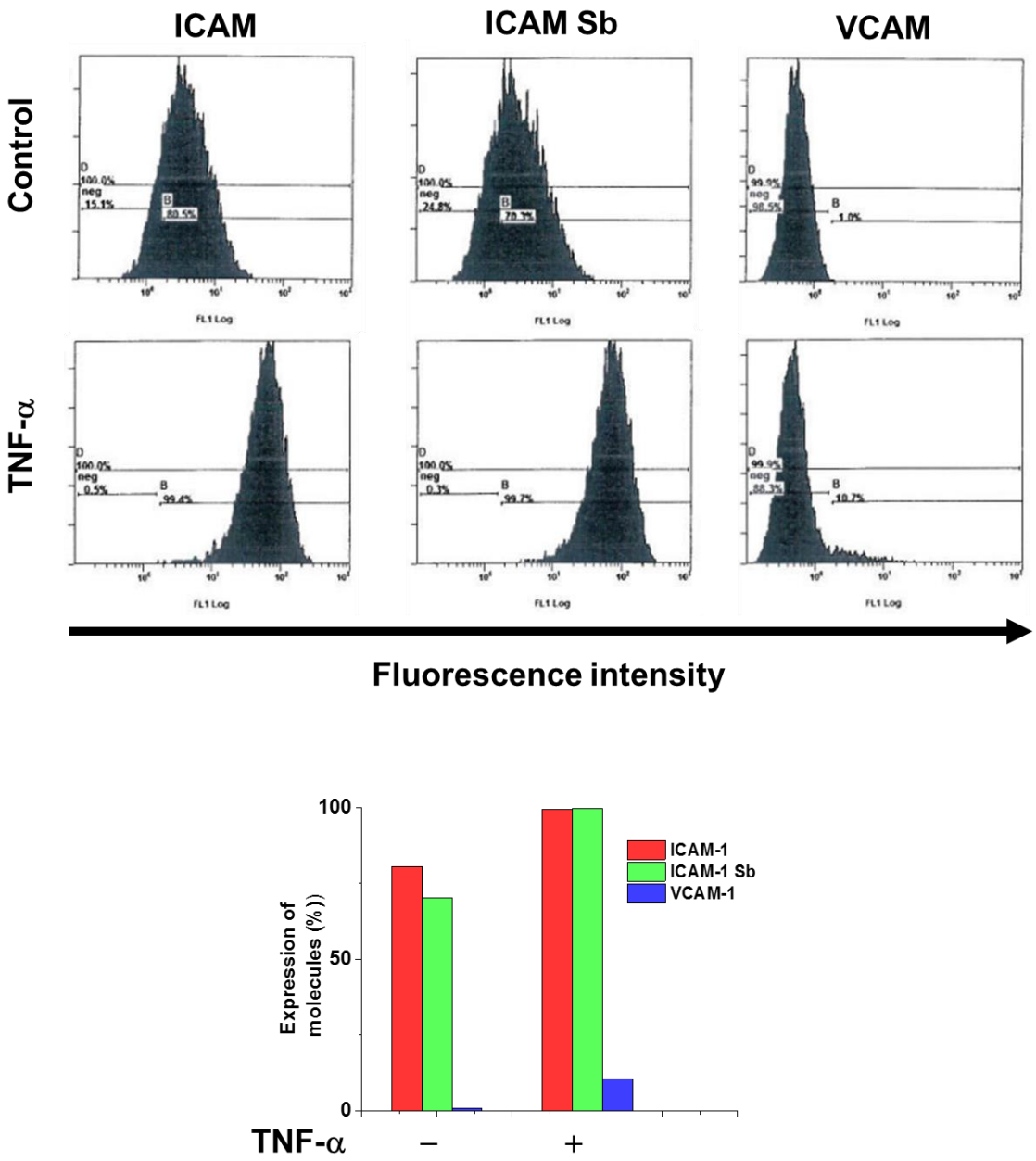


**Figure 2.9** Flow cytometer analysis of the expression of ICAM-1, ICAM-1 Sb and VCAM-1 in (and without) TNF-α-activated HMEC-1. Data in histograms are also displayed in bar graphs in the bottom of this figure.

HMEC-1 (200,000 cells/well) in six-well plates (Costar, Cambridge, MA, USA) were stimulated with 40 ng/mL TNF-α (DakoCytomation, Glostrup, Denmark) for 18 h. To evaluate the expression of ICAM-1 or VCAM-1 after exposure to TNF-α, three kinds of molecules were

used for the expression, ICAM-1 purified, ICAM-1 supernatant of hybridome (Sb) and VCAM-1, the cells were detached with a solution of 0.05% trypsin-EDTA, which was afterwards neutralized by the addition of MCDB131 complete medium. Then, the cells were washed in ice-cold PBS by centrifugation (5 min at 4°C) and resuspended in PBS containing mouse monoclonal anti-human VCAM-1/CD106 (MCA907. BIORAD) or mouse anti-human ICAM-1 monoclonal antibody (TONBO, San Diego. CA). After incubation for 1 h at 4°C, the cells were washed with ice-cold 1% BSA-PBS to remove the unbound antibody. The cell pellet was recovered by centrifugation (5 min, at 4°C) and resuspended in cold PBS containing FITC-conjugated rabbit anti-mouse Ig (1/40) (Dako, Den- mark). After washing, the cells were resuspended in PBS before being analyzed by flow cytometry with a FACScan flow cytometer (model FACS- Calibur, Becton Dickinson, San Jose, CA, USA) with the CellQuest analysis program (BD Biosciences, San Diego, CA, USA). Flow cytometry was performed using the appropriate single-stained samples for compensation setting. The number of cells expressing adhesion molecules was determined according to a forward light scatter/side light scatter gating combined with an FL-1 channel for immunostaining. The results are shown in **Figure 2.9**, before the HEMC-1 activated by TNF-α, the expression of ICAM-1 and ICAM-1 Sb are 80% and 70%, respectively. After activated by TNF-α, the expression of these two molecules have reached to 100%. In case of VCAM-1, the expression efficiency is very low, only 10% after TNF-α activated.

### 2.3.3. Cell viability study

In order to evaluate the cellular toxicity of GNSs used in the my thesis, the MTT (3-(4,5-dimethylthiazol-2-yl)-2,5-diphenyltetrazolium bromide) tetrazolium reduction assay was used in all the cases. Metabolically active cells are capable of converting MTT to formazan, which is a water-insoluble compound with dark blue color. While the dead cells lose the ability to produce formazan from MTT. When the formazan is formed in culture medium, they precipitate inside cells and being deposited inside the culture medium due to their insoluble properties in water. Here, Dimethylsulfoxide (DMSO), an organic medium, is used to stabilize the formazan and avoid evaporation.[131] Thus formazan can be quantified by from the optical absorption of the dispersion at 540 nm, and finally the number of living cells are obtained compared to the control.

In this thesis, the cell viability was studied on HeLa cells. To carried out these test, the cells were cultured in a plate with 24 wells at 37 °C in controlled atmosphere (5% of $CO_2$). After 48 hours, the culture medium was replaced by new culture medium in which NPs had previously been dispersed at different concentrations. The HeLa cells were incubated with GNSs for 24 hours. At the end of the incubation period, the culture medium with NPs was removed and medium without NPs was added to these wells. After 24 hours, 0.5 mL of an 0.05 mg/mL MTT dispersion was added to each wells and incubation was continued in controlled atmosphere for 3 hours, after that, the culture medium were discarded. The formazan crystals were dispersed in 0.5 mL of DMSO.

Finally, the optical density of the samples at 540 nm was measured using a reader of microplates (Espectra Fluor 4, Tecan). Based on it, the percentage of feasibility of cells incubated with NPs with respect to the control case was calculated by using the following expression:

$$\text{Viability (\%)} = \frac{A_{NPs}}{A_{control}} \times 100 \tag{2.16}$$

Where $A_{NPs}$ is the absorption of formazan produced by cells after incubated with NPs, and $A_{control}$ is the absorption of formazan produced by cells without incubation.

# Chapter 3. Gold nanoparticles in water dispersion visualization by OCT

## 3.1. Introduction

Although IV-OCT systems have already demonstrated to be an outstanding for both diagnosis and assistance for stent implantation, their unsurpassed sensitivity, resolution and speed suggest that they are also suitable for application in other fields such as intravascular flow studies or imaging of vessel walls at the molecular scale.[60] Nevertheless, such novel applications would require the use of optical probes capable of providing additional optical contrast at the operating OCT wavelength of 1.3 μm. At the present time few OCT contrast agents have been already developed, including gas-filled microbubbles and micrometer-sized droplets of oil with embedded silica particles on their interface.[132, 133] However, their clinical application is somehow limited due to their micrometric size. Such limitation can be easily overcome by using nano-sized OCT contrast agents, in particular by using gold nanoparticles (GNPs).

GNPs have shown to be excellent contrast agents for a variety of imaging techniques.[69, 134] In addition, they display a number of advantages for biomedical applications.[135] (i) They are inert, biocompatible [136] and can be properly functionalized with specific biological markers, allowing specific targeting and making possible the so-called "personalized diagnosis". (ii) GNPs can been easily synthesized by a variety of methods leading to different shapes (spheres, rod, cages, prisms, and stars) and sizes,[72, 77, 137] as well as combined core (dielectric)/shell (gold) spherically nanostructures, usually called gold nanoshells (GNSs). (iii) The morphology of GNPs determines the spectral position of their localized surface plasmon resonance (LSPR), which is related to the collective oscillations of free electrons confined at the dimensions of such nanometric particles. By tuning GNPs morphology, their optical response can be custom-made depending on the application.[78] Indeed, it is possible to shift the LSPR of GNPs from the visible to the BWs (700-950 nm, 1-1.3 μm, 1.5-1.8 μm), to enable *in vivo* applications. (iv) The scattering and absorption properties of GNPs can also be tuned depending on the selected NP's geometry.[138, 139] Thus, enabling the use of GNPs as photo-thermal transducers for in *in-vivo* treatments, as contrast agents for optical imaging (multiphoton excited fluorescence imaging and scattering based imaging techniques), for PA imaging and for X-Ray Computed Tomography.[46, 51, 69, 80, 140-142]

In fact, nowadays, it is possible to find out numerous examples on the use of GNPs to increase contrast in OCT images. In most of cases non-clinical OCT equipment working at wavelengths

close to 800 nm were used, so that gold nanorods (GNRs) with $\lambda_{LSPR} \approx 800$ nm were used as contrast enhancers.[143] Despite the variety of results published dealing with GNPs as contrast agents for OCT imaging, these nanoparticles have not been evaluated yet as contrast enhancers in OCT cardiovascular imaging.

In this chapter, a systematic investigation on the potential use of GNPs as contrast agents for 1.3 μm wavelength based clinical IV-OCT systems for cardiovascular imaging was conducted. The importance of the spectral overlap between the OCT laser and the GNP extinction spectra is investigated by performing experiments with GNRs and GNSs water solution displaying $\lambda_{LSPR}$ ranging from 800 up to 1300 nm. The function of IV-OCT system has been investigated by static and pull back operation after the injection of GNSs inside the tubing.

## 3.2. Characterization of GNPs

I will focus on the study of different GNPs with surface plasmon resonance wavelengths in the NIR, not far from 1.3 μm, as this is the operating wavelength of our IV-OCT system. Two types of commercial GNPs showing plasmonic extinction in this wavelength were used: GNRs and GNSs. GNRs were purchased from Nanopartz Inc., whereas GNSs were purchased from nanoComposix Inc. **Figure 3.1(a)** includes representative TEM images of the different GNPs obtained from these two companies. **Table 3.1** summarizes their main characteristics, including dimensions, nominal localized surface plasmon resonance wavelength ($\lambda_{LSPR}$), effective radius, and mass per GNP. As can be observed, up to a total of six different GNPs were studied; four GNRs with nominal LSPR wavelengths peak at 800, 1064, 1200 and 1300 nm and two GNSs with resonances peak at 856 and 986 nm. The extinction cross section spectra of the different GNPs used in the thesis are shown in **Figure 3.1(b)** for GNRs and **Figure 3.1(c)** for GNSs. The emission spectrum of the IV-OCT laser is included in both cases for the sake of comparison. The extinction cross section at the particular IV-OCT operating wavelength ($\sigma_{ext}$ ($\lambda_{OCT}$)) for each type of GNP has also been included in **Table 3.1**. From the **Figure 3.1(b)**, it is clear that GNRs show relevant extinction cross sections not only at the plasmon resonance wavelength (at which extinction cross section peaks) but over a quite broad spectral range. There is a shoulder peaking at around 500 nm for these GNRs, this is due to the transverse plasmon resonance, the other one correspond to the longitudinal plasmon resonance.[71] The spectral broadening of the extinction cross section spectra

is mainly attributed to the existence of GNRs of slightly different sizes and shapes in the water dispersion (polydispersity). As the morphology (size and aspect ratio) of GNRs determine the spectral location of their LSPR wavelength, such polydispersity leads to an inhomogeneous line broadening in the extinction spectra.[77, 144, 145] As a consequence of this spectral broadening, all GNPs present a non-vanishing extinction cross section at the OCT wavelength ($\sigma_{ext}(\lambda_{OCT})$, see detailed values in **Table 3.1**). Note that all the GNRs here investigated showed extinctions cross sections at $\lambda_{OCT}$ in the order of $10^{-12}$ cm$^2$ per nanoparticle. In the case of GNSs, as shown in **Figure 3.1 (c)**, much broader spectra are obtained in comparison to GNRs. Such broad extinction spectra are expected for GNSs due to the optical activation of surface charge oscillations of different orders.[77, 146, 147] Due to this superior broadening, although both GNSs have their LSPR below 1000 nm, they show non-vanishing extinction cross section values at $\lambda_{OCT}$, more than two orders of magnitude larger than those obtained for GNRs, being in the order of $10^{-10}$ cm$^2$ per nanoparticle for both GNSs.

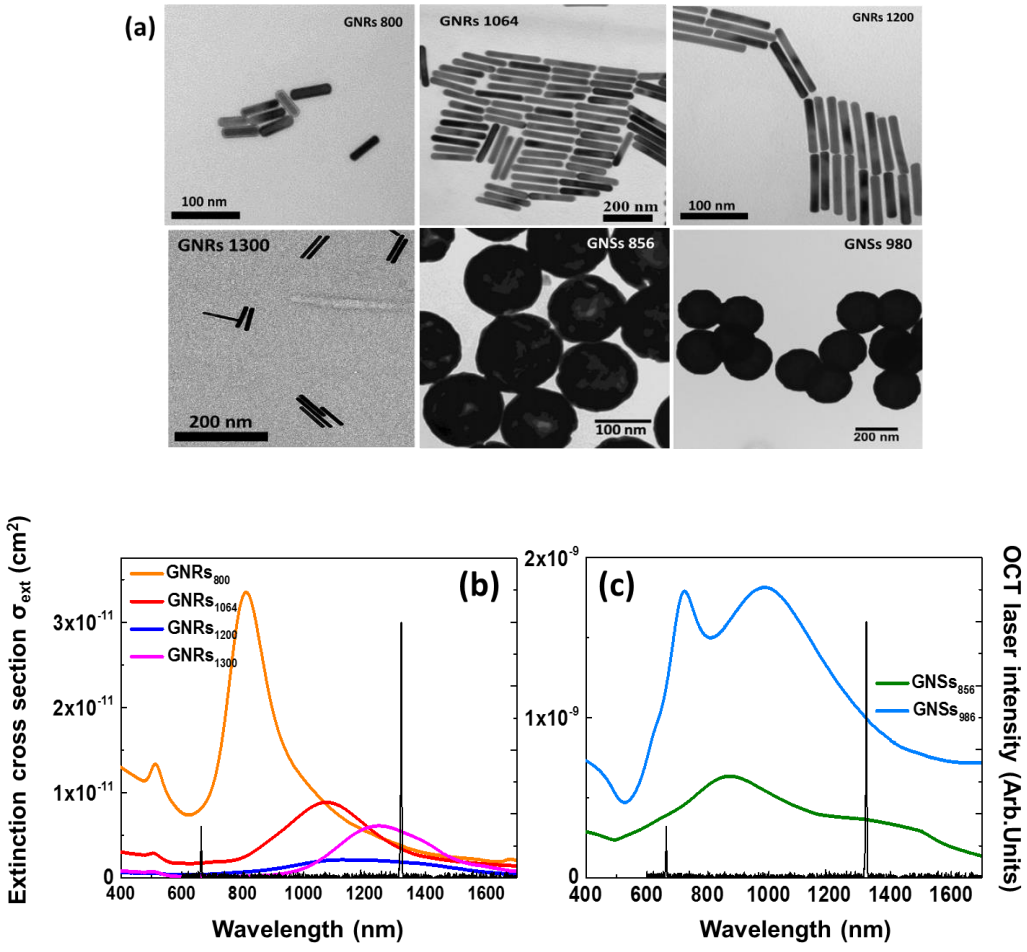

**Figure 3.1 (a)** TEM images of the different gold nanoparticles investigated in the thesis **(b)** and **(c)** show the extinction cross section spectra obtained for the GNRs and GNSs, respectively. The OCT laser spectrum is displayed in **(b)** and **(c)** as a black line.

**Table 3.1** Optical and physical properties of the different types of GNPs studied in the thesis. The OCT intensity (dB) per nanoparticle is also included.

| GNP | $\lambda_{NSPR}$ (nm) | Dimensions (nm) | $r_{eff}$ (nm) | Mass/GNP (gr/GNP) | $\sigma_{ext}@\lambda_{OCT}$ ($cm^2$) | $\Phi_{abs}$ | $\sigma_{sct}@\lambda_{OCT}$ ($cm^2$) | dB/GNP |
|---|---|---|---|---|---|---|---|---|
| GNR 800 | 800 | 25×90 | 21.9 | $7.72\times10^{-16}$ | $3.66\times10^{-12}$ | 0.66 | $1.24\times10^{-12}$ | $9.80\times10^{-11}$ |
| GNR 1064 | 1064 | 10×67 | 10.8 | $9.80\times10^{-17}$ | $3.24\times10^{-12}$ | 0.96 | $0.12\times10^{-12}$ | $1.71\times10^{-11}$ |
| GNR 1200 | 1200 | 21×171 | 24.2 | $7.84\times10^{-17}$ | $1.83\times10^{-12}$ | 0.76 | $0.44\times10^{-12}$ | $2.30\times10^{-11}$ |
| GNR 1300 | 1300 | 10×100 | 12.3 | $1.47\times10^{-16}$ | $5.31\times10^{-12}$ | 0.96 | $0.20\times10^{-12}$ | $3.00\times10^{-11}$ |
| GNS 856 | 856 | 15.5×117.8 | 74.1 | $1.67\times10^{-14}$ | $3.61\times10^{-10}$ | 0.34 | $2.40\times10^{-10}$ | $3.96\times10^{-9}$ |
| GNS 986 | 986 | 16.4×198.1 | 115.5 | $6.80\times10^{-14}$ | $7.63\times10^{-10}$ | 0.37 | $4.84\times10^{-10}$ | $1.15\times10^{-8}$ |

Previous works pointed out the relevant role played by the scattering cross section (an in particular by the backscattering cross section) of nanoparticles in their OCT enhancement capability;[148, 149] the higher value of backscattering coefficient the higher OCT intensity gain. Thus, in order to make a proper interpretation of OCT images, the scattering cross section at $\lambda_{OCT}$ ($\sigma_{sct}(\lambda_{OCT})$) for each type of GNP has been estimated. These cross section values have been determined from the experimental value of the extinction cross section and the particular absorption efficiency of each type of GNP. The absorption efficiency of any GNP is defined as the ratio between the absorption and extinction cross section, i.e. $\phi_{abs} = \frac{\sigma_{abs}(\lambda_{OCT})}{\sigma_{ext}(\lambda_{OCT})}$.[51, 150] This efficiency can be estimated by using the discrete dipole approximation method and, in particular, the open-source Fortran-90 software package Discrete Dipole Scattering (DDSCAT) 7.3.[76] Once $\phi_{abs}$ is known, the scattering cross section can be estimated from the extinction cross section by taking into account that $\sigma_{ext} = \sigma_{abs} + \sigma_{sct}$. Thus, we can write:

$$\sigma_{sct}(\lambda_{OCT}) = (1 - \phi_{abs})\sigma_{ext}(\lambda_{OCT}) \quad (3.1)$$

**Table 3.1** includes both the absorption efficiencies and the estimated scattering cross sections at OCT operating wavelength for all the GNPs under study. It is clear that GNSs display the largest values of $\sigma_{sct}(\lambda_{OCT})$ among all the studied GNPs, this fact is due to their larger extinction cross section values (when compared to GNRs) as well as to their reduced absorption efficiencies (i.e. to their large scattering efficiencies).

Previous works clearly stated that the OCT contrast enhancement provided by nanoparticles basically depends on the relative change in the backscattering coefficient between the nanoparticle and the medium.[143, 151] For instance, in highly scattering media, nanoparticles with low scattering cross sections have demonstrated to lead to a maximum OCT contrast.[143] In this case, a weakly scattering medium was used, and so, the achievement of high OCT contrast would require the use of nanoparticles with high scattering cross section and, in particular, with high back-scattering cross section, $\sigma_{bsct}$.[21] In this respect, the DDSCAT code allows also for estimating $\sigma_{bsct}$ for any GNPs. The estimated values using this code are also listed in **Table 3.1**. GNSs are expected to be those providing the largest OCT contrast over all the GNPs here considered. In order to corroborate this prediction, the OCT contrast generated per individual GNP was systematically investigated for all the GNPs isotonic saline solution.

### 3.3. Static OCT imaging experiments

The experimental procedure followed all along the chapter for the visualization of GNPs is schematically represented in **Figure 3.2.** Basically, the IV-OCT catheter is introduced in a plastic tubing of 3 and 3.6 mm of internal and external diameter, respectively. GNPs were then injected in the proximity of the OCT catheter by using a subcutaneous needle **(Figure 3.2 (a))**. A volume of 5 μL of a solution of GNPs in isotonic saline solution was injected. Solutions containing different concentrations of GNPs were used. After the injection, three different types of experiments for GNP visualization were performed, schematically drawn in **Figure 3.2 (b-d)**. A representative IV-OCT slice provided by IV-OCT system was also included in **Figure 3.2 (e)**. It shows two cross-sectional images, one is the cross-sectional image of the tubing filled with GNPs, the other one is the axial cross-sectional image obtained from the line crossed the tubing and catheter. More information, such as the IV-OCT scan time, the date of the experiment, the morphology of the tubing and the table where the tubing was put can be obtained from this image.

Particularly, I will focus on the OCT cross-sectional image contained in the dotted line circle, which contains a cross-sectional image of GNPs obtained by IV-OCT system.

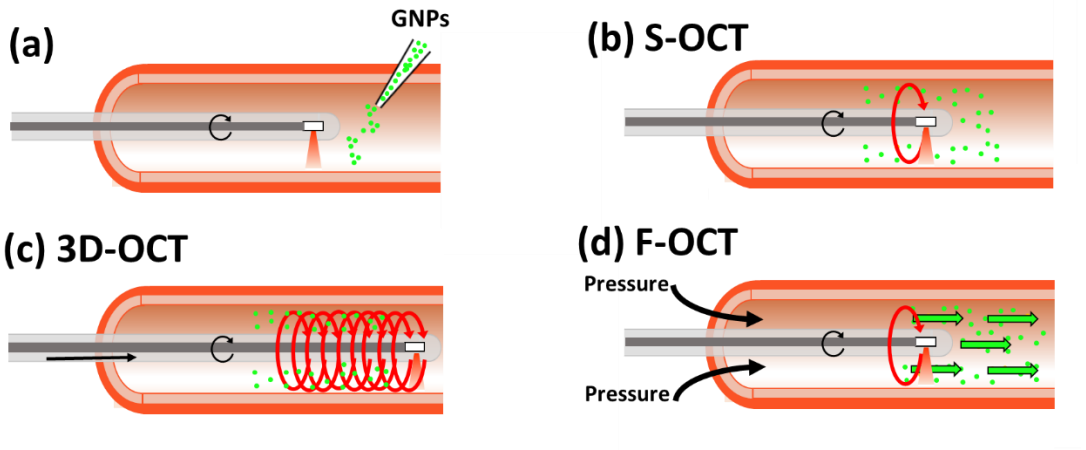


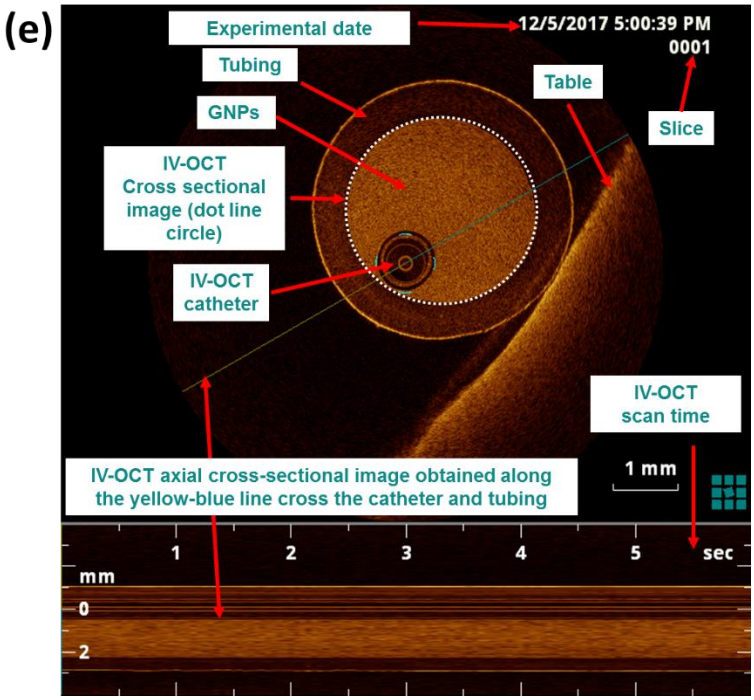


**Figure 3.2 (a)** The procedure here used for the injection of GNPs into the IV-OCT system. **(b)** The arrangement for "static measurements", in which OCT images are obtained with both the GNPs solution and catheter under static conditions. **(c)** The procedure followed for the acquisition of three dimensional OCT images; The OCT catheter is moved while keeping the GNPs solution remains under static conditions. **(d)** The procedure for the acquisition of OCT images of flowing GNPs; the OCT catheter is kept at fixed

position while the solution containing GNPs is pushed forward. **(e)** A representative IV-OCT slice obtained from S-OCT video.

*Static OCT imaging experiments (S-OCT)*: In order to evaluate the contrast enhancement produced by the GNPs, static images where obtained, in which the IV-OCT catheter remains in the same axial position while performing cross sectional imaging of the tubing in absence of any flow , i.e. under static condition (see **Figure 3.2 (b)**). The detection limit of the IV-OCT system for each type of GNPs was systematically investigated by injecting solutions with different GNPs concentrations (ranging from $5\times10^{-2}$ down to $5\times10^{-6}$ mg/mL).

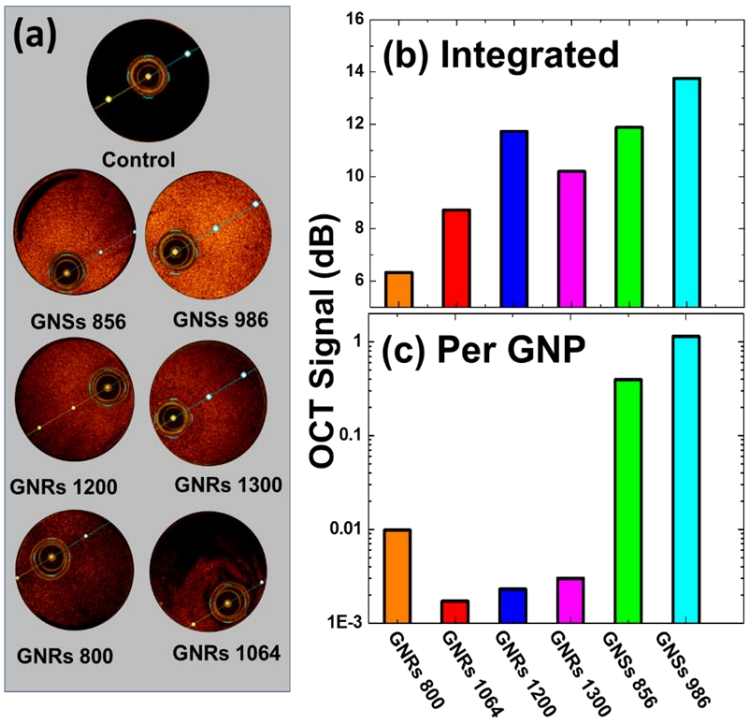


**Figure 3.3 (a)** S-OCT images of the conduit when it was filled with a saline solution (Control) and with solutions containing different GNPs. In all the cases the GNP concentration was set to 0.05 mg/mL of GNPs. **(b)** Integrated OCT signal as obtained for the different GNPs. **(c)** OCT signal normalized per the density of GNPs as obtained for the GNPs investigated in the thesis. Note that OCT images are taken by a clinical OCT system and so including some measuring tools (lines, reference points) that are used by clinicians that cannot be removed from the images

After injection of different GNPs solutions, the static OCT videos were recorded. The static OCT (S-OCT) cross-sectional images, which were obtained from the S-OCT videos, are shown in **Figure 3.3 (a)**. For the sake of comparison, the S-OCT image obtained when the tubing was filled with only saline solution (control) is also included. From the S-OCT images included in **Figure 3.3 (a)**, it is clear that, for all cases, the presence of GNPs in the tubing leads to a relevant enhancement in the OCT contrast, but the amount of induced enhancement is found to be strongly dependent on the particular type of GNP used. At this point, it should be mentioned that to estimate the OCT enhancement, OCT intensities were first calculated, for each case, by defining a measuring area inside the tubing in which the OCT signal was uniform. Then, using the ImageJ software, I integrated the signal inside this area. The same procedure (same area and same integration procedure) was applied for all the images. Thus, from these analyses, the OCT contrast enhancement (as measured in dB, $\mathrm{dB} = 10 \times \log(I_{OCT}/I_{background})$) for each particular GNP can be obtained. **Figure 3.3 (b)** shows the OCT signal enhancement as obtained from the S-OCT images included in **Figure 3.3 (a)**. It is clear that for the same mass concentration in the GNPs/ solution (0.05 mg/mL) GNSs present the largest OCT contrast. This is further evidenced in **Figure 3.3 (c)** that shows the OCT signal enhancement normalized to the GNPs concentration for each case; the data are included in **Table 3.1**. **Figure 3.4** shows the OCT enhancement signal per GNP as a function of the back-scattering cross section at the OCT wavelength (given by each particular GNP). As expected, the OCT signal enhancement monotonously increases with the back-scattering cross section given by each type of GNPs. A linear fir to the data given in **Figure 3.4**, lead to an almost linear dependence: $\mathrm{d}B \sim \sigma_{bsct}^{0.8}$. Thus, from **Figure 3.4** and the data given in **Table 3.1,** it is clear that, generally speaking, GNSs present scattering cross sections (at OCT wavelength) two orders of magnitude larger than GNRs. Such difference accounts for the different OCT signal enhancement generated by GNSs and GNRs. In particular the dominant role of back-scattering processes in the enhancement of OCT contrast induced by GNPs is clearly manifested.

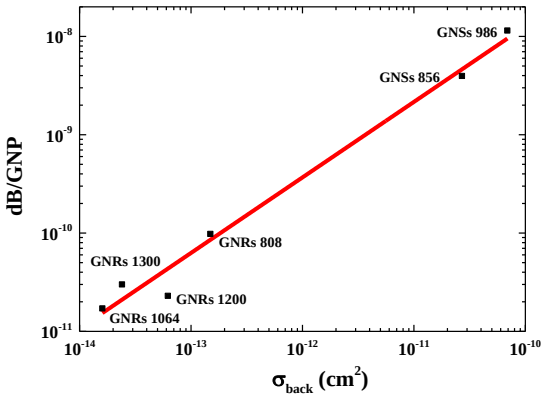


**Figure 3.4** OCT signal enhancement per GNP as a function of backscattering cross section. The solid line indicates the best linear fit to the data.

Once GNSs have been identified as the optimum GNPs ones for enhanced OCT contrast, I proceed to evaluate the potential ability of IV-OCT detection and imaging of individual GNSs under both static and dynamic conditions. As a first step, and in order to determine the detection limit of our clinical OCT apparatus, I conducted systematic OCT imaging experiments using saline solutions with different concentrations of GNSs 986 (the best scatterers). The results are summarized in **Figure 3.5**. **Figure 3.5 (a)** shows the S-OCT images obtained for three representative GNSs concentrations. On one hand, for elevate GNSs concentrations (0.05 mg/mL, leading to a GNSs density of $1.2\times10^9$ GNSs/cm$^3$) the S-OCT image is characterized by a homogeneous and high contrast signal all along the cross section of the tubing. As one GNSs occupying a volume of 833.33 μm$^3$ ($1\times10^{12}$ μm$^3$/$1.2\times10^9$ GNSs), in this case, the movement of single GNSs were thought to be in this volume, the shape of this volume is thought to be a cubic, thus the size of the cubic is 833.33 μm$^3$, the length of its side is 9.4 μm. The average separation between GNSs was estimated to be around 9.4 μm for this concentration, which is below the axial resolution of our OCT system (15 μm, according to the manufacturer). Therefore, for such large concentrations, the detection of isolated/individual GNS is not possible, and the image appears as a pseudo-homogeneous high-contrast medium. On the other hand, when the GNSs concentration is reduced by several orders of magnitude, the OCT image appears as constituted by different bright spikes corresponding to the local OCT enhancement caused by individual GNSs (see the zoom of the OCT image obtained from the solution containing GNSs 986 at a concentration of $5\times10^{-5}$ mg/mL). Such low concentration corresponds to a GNS density of $1.2\times10^6$ GNSs/cm$^3$ that

leads to an average distance between GNSs close to 94 µm (One GNSs will occupy $8.33\times10^5$ µm$^3$, and has a length of 94 µm). Indeed, this interparticle distance is more than six times the nominal axial resolution of our OCT system. Thus, under these conditions, the visualization of individual GNSs becomes possible as it is experimentally demonstrated in the OCT images of well diluted solutions included in **Figure 3.5 (a)**. These results reveal the ability of nanosized individual particles as local contrast agents for OCT and supports conclusions of previous works that pointed out the potential capacity of OCT for imaging at the nanoscale.[152-154]

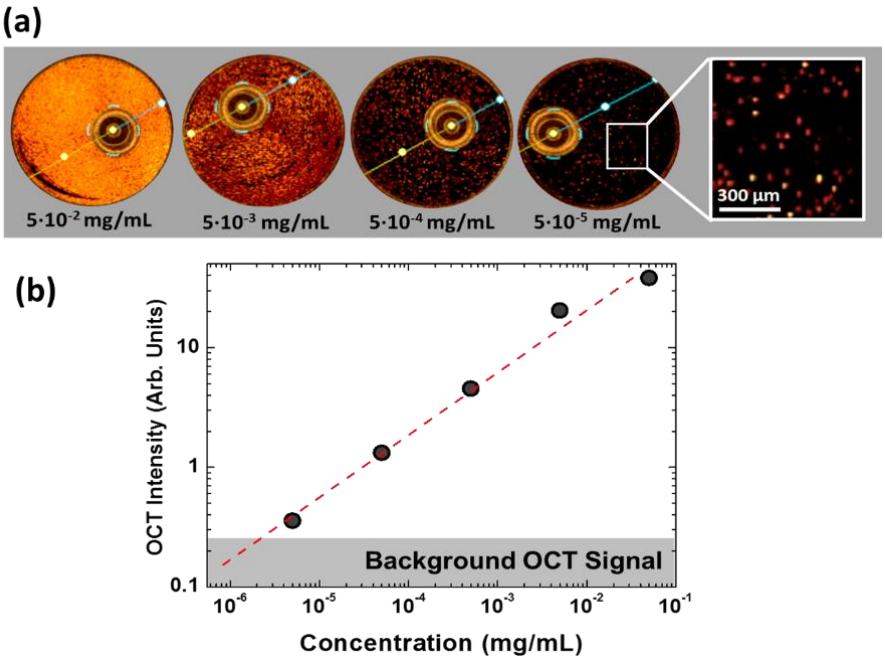


**Figure 3.5. (a)** S-OCT images of the conduit when it was filled with saline solutions containing GNSs at different concentration levels. A detailed zoom of the S-OCT image of the $5\times10^{-5}$ mg/mL concentrated solution is also included. **(b)** OCT integrated intensity as a function of the concentration of GNSs. Dots are experimental data obtained from S-OCT images and dashed line is a guide for the eyes. The background OCT signal is indicated by the gray area. Detection limit is estimated to be $3\times10^{-6}$ mg/mL. Note that OCT images are taken by a clinical OCT system and so including some measuring tools (lines, reference points) that are used by clinicians that cannot be removed from the images.

The dependence of the OCT intensity as a function of GNS concentration is displayed in **Figure 3.5 (b)**, which constitutes a basis to estimate the detection limit of our OCT system for GNP detection. The background level in our experimental conditions is also indicated by the grey area.

From **Figure 3.5 (b)** it is clear that our clinical OCT system is able to detect the presence of colloidal GNSs with a detection limit close to $5\times10^{-6}$ mg/mL that corresponds to a GNSs density close to $1.2\times10^{5}$ GNS/cm$^3$. This constitutes a relevant improvement in respect to the detection limits previously reported for OCT imaging of GNRs and GNSs that were established to be close to $1\times10^{11}$ GNRs/cm$^3$ and $6.2\times10^{9}$ GNSs/cm$^3$.[143, 151] In other words, it is here demonstrated the superior performance of clinical OCT scans for intravascular detection of single GNPs. At this point, such improvement is due to the special sensitivity of our experimental OCT system together with the use of highly scattering GNSs.

### 3.4. Three dimensional imaging of GNPs

*Three dimensional imaging of GNPs (3D-OCT):* The potential application of the clinical OCT for real three dimensional localization of GNPs was demonstrated by using the pull-back imaging option of the clinical OCT system. In this case the fluid inside the tubing was set to be under static conditions (no pressure applied at the end of the tubing). Then a sequence of OCT images were recorded during pull-back of the OCT catheter over a 5 cm path length, i.e. cross-sectional images of the tubing were measured at different axial positions within the tubing as it is schematically indicated in **Figure 3.2 (c)**. Subsequent analysis of the image sequence was performed by ImageJ software, allowing for a three dimensional reconstruction of the GNP distribution along the tubing. The obtained images were then used to estimate the density of GNPs (number of particles per unit volume)

In other to unequivocally assign the bright spots appearing in the OCT images of low concentrated solutions to the presence of individual GNSs, a 3D-OCT experiment was performed along a tubing partially filled with a water solution containing, nominally, $3\times10^{7}$ GNSs/mL. As schematically indicated in **Figure 3.2 (c),** for these particular measurements the OCT catheter was initially positioned inside the GNSs injected volume and it was then scanned along the tubing for a total distance of 5 mm, so that at the end of the scan the catheter reaches a tubing volume without GNSs (i.e. just filled with saline solution). The 3D-OCT image of the GNSs was obtained by importing the *x*, *y* and *z* coordinates of GNSs in the IV-OCT videos into Origin software and drawing 3D scatter. Thus 3D-OCT image is shown in **Figure 3.6 (a)**. Note that the interface between the volume containing the GNSs and the volume filled with just the solution is found to

be close to $Z$ = 1 mm. From the analysis of this 3D-OCT image I have computed a total number of GNSs close to $4.2\times10^4$. The volume containing those GNPs is estimated to be $8.6\times10^{-3}$ mL, leading to a GNSs concentration of $0.5\times10^7$ GNSs/cm$^3$. This is of the same order of magnitude, but six times lower, than the nominal concentration of the injected solution ($3\times10^7$ GNSs/cm$^3$). The relative good agreement between measured and nominal GNP concentration results reasonable, specially taking into account that when measuring the 3D-OCT images the catheter is moving along the axial ($Z$) direction while scanning radially the *xy* plane so that it is doing a spiral-shape 3D scan that would result in a slight underestimation of the actual GNSs concentration. **Figure 3.6 (b)** shows a detailed zoom of the 3D-OCT image in the surroundings of the water-GNSs solution interface. From this figure, it is evidenced the nonhomogeneous distribution of GNSs along this interface. From **Figure 3.6 (b)** (in which the *z* scale has been enlarged) it is also possible to localize well-isolated GNSs behind the interface, i.e. in the pure aqueous volume (see red arrows). Data included in **Figure 3.6** demonstrate the potentiality of clinical OCT cardiovascular systems for the 3D localization of single GNPs.

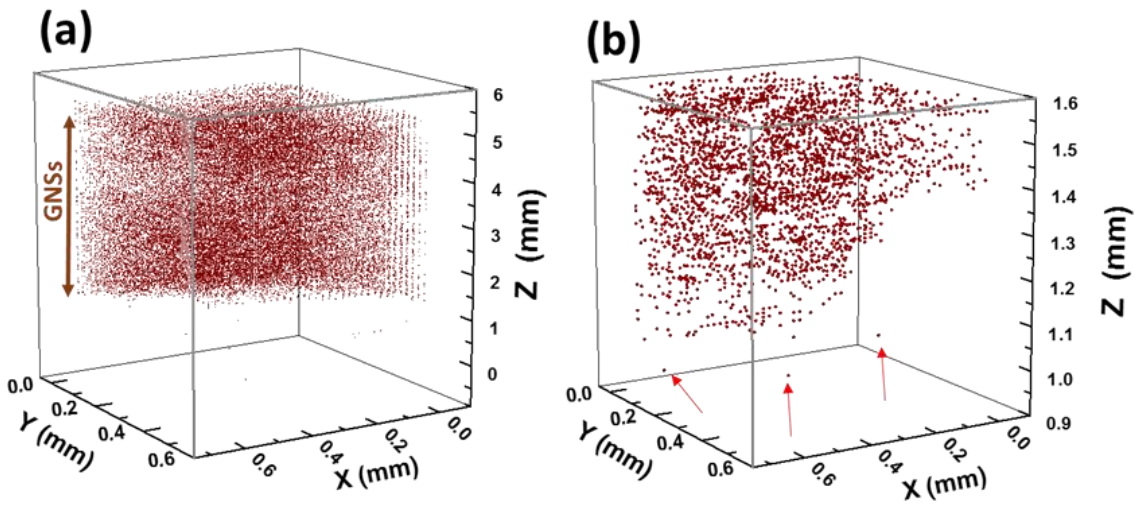


**Figure 3.6 (a)** 3D-OCT image of the conduit partially filled with an injection of a saline solution containing GNSs 856 at a concentration of $5\times10^{-4}$ mg/mL. Each pixel providing a OCT signal larger than background level has been identified as a single GNS, indicated by a dot. **(b)** Detailed 3D-OCT image of the interface between the GNS solution and water. The presence of individual and isolated GNSs in the non-injected volume of the tubing are evidenced by red arrows.

## 3.5. OCT imaging of flowing GNPs

*OCT imaging of flowing GNPs (F-OCT)*: In order to demonstrate the potential ability of the IV-OCT system under dynamical conditions, a pressure syringe filled with the isotonic saline solution was connected to the end of the tubing, containing both the OCT catheter and the injected solution of GNPs. This syringe allowed us to apply, in a controlled way, a given pressure in one end of the tubing and, hence, an intra-tubing flow, as it is schematically indicated in **Figure 3.2 (d)**. As a consequence of this flow, the solution containing the GNPs was pushed from one extreme to the other extreme of the tubing. In these experiments, the OCT catheter remained in a fixed position. A 5 s video was recorded during the flushing out procedure of the GNPs. Analysis of this video by ImageJ software allowed us to plot the time evolution of the GNPs distribution at the position of the OCT catheter.

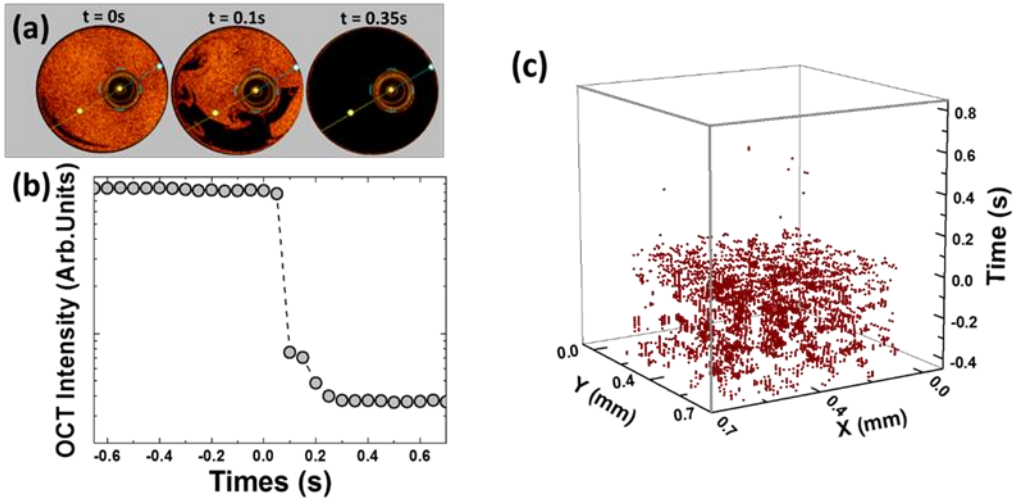


**Figure 3.7 (a)** F-OCT images of the conduit when it was filled with saline solution containing GNSs 986 at a concentration of 0.05 mg/mL as obtained at different times. **(b)** OCT integrated intensity as a function of time during the F-OCT procedure. Dots are experimental data obtained from S-OCT images and dashed line is a guide for the eyes. **(c)** Time evolution of the cross sectional OCT image during the F-OCT procedure as obtained with a GNSs 986 concentration of $5\times10^{-6}$ mg/mL.

**Figure 3.7 (a)** shows three representative F-OCT images corresponding to a 0.05 mg/mL concentrated water solution of GNSs 986, as obtained at different times after establishment of an intra-tubing evacuating flow. In this figure $t = 0$ *s*, the interface between the water and GNSs water

solution start crossing the OCT cross sectional detection plane. Before $t = 0$ *s*, the F-OCT image showed a homogeneous bright signal, indicating the presence of homogeneously distributed flowing GNSs inside the tubing. Just after $t = 0$ ($t = 0.1$ *s*) the F-OCT signal becomes highly inhomogeneous, indicating that, at the position of OCT catheter, the GNSs are no longer homogeneously distributed. Indeed, this reveals that the solution containing the GNRs at the interface is mixing with water in a non-homogeneous way, as it was already evidenced in **Figure 3.6 (c)**. For times larger than 0.2 s, the F-OCT contrast signal has been completely removed, as can be observed in **Figure 3.7 (b)**. The complete suppression of OCT contrast signal unequivocally indicates that the solution containing the GNSs has been fully replaced by pure water and, thus, all GNSs have been pushed out from the cross sectional OCT detection section. Appropriate analysis of the F-OCT images obtained under flowing conditions allowed us to plot the position of single GNSs in a certain cross-sectional area as function of time. A representative of plot is included in **Figure 3.7 (c).** It can be observed how GNSs have been removed after 0.2 s pushing from the studied cross-sectional image. Thus constitutes a solid proof of the potential ability of intravascular OCT systems for detecting single GNPs under non-static conditions. This ability could be very useful for a great variety of applications, including the localization and evaluation of intravascular obstructions via detection of flowing GNPs, the accurate measurement of blood velocity and, even, the indirect determination of intravascular pressure gradients.

## 3.6. Conclusions

In summary, I have experimentally demonstrated how gold nanoshells showing multipolar plasmonic excitations in the 1000-1500 nm spectral range are excellent contrast agents for frequency based intravascular OCT catheters, working at 1320 nm. This ability is mostly based in the large scattering (backscattering) cross section values that these nanoparticles provide at this specific wavelength, which are two orders of magnitude larger than those given by the gold nano-rods traditionally used as OCT enhancers. The outstanding OCT contrast provided by gold nanoshells has allowed for detecting individual nanoparticles under both static and dynamical conditions. I firmly believe that the results here presented open a new avenue for novel potential applications of intravascular optical coherence tomography.

On the other hand, it is important to stand out the high sensitivity of IV-OCT system. It can be used for visualizing individual NPs both in static and dynamical conditions. This has open an avenue of possibilities for future work.

# Chapter 4. Experimental evaluated scattering properties of gold nanoparticles

## 4.1. Introduction

After the selection of GNPs, the first step for the functional validation of these GNPs as contrast agents for IV-OCT is a full understanding of their infrared optical properties including the wavelength dependence of their absorption and scattering efficiencies. Such knowledge is imperative for of IV-OCT images analysis, as well as to evaluate the thermal loading during intravascular image acquisition. Until now there are only few experimental studies dealing with the scattering/absorption efficiency of GNPs in the BWs. Remind that the efficiency that were previously determined in **Chapter 3** was based on the spectral simulation. Indeed, most of the studies describing optical properties of GNPs are dealing with their response in the visible domain or in the I-BW.[155-157] The geometry dependence of the GNPs scattering efficiency has been experimentally determined at 808 nm,[158] as this one is the working wavelength OCT systems for ophthalmology.[159, 160] There are numerous predictive models on the optical response of different GNPs in the II-BW. However, an experimental validation of the wavelength dependence of both scattering and absorption efficiencies of GNPs in the BWs has not been demonstrated yet. Providing this experimental data is crucial for the functional validation of GNPs as contrast agents for advanced IV-OCT.

In this chapter, the scattering efficiency of three types of GNPs (gold nanorods, gold nanoshells and gold nanostars) displaying LSPR with significant extinction at around 1.3 µm (the operating wavelength of clinical IV-OCT apparatus) have been experimentally determined. By means of a well-stablished photo-thermal method,[126, 157, 161] the scattering efficiency has been measured at three different wavelength, namely at 808 nm, 980 nm and 1280 nm. These multi-wavelength experimental data have been compared with numerical simulations performed in **Chapter 3**, we will see that simulation failed to reproduce reliable values at long wavelengths. This fact stands out the importance of an experimental determination of the scattering and absorption efficiencies. The geometry dependence of scattering efficiency determined by the photo-thermal method has been corroborated by the combination of IV-OCT, infrared dark field microscopy (IR-DFM) and infrared optoacoustic (IR-OA) spectroscopy. The optimum GNPs geometry for IV-OCT contrast enhancement has been determined and the importance of the experimental determination of the spectral dependence of infrared scattering efficiency has been clearly evidenced.

## 4.2. Characterization of the GNPs

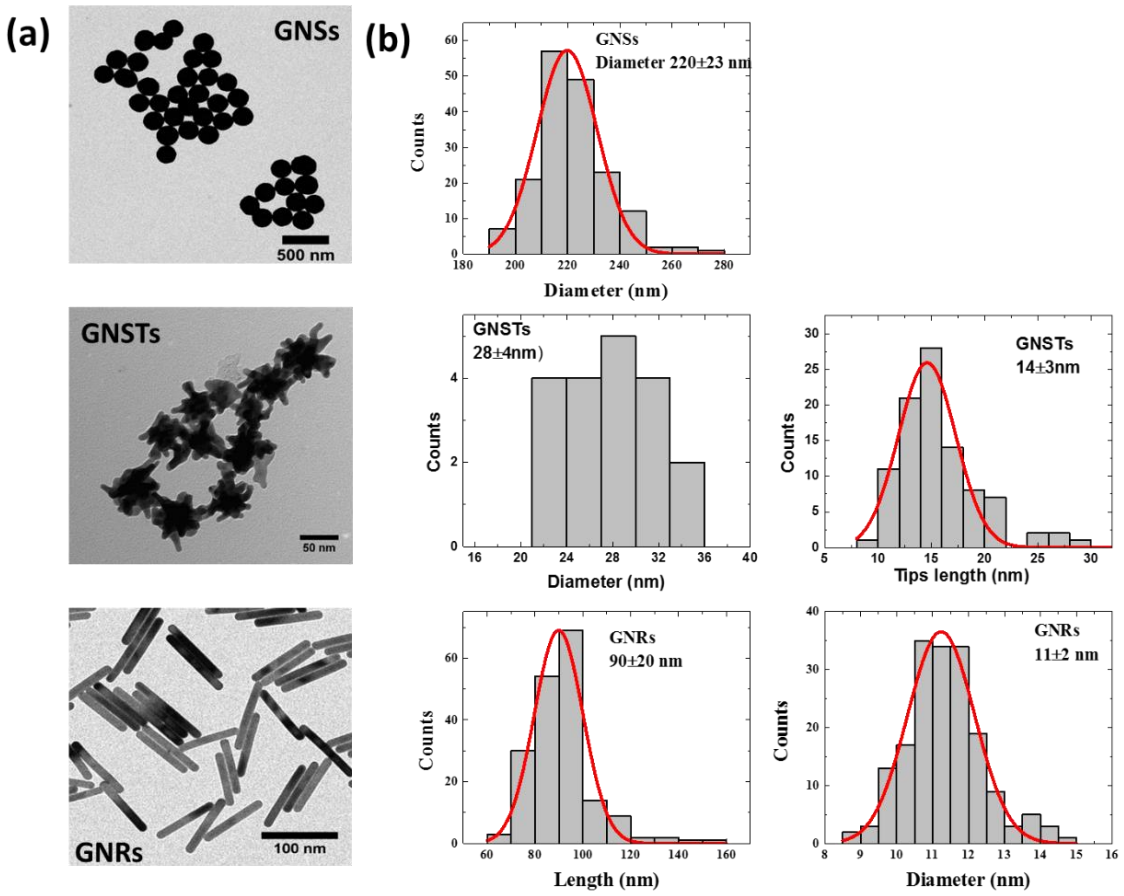


**Figure 4.1 (a)** TEM images of the GNSs, GNSTs and GNRs used along this chapter. **(b)** Size distribution of GNSs, GNSTs and GNRs

Three kind of the GNPs with different shape were used in this chapter; GNRs, GNSs and gold nanostars (GNSTs). GNRs and GNSs were the same describe before, whereas GNSTs were synthesized at Pompeu Fabra University (UPF). **Figure 4.1** shows the representative TEM images and size distribution of these GNPs. Here, the TEM of the GNRs and GNSs are shown again due to the new batches of GNRs and GNSs were used here (their TEM images were previously shown in **Chapter 3**). GNRs have a diameter of 11±2 nm and a length of 90±20 nm. GNSs have a total average diameter of 220±23 nm. GNSTs consist in solid gold nanospheres with an average diameter of 28±4 nm together with different lobes (in average 14) with an average length of 14±3 nm.

The extinction cross section spectra of these three structures are included in **Figure 4.2**. The extinction cross section spectra shape of GNRs and GNSs are the same as they were described in **Chapter 3**. The extinction cross section of GNSTs is constituted by a plasmonic band peaking at about 800 nm and extends in the IR spectral region from about 500 nm to 1600 nm. Such LSPRs are electric dipole resonances stemming from the collective oscillations of Au electrons. As such, they are sensitive to nanoparticle shape (except for very small nanoparticle), especially along the direction of electric field polarization of the incident light. GNSTs are not spherically symmetric; however, for a sufficiently large number of star tips pointing to all directions, they are nearly polarization independent.[162,121, 163] Due to broad extinction spectra of these GNPs, the relevant infrared wavelengths were investigated in this chapter; 808 nm, 980 nm and 1280 nm (the IV-OCT working wavelength).

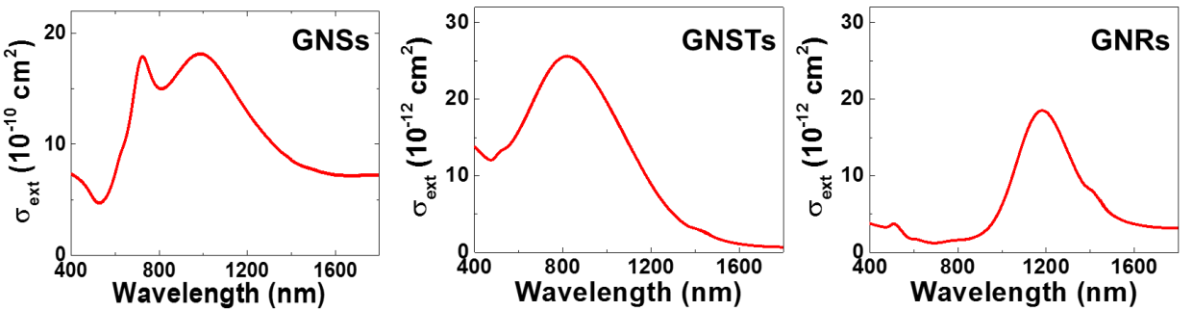


**Figure 4.2** Extinction spectra obtained from colloidal suspensions of GNSs, GNSTs and GNRs.

## 4.3. Experimental determination of infrared scattering efficiency

The experimental determination of the wavelength dependence of the scattering efficiency ($\eta_s$) is based on the experimental determination of the photo-thermal heating conversion efficiency ($\eta_h$) at each particular wavelength (808, 980, 1280 nm). $\eta_h$ is defined as the fraction of extinct (scattered or absorbed) energy by a single nanoparticle that is converted into heat. For non-luminescent nanoparticles, as it is our case, all the absorbed energy by a single nanoparticle is converted into heat, so that the photo-thermal conversion efficiency is equal to the absorption efficiency ($\eta_a$) (i.e. $\eta_h = \eta_a$), as defined in **Chapter 3**. At a given wavelength ($\lambda$), it can be written:

$$\eta_h(\lambda) = \eta_a(\lambda) = \frac{\sigma_{abs}(\lambda)}{\sigma_{abs}(\lambda) + \sigma_{sct}(\lambda)} = \frac{\sigma_{abs}(\lambda)}{\sigma_{ext}(\lambda)}, \quad (4.1)$$

where $\sigma_{abs}(\lambda)$, $\sigma_{sct}(\lambda)$ and $\sigma_{ext}(\lambda)$ are the absorption, scattering and extinction cross sections at a wavelength $\lambda$, respectively. If the photo-thermal conversion efficiency $\eta_h$ is known, then the scattering efficiency, as described in **Chapter 3**, can be written:

$$\eta_s(\lambda) = 1 - \eta_a(\lambda) = 1 - \eta_h(\lambda). \quad (4.2)$$

The photo-thermal conversion efficiency can be evaluated by measuring the input/output heat balance under transient illumination, as previously reported.[126, 157, 164] **Figure 2.3 (a)** shows the experimental arrangement used all along this work to measure $\eta_h(\lambda)$. The method is described in detail in **Chapter 2 Experimental techniques**. It is based on the measurement of the heating and cooling curve of a solution containing the GNPs when it is optically excited by a fiber coupled laser diode. A representative heating/cooling curve is shown in **Figure 2.3 (b)**. From this curve, it is possible to estimate the absorption efficiency, which it is given by:

$$\eta_a = 1 - \eta_s = \frac{\frac{mC_p\Delta T_{max}}{\tau} - Q_r}{P_0(1 - 10^{-OD})}, \quad (4.3)$$

where $m$, $C_p$ and $OD$ are the mass, specific heat and optical density of the solution containing the GNPs. $P_0$ is the incident laser power, $\Delta T_{max}$ is the maximum temperature increment (indicated in **Figure 2.3 (b)**) and $\tau$ is the relaxation time of the cooling process (also indicated in **Figure 2.3 (b)**). Equation (4.3) gives the photo-thermal efficiency (equal to the absorption efficiency) from parameters that are either known or can be experimentally measured. For instance, the specific data shown **Figure 2.3 (b)** corresponds to the heating and cooling cycle of an aqueous solution of GNRs excited at 1280 nm and for the particular values $m$ = 0.5 g, $P_0$ = 160 mW, $OD$ = 1.075, $\Delta T_{max}$ = 9.92 $^oC$ and $\tau$ = 104.3 s. Substituting these values in Equation (4.3), an absorption efficiency of 0.95 was obtained, and therefore, a scattering efficiency of $\eta_s$: 1-0.95 = 0.05.

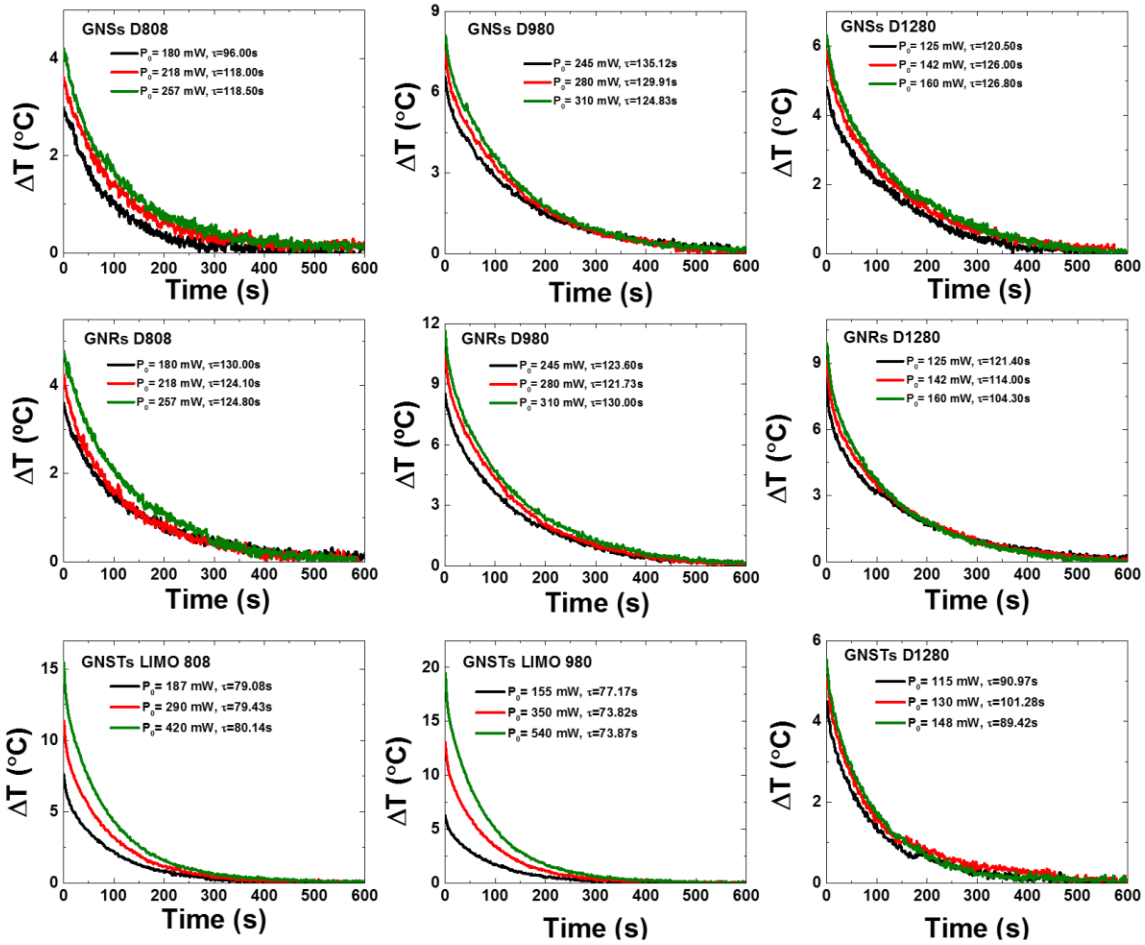


**Figure 4.3** Cooling curves of the GNPs under excitation at different wavelength.

**Table 4.1** Parameters to calculate absorption efficiency

| Laser wavelength (nm) | $P_0$ (mW) | $Q_r$ (mW) | $\tau_s$ GNSs | OD GNSs | ΔT(°C) GNSs | $\eta_\alpha$(±10%) GNSs | Average $\eta_\alpha$ | Simulated $\eta_\alpha$ GNSs |
|---|---|---|---|---|---|---|---|---|
| | 125 | 45 | 120.5 | | 4.81 | 51 | | |
| 1280 | 142 | 52 | 126.0 | 0.406 | 5.85 | 52 | 49 | 32 |
| | 160 | 60 | 126.8 | | 6.31 | 45 | | |
| | 245 | 70 | 135.12 | | 6.55 | 16 | | |
| 980 | 280 | 80 | 129.91 | 0.67 | 7.41 | 18 | 16 | 22 |
| | 310 | 100 | 124.83 | | 8.12 | 15 | | |
| | 180 | 16 | 96.00 | | 2.97 | 38 | | |
| 808 | 218 | 18 | 118.00 | 0.55 | 3.61 | 29 | 32 | 28 |
| | 257 | 22 | 118.50 | | 4.21 | 28 | | |

| Laser wavelength (nm) | $P_0$ (mW) | $Q_r$ (mW) | $\tau_s$ GNRs | OD GNRs | ΔT(°C) GNRs | $\eta_\alpha$(±10%) GNRs | Average $\eta_\alpha$ | Simulated $\eta_\alpha$ GNRs |
|---|---|---|---|---|---|---|---|---|
| | 125 | 45 | 121.40 | | 8.07 | 82 | | |
| 1280 | 142 | 52 | 114.00 | 1.075 | 9.11 | 88 | 88 | 95 |
| | 160 | 60 | 104.30 | | 9.92 | 95 | | |
| | 245 | 70 | 123.60 | | 8.53 | 69 | | |
| 980 | 280 | 80 | 116.72 | 0.25 | 10.43 | 87 | 77 | 95 |
| | 310 | 100 | 121.73 | | 11.65 | 74 | | |
| | 180 | 16 | 130.00 | | 3.60 | 93 | | |
| 808 | 218 | 18 | 124.10 | 0.125 | 4.61 | 100 | 95 | 95 |
| | 257 | 22 | 124.80 | | 4.78 | 91 | | |

| Laser wavelength (nm) | $P_0$ (mW) | $Q_r$ (mW) | $\tau_s$ GNSTs | OD GNSTs | ΔT(°C) GNSTs | $\eta_\alpha$(±10%) GNSTs | Average $\eta_\alpha$ | Simulated $\eta_\alpha$ GNSTs |
|---|---|---|---|---|---|---|---|---|
| | 115 | 35 | 90.97 | | 4.5 | 65 | | |
| 1280 | 130 | 45 | 101.28 | 1.06 | 5.07 | 49 | 56 | 91 |
| | 148 | 55 | 89.42 | | 5.52 | 55 | | |
| | 155 | 32 | 77.17 | | 6.28 | 89 | | |
| 980 | 350 | 80 | 73.82 | 3.9 | 13.06 | 83 | 84 | 87 |
| | 540 | 120 | 73.87 | | 19.53 | 80 | | |
| | 187 | 18 | 79.08 | | 7.62 | 98 | | |
| 808 | 290 | 40 | 79.43 | 4.835 | 11.4 | 90 | 90 | 87 |
| | 420 | 50 | 80.14 | | 15.48 | 84 | | |

In order to obtain an accurate statistical value of the scattering efficiency, experiments were carried out at different input powers for each one of the three illumination wavelengths here investigated (see **Figure 4.3** and **Table 4.1**). Note that once the scattering efficiency at a given wavelength ($\lambda$) is experimentally determined, it is possible to get the scattering extinction cross section at this wavelength, since:

$$\sigma_{sct}(\lambda) = \eta_{sct}(\lambda) \cdot \sigma_{ext}(\lambda), \tag{4.4}$$

where $\sigma_{ext}(\lambda)$ is the extinction cross section at wavelength $\lambda$ as experimentally determined from the extinction spectra included in **Figure 4.2**. In **Table 4.2**, the averaged scattering efficiencies,

extinction cross section and scattering cross section as obtained for each GNP (at the three wavelengths) are listed. Inspection of **Table 4.2** reveals that the largest scattering efficiencies and cross sections are provided by GNSs. Actually, the scattering efficiency of GNSs is higher than 50%, for the three wavelengths investigated in this work. Consequently, these results indicate that GNSs are the most suitable nanoparticles for scattering based imaging techniques, such as OCT and optical microscopy.[127, 165] This is in good agreement with the scattering efficiency estimated by means of simulation in **Chapter 3**. Data included in **Table 4.2** also reveal that the scattering efficiency is strongly wavelength dependent for all GNPs. Although GNSTs show very low scattering efficiencies at 800 and 980 nm they present a scattering efficiency close to 50% at around 1.3 μm.

**Table 4.2.** Experimentally determined scattering efficiency and scattering cross sections at three wavelengths investigated.

| | 808 nm | | | 980 nm | | | 1280 nm | | |
|---|---|---|---|---|---|---|---|---|---|
| | $\eta_{sct}$ | $\sigma_{ext}$ ($cm^2$) | $\sigma_{sct}$ ($cm^2$) | $\eta_{sct}$ | $\sigma_{ext}$ ($cm^2$) | $\sigma_{sct}$ ($cm^2$) | $\eta_{sct}$ | $\sigma_{ext}$ ($cm^2$) | $\sigma_{sct}$ ($cm^2$) |
| **GNSs** | 0.68 | $1.50\times10^{-9}$ | $1.02\times10^{-9}$ | 0.84 | $1.81\times10^{-9}$ | $1.52\times10^{-9}$ | 0.51 | $1.09\times10^{-9}$ | $5.56\times10^{-10}$ |
| **GNRs** | 0.05 | $1.64\times10^{-12}$ | $0.82\times10^{-13}$ | 0.23 | $5.00\times10^{-12}$ | $1.15\times10^{-12}$ | 0.12 | $1.42\times10^{-11}$ | $1.70\times10^{-12}$ |
| **GNSTs** | 0.10 | $2.55\times10^{-11}$ | $2.55\times10^{-12}$ | 0.16 | $2.06\times10^{-11}$ | $3.30\times10^{-12}$ | 0.44 | $5.59\times10^{-12}$ | $2.46\times10^{-12}$ |

## 4.4. Numerical calculations and comparison with experimental data

In this chapter, new numerical calculations were provided by Diego Romero and José A. Sánchez-Gil (Instituto de Estructura de la Materia (IEM-CSIC), Consejo Superior de Investigaciones Cientificas). The calculation process is illustrated below.

Full electrodynamic methods were used to calculate the spectral dependence of the extinction, absorption and scattering cross sections. For GNSs, the simulation method is the same as described in **Chapter 3**. For more complex shapes, such as GNRs and GNSTs, numerical calculations were carried out by means of a free software implementation, called SCUFF[166] (open-source software package for analysis of electromagnetic scattering problems using the method of moments). Gold permittivity data were obtained from Johnson and Christy measurements[167] and the medium

permittivity is assumed to be the water ($n$ = 1.33). Thus, GNRs were considered as cylinders with given length and radius, with endcaps terminated as hemispheres with the same radius.

For the particular case of GNSTs the situation is more complex and a crucial issue is how to define the nanostar geometry. In this regard, the definition of a nanostar shape is inspired by the TEM images (**Figure 4.1**). Rather than exploiting analytical formulation (as in Ref.[162], which poses some difficulties in the meshing procedure), each nanostars is assumed contain a spherical core, with fourteen elongated tips with semi-ellipsoidal shape, as shown in **Figure 4.4 (a)**. Due to the structural inhomogeneities shown in the TEM images of the GNTSs, the spherical core radius was fixed as $R$ = 15 nm, and the tip ellipsoidal cross section (along two short axes) as a circle with radius $r$ = 5 nm. The tip length $L$ (long axis of the ellipsoid) is then allowed to vary between 12-25 nm (which nearly corresponds to the tip length and angle ($\theta$ = atan($r/L$)), as observed in the TEM images. The resulting calculated cross sectional spectra are shown in **Figure 4.4 (b)** for monochromatic plane waves, with varying vacuum wavelength impinging onto the nanostars along the $x$ direction, and with linear polarization along the vertical axis (with respect to the nanostar shown in the inset). Strong LSPRs appear with narrow width in the range 700-950 nm, with a ratio between absorption and extinction of ~ 87%. In this regard, it should be emphasized that, despite the anisotropic shape of the nanostars, the resulting spectra are nearly isotropic and polarization independent. This was verified (though not shown) by varying the angle of incidence and the electric field polarization. Actually, this was also pointed out in reference,[163] even for smoother nanostars with fewer tips. The reason is that the LSPR, being essentially a dipolar resonance, is excited mostly at any angle of incidence, due to fact that the electric field vector stretches along the direction between any of the opposing nanostar tips, whose length (~2$R$+2$L$) in turn controls the LSPR wavelength. As a matter of fact, upon the nanostar tip length increases, the LSPR is red-shifted, covering the spectral range between 700-950 nm, consistently with the broad LSPR width measured experimentally (**Figure 4.2**). To shed light on such inhomogeneous broadening, a smoothed weighted average was carried out over all the spectra of different tip lengths, assigning approximate weighs according to the statistics of GNSTs shapes. The resulting simulated spectra have been included in **Figure 4.4**.

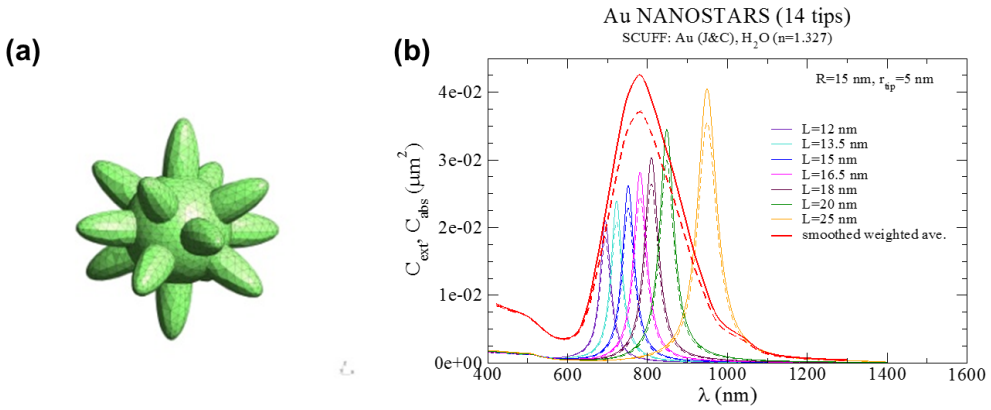


**Figure 4.4** (**a)** Schematic draw of a nanostar, containing an spherical core with fourteen elongated tips with semi-ellipsoidal shape. **(b)** Calculated extinction and absorption spectra considering a spherical core radius $R$ = 15 nm, with fourteen elongated tips with semi-ellipsoidal shape with $r$ = 5 nm short axes and varying long axis $L$ = 12, 13.5, 15, 16.5, 18, 20, 25 nm. A weighted average over all the spectra for different tip lengths is also shown (smoothed over ±5 nm), with approximate weighs extracted from the statistics of GNST shapes (TEM images, **Figure 4.1**): $L$ = 12 (13%), 13.5(22%), 15(22%), 16.5(22%), 18(22%), 20(17%), 25(4.4%) nm.

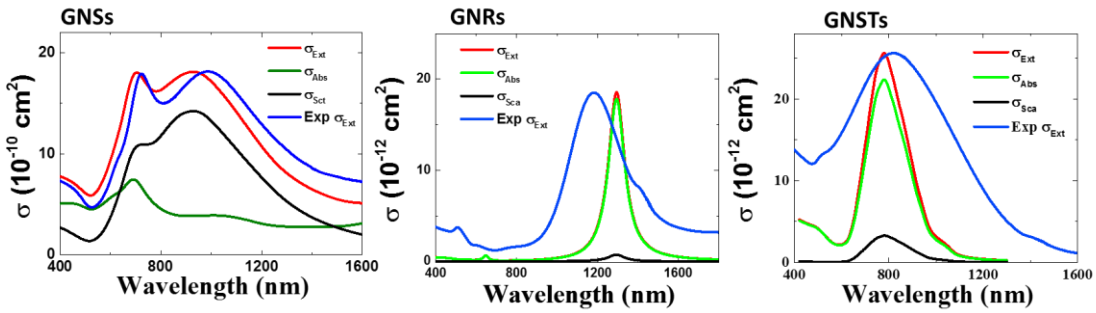


**Figure 4.5** Experimental extinction, calculated extinction, absorption and scattering cross section spectra of GNSs, GNRs and GNSTs in the I and II-BW.

The numerically calculated extinction, absorption and scattering cross section spectra in the spectral range 400-1600 nm (i.e covering BWs) are included in **Figure 4.5** as calculated for GNSs, GNRs and GNSTs. By comparing these data with the experimentally obtained extinction spectra, GNSs are in good agreement, while the spectral shapes are not properly reproduced neither for GNRs nor for GNSTs. For GNRs the calculated extinction cross section spectrum (peaking at about

1300 nm) appears shifted to longer wavelengths in respect to the experimental one (peaking at about 1200 nm). In addition, the calculated spectrum is narrower than the experimental one. For GNSTs, while the peak position is certainly reproduced, the calculated spectrum appears much narrower than the experimental one, and so leading to a large inaccuracy when determining the cross section values and the scattering efficiencies at long wavelengths. This experimental broadening is likely due to the non-uniform nanostar geometries (e.g. wide distribution of aspect ratio), as well as the finite-size effects, which broaden and dampen the resonance but do not influence the plasmon band position.[121] It should be borne in mind that this experimental broadening has been reported elsewhere also in connection with star-shaped nanoparticles,[121] as stemming from both the nonuniform nanostar geometries, and finite-size effects at the tip edges (shorter electron scattering mean free path). The former mechanism has been somehow taken into account through the average over GNSTs shapes inspired by the TEM images (**Figure 4.1 (a)**). Nevertheless larger shape variations and/or particle aggregation (not evidenced in the TEM images) might be responsible for the discrepancies. In addition, the other mechanism mentioned above, finite-size effects, also typically broadens resonance; it is due to increased electron damping resulting from electron scattering at the narrow tips, similar to what occurrs within GNSs thin shells.[168, 169]

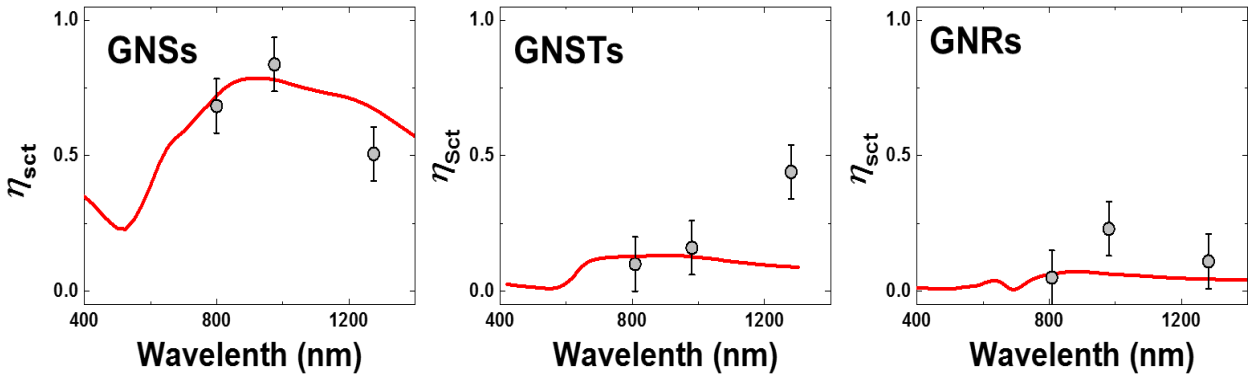


**Figure 4.6** Wavelength dependence of scattering efficiency of GNSs, GNSTs and GNRs. Solid line shows results extracted from calculations whereas the dots correspond to the experimental data obtained in this work (see **Table 4.2**).

By using the calculations included in **Figure 4.5**, the wavelength dependence of scattering efficiency can be also numerically calculated for all the investigated GNPs. Results of these

calculations are included in **Figure 4.6** together with here obtained the experimental data at the three used wavelength. According to these numerical calculations, the scattering efficiency is weakly dependent on wavelength for GNRs and GNSTs but strongly wavelength dependent for GNSs. While a good agreement between numerical simulations and measured efficiencies occurs at 800 nm and 980 nm, a clear disagreement is observed at around 1.3 μm (the IV-OCT wavelength) for GNSTs. At this specific wavelength, calculations predict a scattering efficiency of 0.09, much lower than that experimentally measured (0.44). While the origin of this discrepancy is not fully understood, the physical phenomenon behind this must be the same that leads to the appearance of the long wavelength tail in the extinction spectrum. It was assumed that the existence of interaction between individual GNSTs via agglomeration or slight contact between tips, could lead to dimer structures with completely different optical properties. In particular, the presence of such interacting structures could lead to red-shifts in the plasmon resonance and to larger scattering efficiencies. Regardless of the origin of these discrepancies, this highlight the importance of performing direct experimental measurements for the scattering efficiency at different wavelengths, as it was done in this chapter.

## 4.5. Infrared scattering experiments

To gain insight into the actual scattering efficiency of GNPs at long wavelengths, where the calculated and measured data display the largest discrepancy, two set of imaging measurements were carried out. In particular I investigated the infrared scattering abilities of the three types of GNPs by infrared dark field microscopy (IR-DFM) and IV-OCT. The results obtained in each case are described in the following.

### 4.5.1. Infrared dark field microscopy

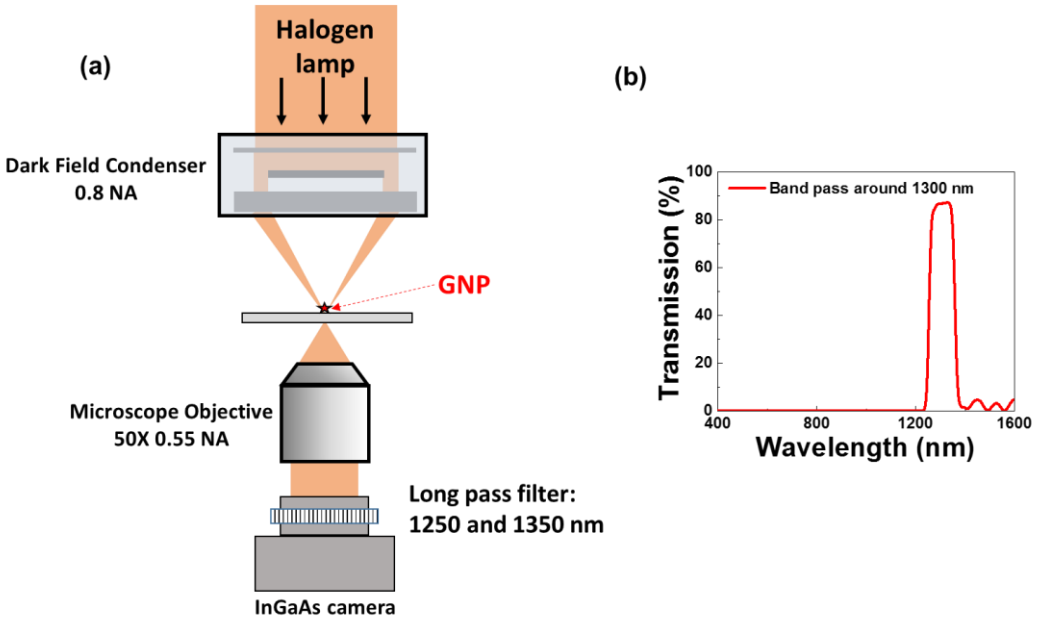


**Figure 4.7 (a)** Schematic representation of the experimental set up designed to evaluate the ability of GNSs, GNSTs and GNRs as contrast agents in a dark field configuration. **(b)** Band pass spectra around 1300 nm after substract the long pass light after 1250 nm by long pass light after 1350 nm.

For IR-DFM experiments the GNPs were deposited and dried onto the microscope slides. The microscope slides containing the GNPs were visualized by using the home-made IR-DFM, the schematically was drawn in **Figure 4.7 (a)**. In order to just get the infrared DFM Image (i.e. just record the dispersed light around 1280 nm), two long pass filters of cutting wavelengths 1250 nm and 1350 nm were used (see the experiemtal set up in **Figure 4.7 (a)**). In detail, the following transmission spectra; (1) after putting long pass filter 1250 nm and (2) after putting long pass filter 1350 nm were obtained. In such a way, a narrow band pass spectrum peaking around 1300 nm was obtained after substract (1) by (2), as shown in **Figure 4.7 (b)**. Therefore, only the infrared radiaton sattered by the GNPs in the wavelength range from 1250 nm to 1350 nm was obtained. Consequently, the here employed IR-DFM system is able to visualize individual GNPs by using their scattering abilities at 1300±50 nm. **Figure 4.8 (a)** shows the IR-DFM images obtained for the three GNPs studied in this chapter. Up to the best of my knowledge, these are the first ever reported IR-DFM images of GNPs in the II-BW. As can be observed, all GNPs can be detected by IR-DFM, revealing a non-vanishing scattering cross section in the three cases (in accordance with

the experimental data included in **Figure 4.6**). The largest IR-DFM contrast has been provided by GNSs, being significantly larger than those provided by GNSTs and GNRs. This is more clearly evidenced in **Figure 4.8,** in which I have included the average IR-DFM intensity per spot generated by GNSs, GNRs and GNSTs. The results included in **Figure 4.8** are, therefore, in qualitative agreement with the experimentally determined and numerically calculated values of the scattering cross section (see **Table 4.2**). These experimental data confirm that GNSs provide the largest infrared scattering cross section among the all geometries here studied.

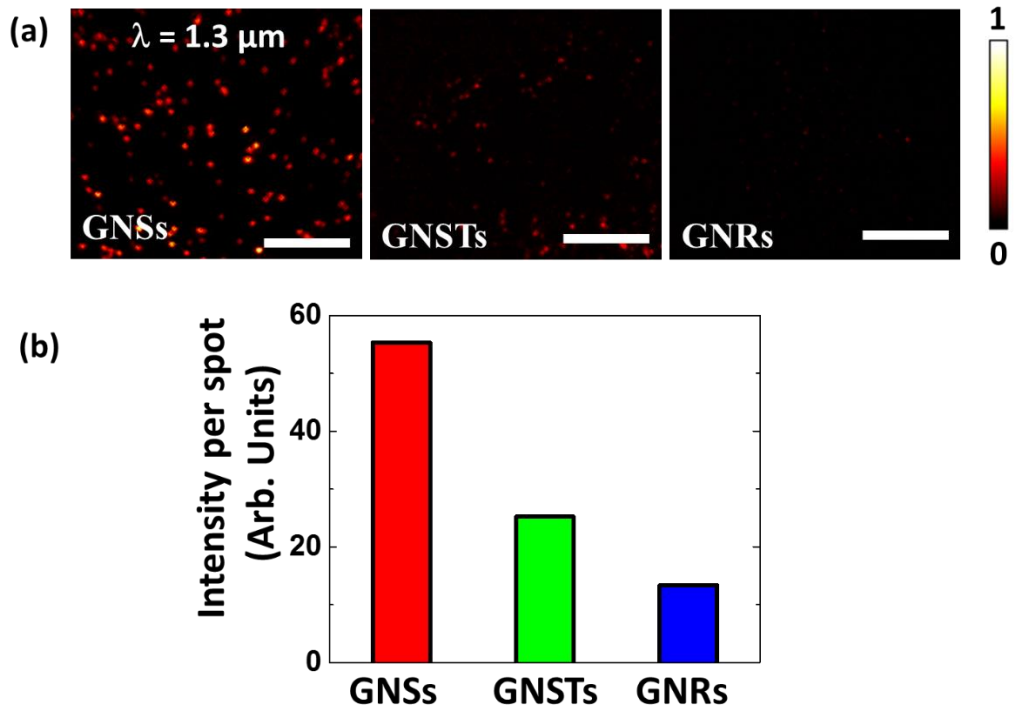


**Figure 4.8 (a)** Infrared dark field images obtained at 1.3 μm by using GNSs, GNRs and GNSTs as potential contrast agents. Scale bar is 20 μm in all the cases. **(b)** Average intensity per nanoparticle generated by GNSs, GNRs and GNSTs as obtained from the statistical analysis of IR-DFM images.

### 4.5.2. Intravascular optical coherence tomography

The infrared scattering ability of the different GNPs at around 1.3 μm (the IV-OCT laser wavelength) has also been investigated by performing IV-OCT experiments. In this case, a colloidal solution of each type of GNP was injected into a tubing (see **Experimental techniques**). Once the aqueous solutions of GNPs were inside the tubing (mimicking an artery), the IV-OCT

catheter was introduced into the tubing allowing for the static detection of the individual GNPs, by means of their back-scattering efficiency.[24] It should be noted that the advantage of this interferometric technique OCT is that it provides an indirect measure of the infrared back-scattering cross section at the single wavelength of 1.3 μm. **Figure 4.9** shows the IV-OCT cross sectional images for the colloidal solutions containing the three investigated GNPs. Again, the three geometries here studied produced a significant IV-OCT signal. This again reveals a non-vanishing infrared scattering cross section at around 1.3 μm. It is also evident from **Figure 4.9 (a)** that the IV-OCT contrast is provided by each type of GNP. **Figure 4.9 (b)** includes the averaged OCT intensity (contrast) provided by individual GNPs, as obtained for each type of GNP. Again, and as we also obtained in **Chapter 3**, it is found that the largest contrast is provided by GNSs, revealing their superior scattering cross section.

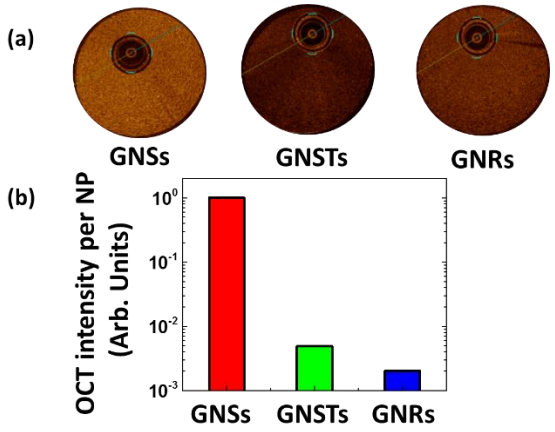


**Figure 4.9 (a)** OCT cross section images of colloidal solutions containing GNSs, GNSTs and GNR. **(b)** OCT intensities of single GNSs, GNSTs and GNRs obtained from the statistical analysis of figures included at the left column.

At this point, the concordance between experimental data included in **Figure 4.9** and those of **Table 4.2** can be discussed. For a sample of thickness *d* containing a certain numer of GNPs, i.e. *N*, the Lambert-Beer exctinction law gives the fraction of scattered intensity:

$$\frac{I_0 - I}{I_0} = 1 - e^{-\sigma_{sct} N d}, \tag{4.5}$$

where $I_0$ is the incident light intensity and $I$ the light intensity transmitted through the sample. For low values of the exponential exponent, and assuming the same thickness for all measurements (same geometrical conditions), Equation (4.5) can be written as:

$$\frac{I_0 - I}{I_0} \approx \sigma_{sct} N d, \tag{4.6}$$

thus the OCT intensities (per GNP) given in **Figure 4.9 (b)** should be proportional to the fraction of scattered light and so to experimental values of $\sigma_{sct}$ (indeed to the backscattering cross section) given in **Table 4.2**. Now, the OCT intensity per GNP ($I_{oct,}$) (for each type of GNP) normalized to that given by the GNSs (the best scatterers) was compared. From the data given in **Figure 4.9**, I obtained:

$$I_{oct}(GNSTs) \Big/ I_{oct}(GNSs) = 5 \times 10^{-3} \tag{4.7}$$

and

$$I_{oct}(GNRs) \Big/ I_{oct}(GNSs) = 2 \times 10^{-3}. \tag{4.8}$$

These values are indeed close to the ratio between the scattering cross sections experimentally obtained and listed in **Table 4.2**, that leads to: $\sigma_{sct}(GNSTs)/\sigma_{sct}(GNSs) \approx 4.42 \times 10^{-3}$ and $\sigma_{sct}(GNRs)/\sigma_{sct}(GNSs) \approx 3.05 \times 10^{-3}$. In fact, the slight discrepancy could be due to the different geometries that lead to different backscattering/scattering ratios. Therefore, at this point, the IV-OCT experimental results confirm the validity of the scattering efficiencies (and so the scattering cross sections) experimentally determined in this thesis by the photo-thermal method. In fact, the results here reported highlight the need of a direct experimental determination of the scattering efficiency, particularly at longer wavelengths (as for the OCT wavelength), where numerical calculations for GNRs and GNSTs fail to explain the experimentally obtained extinction cross section (see **Figure 4.2** and **Figure 4.5**). Therefore, the experimental determined scattering efficiencies are crucial to provide reliable values.

### 4.5.3. Optoacoustic experiments

An indirect estimation of the geometry dependence of the scattering efficiency of GNPs can be also obtained by the performance of IR-OA experiments.[170] For this purpose I prepared colloidal

solutions containing the three types of GNPs with exactly the same OD at 1064 nm (this being the wavelength used in our IR-OA experiments), as shown in **Figure 4.10 (a)**. Each solution was introduced in a quartz cuvette mechanically attached to a piezo transducer, connected to signal amplifier and to a digital oscilloscope. In absence of any fluorescence (as in our case) the magnitude of the IR-OA signal is proportional to the fraction of absorbed pump power ($P_{abs} = P_0 \cdot (1 - 10^{-OD})$), where $P_0$ is the incident pump power that is converted into heat. In other words, the OA signal is expected to be proportional to $\eta_{abs} \cdot P_{abs}$. Therefore, we can write:

$$I_{OA} = k \cdot (1 - \eta_{sct}) \cdot P_0 \cdot (1 - 10^{-OD}), \tag{4.9}$$

where *k* is a coupling constant that depends on the Grüneisen parameter and the experimental conditions such as the gain of the piezo transducer.[171] From Equation (4.9), it is clear that the IR-OA signal is proportional to $(1 - \eta_{sct})$ in such a way that those GNPs with largest scattering efficiencies and with the same OD should give the lowest IR-OA signal. **Figure 4.10 (b)** shows the IR-OA signals generated by the three GNPs studied in this work. The three geometries generate measurable IR-OA signals even though with quite different amplitudes. The averaged IR-OA amplitudes obtained for the three cases are displayed in **Figure 4.10 (c)**. In this case, the lowest IR-OA signal was generated by the GNSs. This is in close agreement with the experimental data displayed in **Figure 4.6** and with Equation (4.9) that predicts the lowest IR-OA for the GNPs with the largest scattering efficiency. Data included in **Figure 4.10 (c)** allows for a quantitative estimation of the relation between the infrared scattering efficiencies of the different GNPs studied in this work. Equation (4.9) can be rewritten to get a formal expression for the OA intensity ratio between GNSTs and GNSs, so that:

$$R_{OA}\left(\frac{GNSTs}{GNSs}\right) = \frac{I_{OA}(GNSTs)}{I_{OA}(GNSs)} = \frac{1 - \eta_{sct}(GNSTs)}{1 - \eta_{sct}(GNSs)}. \tag{4.10}$$

Analogously, Equation (4.10) can be written for the ratio that compares GNRs and GNSs, as follows:

$$R_{OA}\left(\frac{GNRs}{GNSs}\right) = \frac{I_{OA}(GNRs)}{I_{OA}(GNSs)} = \frac{1 - \eta_{sct}(GNRs)}{1 - \eta_{sct}(GNSs)}. \tag{4.11}$$

From the experimental IR-OA data, I obtained $R_{OA}\left(\frac{GNSTs}{GNSs}\right) \approx R_{OA}\left(\frac{GNRs}{GNSs}\right) \approx 6$. From the experimentally determined scattering efficiencies (**Table 4.2**), I obtained $R_{OA}\left(\frac{GNSTs}{GNSs}\right) \approx R_{OA}\left(\frac{GNRs}{GNSs}\right) \approx 4$. Therefore, it is found that the infrared scattering efficiencies determined by the transient photo-thermal method, are in good agreement with optoacoustic experiments of the GNPs studied in this work.

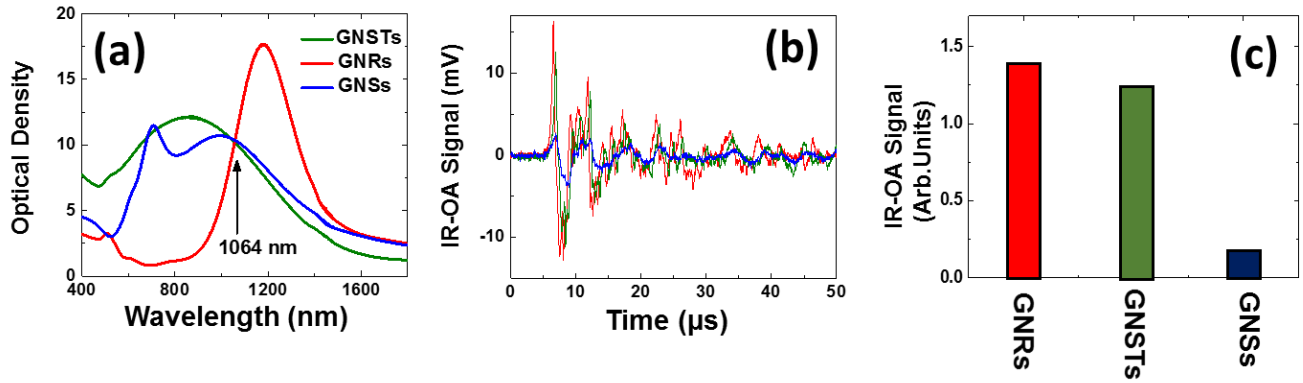


**Figure 4.10 (a)** Optical density of GNRs (red), GNSTs (green) and GNSs (blue). **(b)** Time evolution of the IR-OA signals generated by the three GNPs after laser excitation. **(c)** Average IR-OA amplitudes obtained for the three GNPs.

## 4.6. Conclusions

An experimentally determination of infrared scattering efficiency and scattering cross section of GNPs with three different geometries: nanorods, nanoshells and nanostars was carried out in this chapter. Multi-wavelength thermal loading experiments have been used to experimentally determine the spectral dependence of the scattering efficiency of these three geometries. Comparison between experimental data and numerical simulation, reveals good agreement in all cases, except for GNSTs that present an unexpected large scattering efficiency at long wavelengths. This discrepancy has been explained in terms of size inhomogeneities as well as particle-particle interactions. Both GNSs and GNSTs show scattering efficiencies strongly dependent on the wavelength, thus evidencing the importance of considering the spectral operating range when choosing the appropriate geometry for each particular imaging application. It is also experimentally found that, in the whole infrared spectral range investigated in this work (800-1400

nm), GNSs show the largest scattering efficiency and cross section. This explains, why they are best cardiovascular imaging probes, as we also concluded in **Chapter 3**.

The superior performance of GNSs as scattering units in the infrared has been confirmed by means of infrared dark field imaging, optical coherence tomography and optoacoustic experiments. In all the cases, the experimental data confirm the previous conclusions extracted from photothermal experiments. They also reveal the multifunctional character of these GNPs that are capable of efficient light scattering and acoustic generation under infrared optical excitation.

# Chapter 5. GNSs as contrast agent for cell imaging and tissue contrast enhancement by OCT

## 5.1. Introduction

IV-OCT imaging is nowadays used as a minimally invasive technique for the *in vivo* identification and assessment of unstable atheroma plaques as well as for the guidance of interventional procedures, such as atherectomy and stent placement.[24, 172-175] The possibility of adding molecular contrast to available IV-OCT systems opens a new door to extend the impact of OCT to cardiovascular clinical applications, as it would enable functional biomolecular imaging together with available morphological imaging. Indeed, IV-OCT with molecular contrast would enable site-specific cardiovascular imaging and therefore would allow for the early detection and localization of atherosclerotic lesions, which is not possible by using current IV-OCT imaging techniques. Thus, this intravascular molecular imaging modality would contribute substantially to the future development of personalized medicine for cardiovascular diseases.

A common strategy to improve OCT contrast at the molecular level involves the use of nanoparticles (NPs) that enhance OCT contrast and, at the same time, can be properly functionalized with antibodies to target specific molecules overexpressed by the tissue/cells to be detected.[106, 176] In this respect, GNPs of different geometries and sizes have been successfully applied as OCT contrast enhancers.[82, 149, 177-181] GNPs are particularly suitable for OCT contrast improvement as their extinction spectra can be precisely tuned over a broad spectral range by solely controlling their size and geometry. In addition, the gold surface of GNPs is particularly suitable for functionalization with specific targeting ligands and therefore provides the opportunity for molecular targeting.[181] Owing to these properties, GNPs have already been deployed as contrast agents in different OCT imaging modalities.[81, 182, 183] Moreover, as gold is an inert and biocompatible noble metal, these GNPs are considered nontoxic, although some concerns have been raised, especially related to the long-term effect of gold accumulation in the organism or cellular modifications.[184]

In **Chapter 3**, it was described how different types of commercial GNPs, including gold nanorods and gold nanoshells (GNSs), with plasmon resonances in the proximity of 1320 nm, could act as efficient IV-OCT enhancers when suspended in biomedical fluids.[179] In particular, GNSs consisting of a dielectric silica core of about 200 nm and an ultrathin metal shell of about 15 nm, resulted in the largest IV-OCT contrast enhancement based on their superior backscattering

cross-section ($0.7 \times 10^{-10}$ $cm^2$) at the IV-OCT wavelength.[179] As a result, GNSs dispersed in physiological solutions could be individually observed by IV-OCT, even under dynamic flow conditions. Despite these promising features, the potential use of GNSs for the selective enhancement of live cell imaging by IV-OCT must be explored, though it would constitute the first step towards the use of IV-OCT for molecular imaging.

In this chapter, a systematic investigation of IV-OCT contrast in living cells and its enhancement by passive incubation with GNSs is presented. Experiments were conducted in two different cell lines; HeLa and Jurkat cells. (i) HeLa cells constitute an immortal cell line, as they can divide many times in cell culture plate under minimal survival conditions. Thus, they have been widely used for scientific research. What's more, as cancer cells, they are capable to uptake NPs by endocytosis. (ii) Jurkat cells are T lymphocytes and can be found in the blood stream. Recent studies have shown that they play an important role in protecting against cardiovascular diseases by responding to inflammatory cues.[185, 186] Therefore, the investigation of these two cell lines for OCT molecular imaging is important. Intensity analysis of IV-OCT was used to discriminate the population of living cells in which an efficient incorporation of GNSs was achieved and to determine the relationship between the incorporation efficiency and the incubation parameters. The results extracted from the IV-OCT images of cell dispersions were compared to the images obtained by transmission electron microscopy (TEM) and dark field microscopy (DFM), in order to unequivocally correlate the contrast enhancement observed in the IV-OCT images with the incorporation of GNSs in living cells. Future implications of the results for the application of IV-OCT to intracoronary molecular imaging are also discussed.

## 1.1. Static OCT imaging of HeLa and Jurkat cells incubated with GNSs

As indicated in the Introduction, and with the purpose of studying IV-OCT contrast for living cells and its enhancement by passive incubation with GNSs, cytotoxicity was initially examined using various concentrations of GNSs incubated on HeLa cells for 24 h. MTT assay was then used to evaluate the cytotoxicity of the GNSs, more details can be found in **Experimental techniques**. The results of these experiments are shown in **Figure 5.1**. For all the concentrations (0.05, 0.1, 0.5, 2.5, and 5 μg/mL), the cell viability was never less than 94% relative to the control. Therefore, the GNSs did not show any relevant toxicity to the HeLa cells under these experimental conditions.

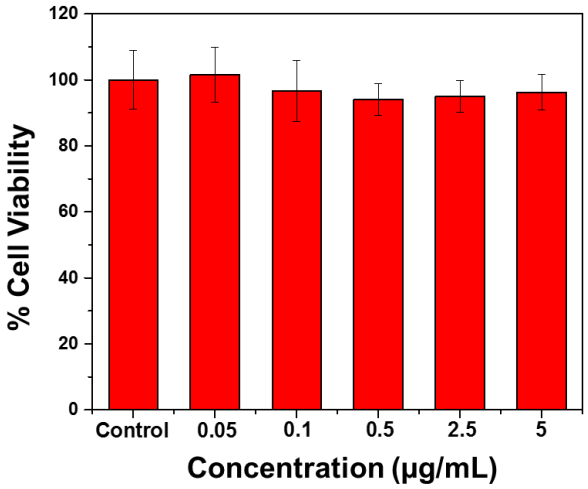


**Figure 5.1** Cell viability of HeLa cancer cells after incubation with several concentrations of GNSs. Each bar corresponds to the mean value ±standard deviation (SD) obtained from 4 replicates for each experimental condition.

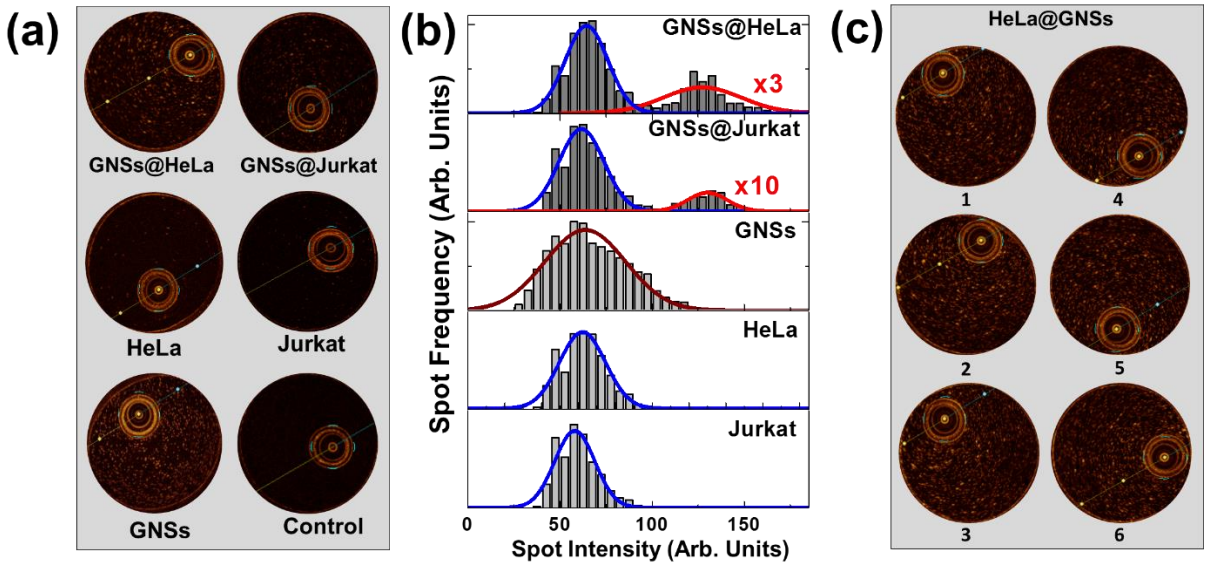


**Figure 5.2 (a)** IV-OCT cross-sectional images of GNSs suspended in PBS , nonincubated HeLa and Jurkat cells in PBS, HeLa and Jurkat cells incubated for 24 h with a dispersion of GNSs in PBS. **(b)** Histograms of intensity, as calculated from the IV-OCT images. Note that free GNSs and free (nonincubated) Jurkat and HeLa cells yielded single Gaussian distributions centered at about 65 $u_{arb}$ (GNSs) and 60 $u_{arb}$ (free cells), whereas the incubation of HeLa and Jurkat cells with GNSs led to the appearance of high-intensity

bands centered at about 120 $u_{arb}$. The different fits to Gaussian distributions are shown as solid lines. ×3 and ×10 indicate the magnification factor. **(c)** Representative IV-OCT cross-sectional images of HeLa cells incubated with 5 μg/mL GNSs for 24 hours, obtained by injecting the sample (1, 2 and 3) and its duplicate (4, 5 and 6) in the tubing at different times, and moving the IV-OCT catheter in 3 positions along the tubing.

After the negligible toxicity of the GNSs was proved, the GNSs were incubated in cells (HeLa and Jurkat) to evaluate their viability as OCT contrast agents. HeLa cells were incubated with 2.5 μg/mL of GNSs for 24 hours, while Jurkat cells were incubated with 1.0 μg/mL of GNSs for 24 hours. Both of them were washed for three times in order to remove the excessed GNSs, and then they were dispersed in PBS. Then 200 μL of the incubated cells/PBS solution were injected in a tubing containing the IV-OCT catheter. In order to make a comparison, the following control samples were also prepared and then injected into the tubing: (i) PBS solution, (ii) 2.5 μg/mL of GNSs in PBS, (iii) non-incubated HeLa and Jurkat cells in PBS solution. **Figure 5.2 (a)** shows OCT cross-sectional images of the tubing filled with these solutions. As we have seen in **Chapter 3**, individual GNSs can be visualized by IV-OCT when using a low concentration of GNSs. The different bright spots in the cross-sectional images are due to the backscattered light of the OCT laser produced by (i) individual GNSs, (ii) individual cell, (iii) cell containing GNSs. Thus, the cross-sectional images in **Figure 5.2 (a)** must be carefully analyzed. For this purpose, the spot intensity distribution of these cross-sectional images was carefully analyzed. **Figure 5.2 (b)** shows the spot intensity distribution (spot frequency as a function of the OCT spot intensity) obtained for the different samples. The data analysis process is described in detail in **Experimental techniques**. Each distribution was obtained by analyzing the intensity of 120 images taken along the tubing. To guarantee the accuracy, the experiment was repeated at least 6 times for each concentration by injecting each sample and its duplicate (another solution with same GNSs concentration) in the tubing, and moving the IV-OCT catheter to 3 different positions along the tubing. An example of these repeated experiments for HeLa cells incubated with GNSs is shown in **Figure 5.2 (c)**. In these six IV-OCT cross sectional images, bright spots and less bright spots can be clearly seen, giving no significant differences in the spot intensity distribution, thus demonstrating that the data obtained in these experiments are reproducible. For the solution containing only GNSs, a single distribution of spot intensities was observed around a central spot intensity of about 65 $u_{arb}$ (in the contrast units given by the IV-OCT software, hereafter $u_{arb}$) with a full width at half maximum (FWHM) of 50 $u_{arb}$. This distribution resembled a Gaussian one, as depicted by the best-fit curve

displayed over the distribution. Cross-sectional images of the PBS solutions containing HeLa and Jurkat cells also show bright OCT spots, demonstrating the ability of IV-OCT to detect individual cells. The corresponding spot diagrams are shown in the right panel of **Figure 5.2**. In both cases, Gaussian distributions with peaks at about 59 $u_{arb}$ and an FWHM close to 26 $u_{arb}$ were obtained. Thus, when compared to the histogram of IV-OCT signal intensities provided by colloidal GNSs, it was clear that suspended cells (either HeLa or Jurkat) produce much narrower distributions, peaking at slightly different OCT intensities. **Figure 5.2 (b)** also includes the intensity histograms corresponding to the IV-OCT cross-sectional images obtained for cells that were incubated with GNSs for 24 h. It can be clearly observed that the incubation process results in the appearance of a number of OCT spots at higher intensities than those obtained for single GNSs and for nonincubated cells. In these cases, the intensity histogram can be effectively described by the superposition of two Gaussian distributions as follows: 1) the dominant contribution corresponds to a Gaussian distribution centered at 62 $u_{arb}$ with an FWHM close to 25 $u_{arb}$. As the distribution peak is located at 65 $u_{arb}$ for free GNSs and at 59 $u_{arb}$ for cells only, we can consider that this contribution is associated to free GNSs, cells that did not incorporate GNSs, and cells incubated with several GNSs. A possible explanation of these results will be given when describing the dark field images results. 2) The experimental data reveal an additional Gaussian distribution with a peak at about 125 $u_{arb}$ and a FWHM of 50 and 26 $u_{arb}$ for HeLa and Jurkat cells, repectively. This second Gaussian distribution is associated with cells that internalized GNSs, or GNSs that are adhered to the cells during the incubation procedure. Note that in these cases, the backscattering signal is expected to be higher, since it represents two different contributions, i.e., the backscattered signals produced by the medium–cell interface and by intracellular GNSs.

## 1.2. Additional confirmation of the internalization of the GNSs into the cells

Dark field microscopy (DFM), which collects the scattered light produced by an specimen, is a good technique to localize and monitor good light scatterers, like plasmonic nanoparticles.[187] Therefore, the DFM was used to confirm the intracellular incorporation of GNSs, as shown in **Figure 5.3**. **Figure 5.3 (a)** and **(c)** show, as relevant examples, DFM images of HeLa and Jurkat cells obtained after 24 h of incubation with GNSs in PBS at of 2.5 and 1 µg/mL, respectively. In this case, the DFM images were taken by uEye camera (Germany). According to previous studies based on DFM visible imaging, the color of GNPs in the DFM is dependent on the scattering

spectra of the GNPs. For example, gold nanoparticles with scattering spectrum peaking at 547 nm show green color in DFM, while the GNRs with scattering spectrum peaking at 687 nm show a red color in the DFM.[188] However as GNSs display a stronger scattering intensity in the infrared region, they might not be properly imaged by a visible camera. Fortunately, due to the broad scattering spectra of GNSs from 600 to 1400 nm (as discussed in **Chapter 4)**, a visible camera can still be used to image the GNSs, and the color is expected to be red. As observed in the DFM images in **Figure 5.3 (a)** and **(c)**, the red spots are thus associated with GNSs. Therefore, DFM images provide solid evidence for the incorporation of GNSs in both HeLa and Jurkat cells. In addition, the visualization of cells incubated with GNPs by TEM have been widely used,[189, 190] due to the different contrast and morphology that cells and GNPs show in TEM. Therefore, TEM was used to further support the conclusions obtained by DFM. **Figure 5.3 (b)** and **(d)** show representative TEM images of HeLa and Jurkat cells obtained after incubation with GNSs, clearly showing the presence of GNSs in the cytoplasm of the cells.

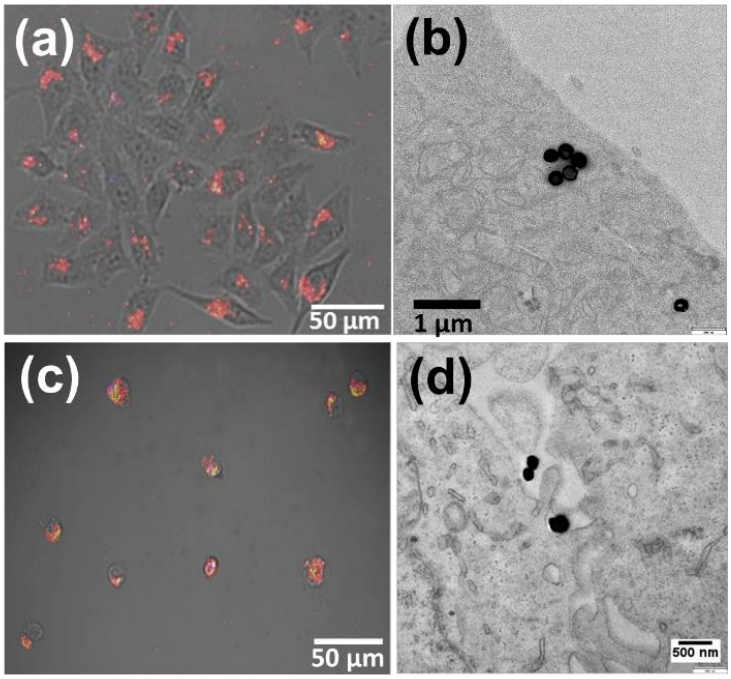


**Figure 5.3** Dark-field microscopy and bright field microscopy images (merged) of HeLa **(a)** and Jurkat cells **(c)** incubated in a dispersion of GNSs in PBS at 2.5 and 1 µg/mL, respectively. TEM image of a HeLa **(b)** and a Jurkat cell **(d)** incubated in a solution of GNSs in PBS at 2.5 and 1 µg/mL, respectively. The intracellular incorporation of GNSs in cells is corroborated.

### 1.3. Incubation efficiency of GNSs incubated into the cells

The data summarized in **Figure 5.2** clearly demonstrate how the incubation of the GNSs in cells leads to complex bright spots distributions in the cross-sectional OCT images. It has been shown that a Gaussian fitting can be used to discriminate the cells that has been efficiently incorporated with GNSs. In order to see how the internalization efficiency was affected by the concentration of the GNSs, IV-OCT cross-sectional images of cells incubated for 24h with GNSs at various concentrations (from 0.05 µg/mL to 5 µg/mL) were analyzed. **Figure 5.4 (a)** shows the cross-sectional IV-OCT images obtained for HeLa cells incubated with 0.05, 0.1, 0.5, 2.5 and 5 µg/mL of GNSs. The IV-OCT image of control (cells not incubated with nanoparticles) is also shown in **Figure 5.4 (a)** for comparison. With the increase of the GNSs concentration, more spots appeared in the cross-sectional images and more bright spots were observed. The spot intensity distributions obtained for different incubated concentrations are displayed in **Figure 5.4 (b)**. It was previously demonstrated that the cells that have internalized GNSs give signals in the 120-190 $u_{arb}$ range (red Gauss fitting as shown in the **Figure 5.2 (b)).** Therefore, by direct computation of the total number of spots with intensities in the 120–190 $u_{arb}$ range, it is possible to obtain a relative measure of the population of cells with GNSs in their cytoplasm. The results obtained from the analysis of the intensity histograms in **Figure 5.4 (b)** are included in **Figure 5.4 (c)**. This figure demonstrates that the sub-population of HeLa cells that internalizes GNSs increases as the concentration of GNSs increases in the culture medium. IV-OCT images revealed that for GNS concentrations below 0.5 µg/mL the internalization efficiency strongly depends on the GNS concentration, whereas for larger concentrations, the internalization efficiency tends to saturated and so is only slightly dependent on the incubation concentration. Interestingly, the number of incubated cells (>120 $u_{arb}$) reaches a maximum for the highest concentration of GNSs (2656) that is quite similar to the same number of HeLa cells (2735) in the control. Therefore, it can be considered that OCT can be efficiently used for imaging of HeLa cells.

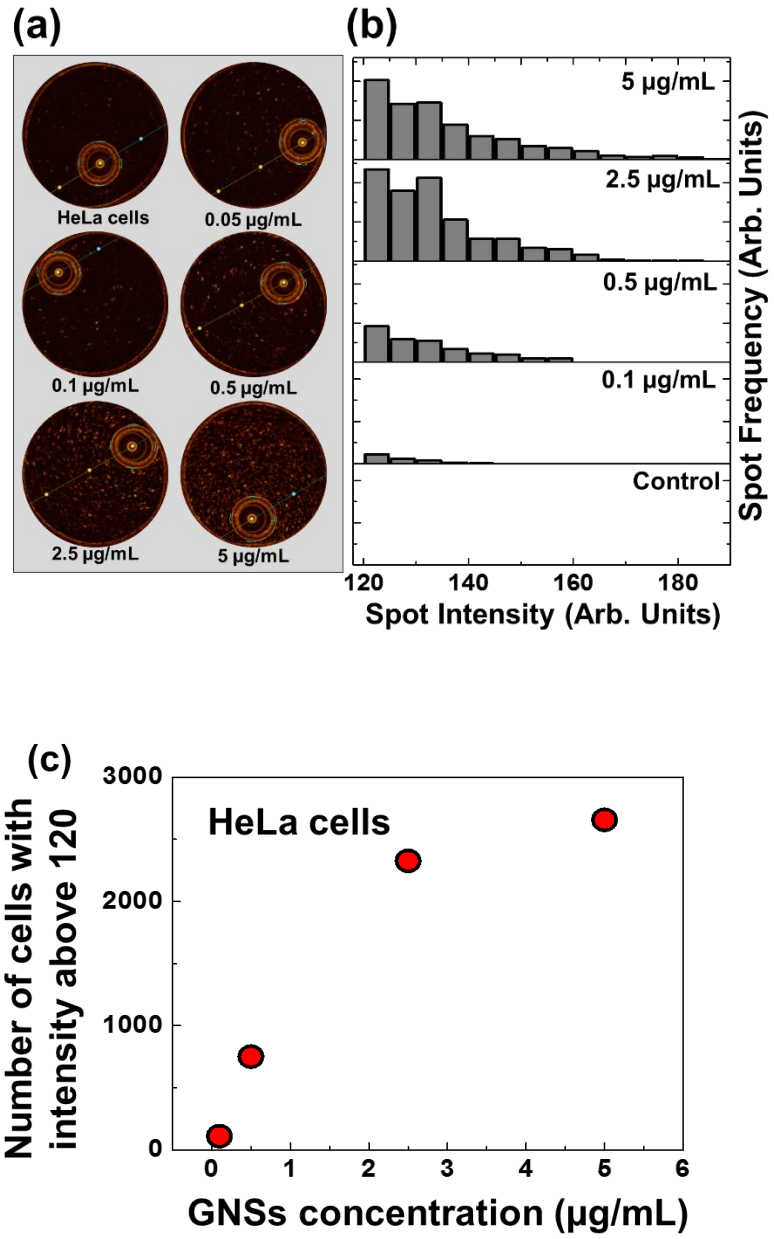


**Figure 5.4 (a)** IV-OCT cross-sectional images of nonincubated HeLa cells and HeLa cells incubated for 24 h with various concentrations of GNSs. **(b)** Intensity histograms as calculated from the IV-OCT cross-sectional images for spots intensities larger than 120 $u_{arb}$. **(c)** Number of cells with intensity above 120 $u_{arb}$ generated from HeLa cells incubated with various concentrations of GNSs for a fixed time of 24 h.

A similar trend was observed when the internalization efficiency of GNSs by Jurkat cells was determined based on IV-OCT images, as shown in **Figure 5.5 (a)**. The spot intensity distributions obtained for various incubated concentrations are displayed in **Figure 5.5 (b)**, where the intensity

range was restricted to 100-160 $u_{arb}$. Interestingly, in the case of Jurkat cells, which present a lower phagocytosis ability than HeLa cells, the GNSs were incorporated in the cells in a sufficient amount to increase the OCT signal, enabling the discrimination between individual cells and cells with GNSs. The integrated OCT intensity with spot intensity above 100 as function of GNSs concentrations is shown in **Figure 5.5 (c)**. The integrated OCT intensity shows also a similar trend with increase of GNSs concentrations to that observed for incubated HeLa cells (see **Figure 5.4 (c)**).

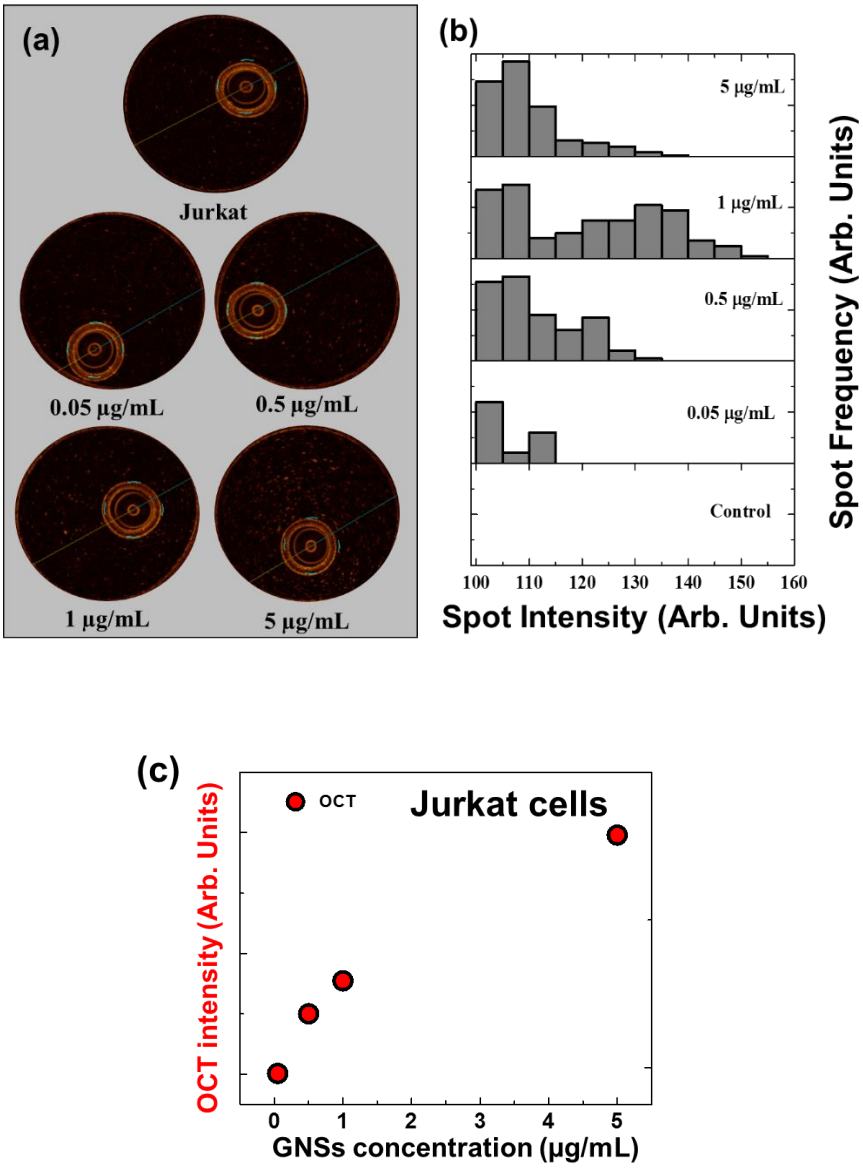

**Figure 5.5 (a)** IV-OCT cross-sectional images of nonincubated Jurkat cells and Jurkat cells incubated for 24 h with various concentrations of GNSs. **(b)** Intensity histograms as calculated from the IV-OCT cross-sectional images for spots intensities larger than 100 $u_{arb}$ (associated only with signals of cells that have incorporated GNSs). **(c)** Integrated OCT intensities generated from Jurkat cells incubated with various concentrations of GNSs for a fixed time of 24 h. The OCT signal was calculated by integrating the frequency distribution signals for spot intensities above a threshold intensity of 100 $u_{arb}$ (IV-OCT signal of successfully incubated cells).

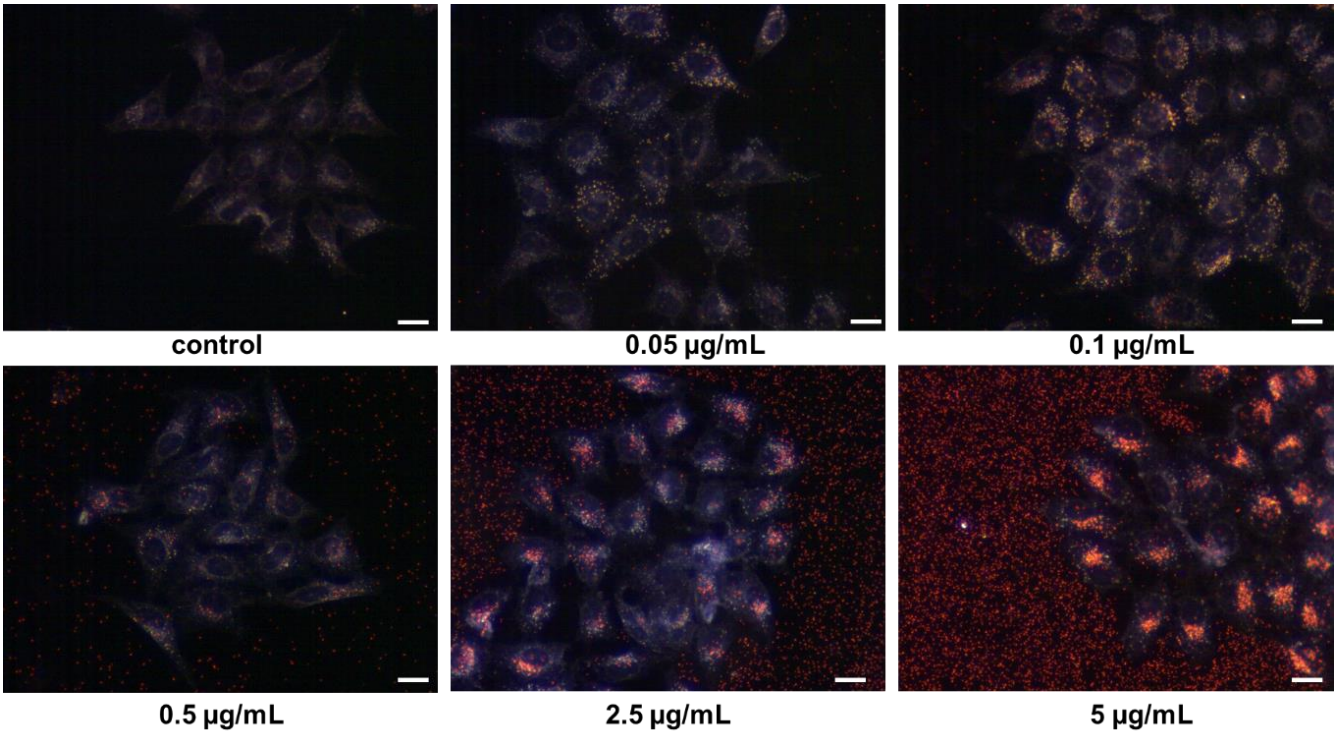


**Figure 5.6** Dark-field microscopy images of HeLa cells incubated with various concentrations of GNSs. Incubation time was 24 h in all cases: The scale bar is 20 µm.

A comparison of data obtained by IV-OCT and those obtained by DFM was performed for HeLa cells. The DFM images obtained for HeLa cells incubated with various GNSs concentrations were systematically studied, representative images are shown in **Figure 5.6.** These images clearly indicate that the number of red spots in cells increases with the concentration of GNSs in the incubation medium. The analysis of DFM images also allows for a qualitative evaluation of the adhesion efficiency of GNSs, by computing the average number of "red spots" per cell as a function of the GNS concentration. Assuming that each "red spot" corresponds to an individual

GNSs, it can be discussed how the number of GNSs incorporated to cells changes with the GNSs concentration as shown in **Figure 5.6.** The concentration-dependent incubation efficiencies, determined by DFM, for HeLa cells are included in **Figure 5.7**, together with the OCT trends obtained from **Figure 5.4 (b)** (i.e. the spots with OCT spot intensity above 120 $u_{arb}$). The average number of GNSs in cells were calculated by counting the red spots in the HeLa cells, using the images shown in the **Figure 5.6** It is clear that the DFM results were consistent with the IV-OCT results. The DFM images also reveal that the incorporation (or adhesion) efficiency of GNSs in living cells increases monotonically as the concentration of the GNSs in the culture medium increases. It can be also observed a tendency towards saturation for concentrations larger than 0.5 μg/mL, in very good agreement with the data extracted from IV-OCT images. This saturation behavior, evidenced by both DFM and IV-OCT, was in accordance with previous studies showing that the cellular uptake efficiency displays a saturation behavior as the concentration of nanoparticles increases.[51, 191] This is due to the limited number of available serum proteins in cells, which plays an important role in the internalization of gold nanoparticles.[191] In the DFM image of HeLa cells incubated with 0.05 μg/mL of GNSs, there are only 2 GNSs per cells (in average). By observing the corresponding OCT signal (**Figure 5.4** and **Figure 5.7**), there are no spots with intensity above 120 $u_{arb}$. Thus, HeLa cells incubated with 2 GNSs do not lead a contrast enhancement in the OCT cell imaging; the signal must be so low that it is impossible to detect the HeLa cells incorporated with GNSs. For HeLa cells incubated with 5 μg/mL of GNSs, the spots outside the cells are due to GNSs that have not been removed by the washing process. Note that some HeLa cells do not have as many GNSs as other HeLa cells, thus they may lead to the different OCT intensity in the OCT cross-sectional. For example, HeLa cells incubated with 1 or 2 GNSs result in a low OCT intensity (below 120 $u_{arb}$), and HeLa cells incubated with 10 to 45 GNSs produce a high OCT intensity (above 120 $u_{arb}$). This fact may give a reasonable explanation to the blue Gauss fitting in **Figure 5.2 (b)** with OCT intensity distribution from 40 to 120 $u_{arb}$. This OCT intensity distribution must be due to the backscattered light produced by the free GNSs, nonincubated HeLa cells, and HeLa cells incubated with several GNSs.

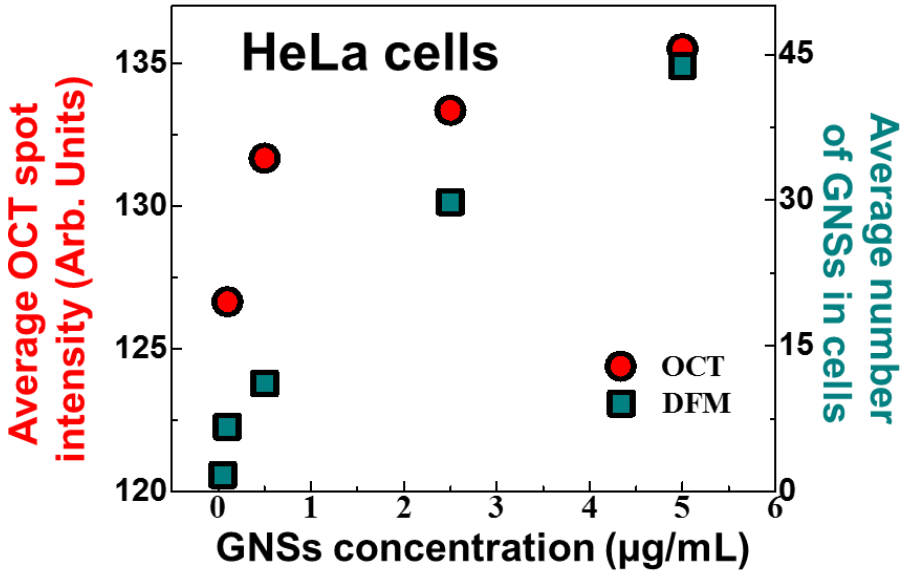


**Figure 5.7** Average OCT spot intensities and number of GNSs in cells generated from HeLa cells incubated with various concentrations of GNSs for a fixed time of 24 h. The average OCT spot signal was calculated from the frequency distribution signals for spot intensities above a threshold intensity of 120 $u_{arb}$ (IV-OCT signal of successfully incubated cells), the number of GNSs in cells were calculated from DFM images.

### 1.4. Contrast enhancement at cellular and tissue level

Finally, it should be noted that the unequivocal relation between OCT spots with intensities larger than 120 uarb and GNS internalization in cells allows for not only detailed studies of the incubation efficiency, but also for the three-dimensional localization of cells with GNSs in their cytoplasm. An example of this imaging capacity is given in **Figure 5.8**. In **Figure 5.8** (a)**,** the raw IV-OCT image of a suspension of HeLa cells after incubation for 24 h with 2.5 µg/mL of GNSs is shown. The IV-OCT raw image shows a large density of spots with a wide variety of intensities ranging from 40 to 180 $u_{arb}$. As discussed above, these spots reveal a high density of GNSs, suspended HeLa cells and suspended HeLa cells that have internalized GNSs. In order to isolate the images of HeLa cells that have internalized GNSs efficiently, the raw IV-OCT images were treated by filtering the spots above a single threshold level. **Figure 5.8 (b)** shows filtered the IV-OCT image corresponding to the data shown in **Figure 5.8 (a)** after removing the OCT spots with intensities below 120 $u_{arb}$. Since OCT intensities above 120 $u_{arb}$ are only generated by HeLa cells

with internalized GNSs, **Figure 5.8 (b)** corresponds to an image of the sub-population of HeLa cells containing GNSs (they have been labeled in green color). Therefore, IV-OCT could be used for molecular imaging of internalized cells. As explained in the **Experimental techniques** section, the clinical IV-OCT system could also be used for three-dimensional imaging by pulling back the catheter. This possibility, together with the threshold level filtering, was exploited to obtain a three-dimensional image of the sub-population of HeLa cells with internalized GNSs. The pull back video was imported to ImageJ program, after setting a threshold level filtering, HeLa cells with internalized GNSs were distinguished, and then their coordinates (*x*, *y*, *z*) were saved and imported to the Origin program. The three dimensional image was drawn by means of 3D scatter program. Thus, the three dimensional image of the sub-population of HeLa cells with internalized GNSs is shown in **Figure 5.8 (c)**. The red spots correspond to HeLa cells with internalized GNSs, the coordinates *x* and *y* correspond to the position of HeLa cells in the OCT cross-sectional image, and *z* coordinate is obtained from the OCT video (540 slices correspond to 54 mm of the pull back distance). This result indicates the possibility of real-time, three-dimensional tracking of living cells in the intravascular system by employing specifically targeted GNSs.

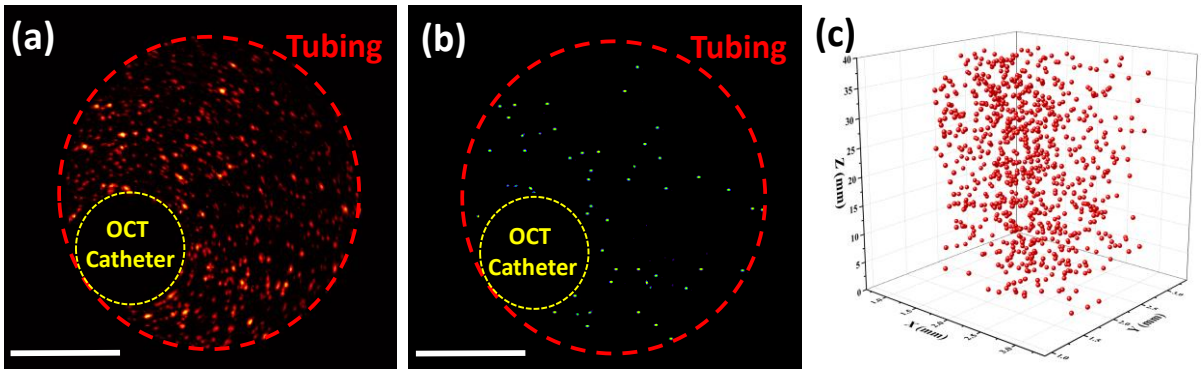


**Figure 5.8 (a)** Raw cross-sectional IV-OCT image of a suspension of HeLa cells after incubation with GNSs for 24 h. The concentration of GNSs in the culture medium during incubation was 2.5 μg/mL. **(b)** IV-OCT cross-sectional image of the same cell suspension used in **(a)**, but after applying a threshold filtering to the raw image. The intensity threshold was set to 120 $u_{arb}$, so that observed spots correspond to HeLa cells that internalized GNSs. **(c)** Three-dimensional IV-OCT image of the suspended HeLa cells that internalized GNSs. Each pixel providing a IV-OCT signal larger than 120 $u_{arb}$ was identified as a single HeLa cell with internalized GNSs. Scale bar represents 1 mm.

As mentioned above, many clinical applications also require contrast enhancement within tissues. In order to demonstrate the potential application of GNSs to enhance the OCT contrast inside a tissue, a final experiment was designed in which the IV-OCT catheter was positioned inside a muscular tissue (*Gallus gallus domesticus*). Then, two injections (0.5 mL per injection) of an aqueous solution of GNSs (50 µg/mL) were performed in the proximity of the OCT catheter (see **Figure 5.9 (a)**). The cross-sectional images of the muscular tissue obtained before and after the injection of GNSs are shown in **Figure 5.9 (a) and (b)**. The circle in the center of the image corresponds to the catheter. The red yellow area around the IV-OCT catheter is due to the backscattered light produced by the tissue and the GNSs. According to the optical scattering properties of soft tissues reported by Joseph,[192] tissues show a high scattering coefficient from 600 to 1400 nm, and so giving a high OCT intensity around the catheter. In addition, the OCT intensity decreases from the OCT catheter to deeper tissue. A detailed comparison of these figures reveals a contrast enhancement at the injection locations. This is clearly manifested in **Figure 5.9 (c)**, which includes the average OCT intensity ($I_{OCT}$) against depth profiles obtained along the scan direction represented by the green arrows in **Figure 5.9 (a)** and **(b)**, i.e., along two scan directions crossing the GNS injection areas. **Figure 5.9 (c)** clearly demonstrates that OCT intensity decrease as function of the depth due to the scattering and absorption properties of the tissue. In addition, the presence of GNSs leads to an OCT contrast enhancement between 0.8 and 1.6 mm, in good agreement with the location of the injected GNSs. This result is more clearly observed when the OCT depth profile obtained prior to the injection is subtracted from the profile obtained after injection ($\Delta I_{OCT}$), shown in **Figure 5.9 (d)**. This figure shows the relevant enhancement in the OCT contrast produced by the GNSs inside the tissue. Indeed the distribution of GNSs as function of depth can be observed. Thus, the data included in **Figure 5.9** clearly demonstrate the potential use of GNSs as contrast agents for OCT imaging of tissues using cardiovascular clinical systems.

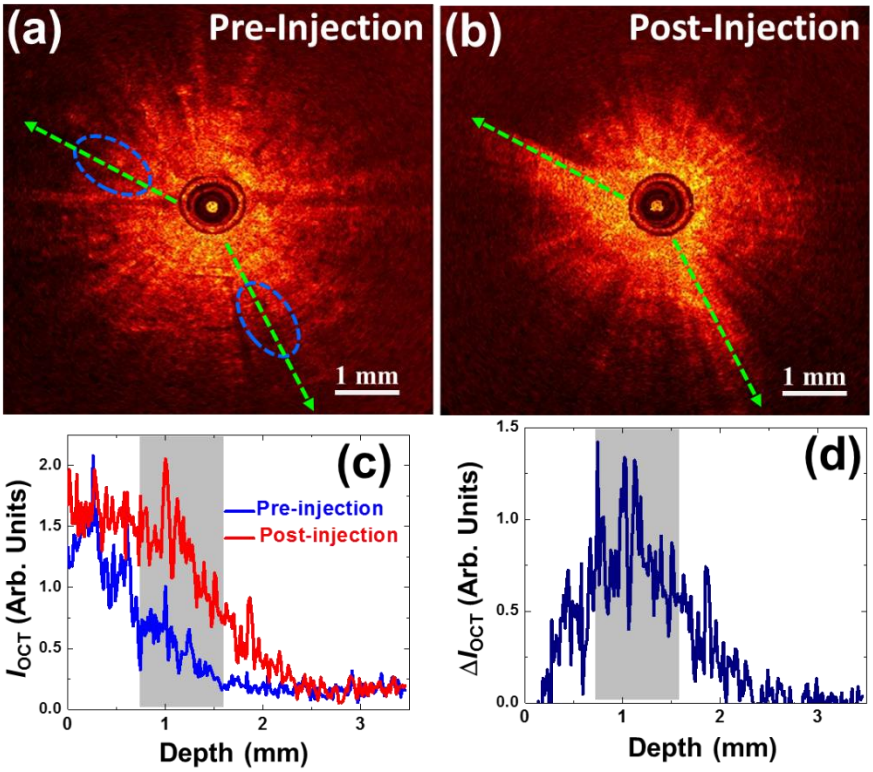


**Figure 5.9 (a)** Cross-sectional OCT image of a tissue prior to the injection of GNSs. An aqueous solution of GNSs (0.5 mL; 50 µg/mL) was injected in the areas delimited by the blue dashed lines. **(b)** Cross-sectional OCT image of the same tissue shown in **(a)** after the injection of an aqueous solution of GNSs. **(c)** OCT intensity ($I_{OCT}$) versus depth in the tissue, as obtained along the scan lines, is indicated by the green arrows in **(a)** and **(b)**. **(d)** Difference between the OCT intensity obtained prior to and after the injection of GNSs ($\Delta I_{OCT}$) as a function of the penetration depth in the tissue. The spatial extension of the GNSs within the tissue is indicated by the gray areas included in **(c)** and **(d)**.

## 1.5. Internalization of GNSs in HMEC-1 cells under flow conditions

HMEC-1 is a human microvascular endothelial cell line, and the dysfunction of this cell line related to cardiovascular disease. Evaluation of internalization of GNSs in HMEC-1 under flow conditions is a very important step for clinical application of GNSs in cardiovascular disease. Therefore, I have settled a flow setup as described in **Experimental techniques**. Due to the limited time of project, the functionalization of GNSs is not available. In this case, commercial GNSs coated with PEG without functionalization and HMEC-1 without activated were used to evaluate the flow system. The DFM images (taken by EMCCD camera) of GNSs and HEMC-1 at different

flow times are shown in **Figure 5.10**. The morphology of HEMC-1 can be clearly seen. The movement of GNSs 1 and 2 can be tracked as labeled by red arrows. The internalization of GNSs in HEMC-1 haven't been found due to the non-specific functionalized of GNSs and non-activated HEMC-1. More work needed to be done in order to see in the internalization of GNSs in HEMC-1 under flow condition.

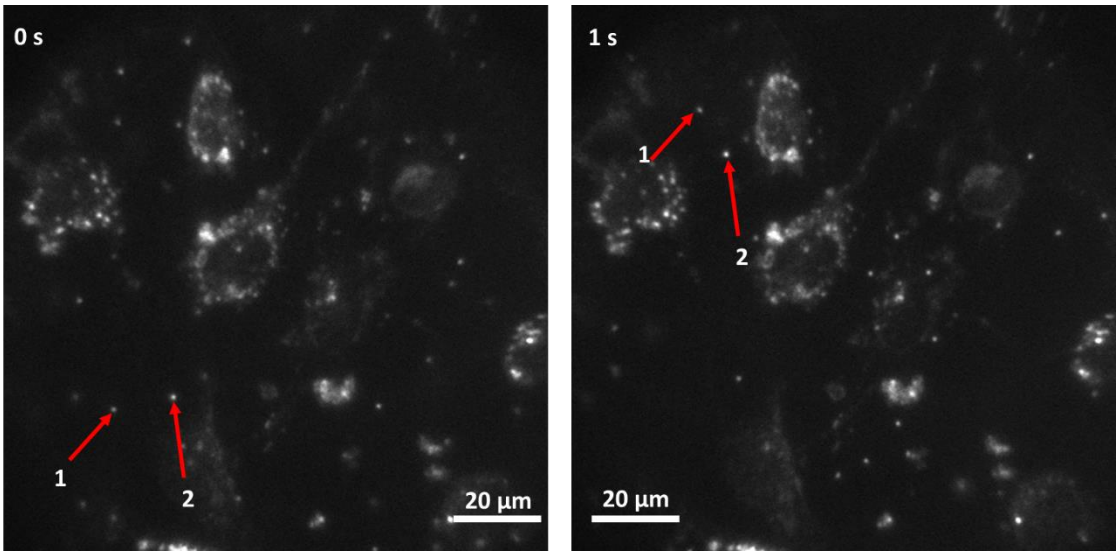


**Figure 5.10** DFM images of GNSs and HMEC-1 cells at different flow time (0 s and 1 s). The positions of GNSs 1 and 2 at different flow time were labeled by red arrows.

## 1.6. Conclusions

In summary, in this chapter, I have shown how clinical IV-OCT allows for the detection of individual cells suspended in biological fluid. The experimental results indicated that the backscattering contrast of individual cells could be substantially enhanced by the intracellular incorporation of specifically designed GNSs with high scattering cross-sections at the IV-OCT operating wavelength (1320 nm). A detailed intensity analysis of IV-OCT images enabled the identification and discrimination of different sub-populations within a suspension of living cells. In particular, an analysis of the intensity histograms from IV-OCT images allowed for the detection of living cells in which GNSs attachment occurred, and made it possible to estimate the attachment efficiency and its relationship to the concentration of GNSs in the culture medium. These results were in excellent agreement with those obtained using alternative techniques, such as DFM and

TEM. Finally, the tissue contrast enhancement by OCT, achieved after the injection of GNSs inside the tissue was demonstrated.

As GNSs are easy to functionalize with biomolecules to target specific cell sites, the results of this study provide a new path for reliable molecular imaging by IV-OCT, and thus constitute the first step towards the development of new diagnostic procedures at the clinical level.

# Chapter 6. PbS QDs as contrast agents for cardiovascular bimodal imaging

## 6.1. Introduction

Up to now, silica-coated gold nano-shells with plasmon resonance close to the IV-OCT laser wavelength (1.3 μm) and high back-scattering cross sections were demonstrated as the best nano-contrast agents, showing significant IV-OCT contrast enhancements in suspensions and tissues.[179] In addition, these nanoparticles have been used for OCT molecular imaging of several cell lines.[193] The potential application of OCT contrast agents would further benefit if the NPs, in addition to the OCT contrast enhancement, could provide simultaneous photoluminescence (PL) contrast. This would open the possibility of achieving multimodal intracoronary imaging that would be immensely helpful, for instance, in the understanding of the relation between atherosclerotic plaque microstructures and the molecular mechanisms that underlie their formation and instability, leading to acute coronary syndromes.[194] A pioneering work of H. Yoo and co-workers[60] demonstrated that the simultaneous acquisition of multimodal OCT+(PL) intracoronary images allowed for microstructural and molecular functional image, an essential information to the correlation of coronary artery disease and vessel wall healing. These authors used the Cy7 fluorophore to provide fluorescence imaging while intracoronary OCT images were constructed from the inherent contrast provided by the artery.[195, 196] However, this approach implied the use of two laser sources (one to excite the fluorophore and the other for OCT),[60] increasing the complexity of the experimental arrangement. Solving this drawback implies the use of a contrast agent capable of providing both luminescence and back-scattering contrast just under single laser excitation at 1.3 μm. Furthermore, if a NP is to be used as a multimodal OCT+PL agent in cardiological applications, its luminescence should be produced within the so-called infrared biological windows,[51] where human tissues become partially transparent allowing high penetration in *in vivo* fluorescence imaging.[197-199] In, addition, NPs is much more stable than the fluorophores and doesn't have photobleach.[53]

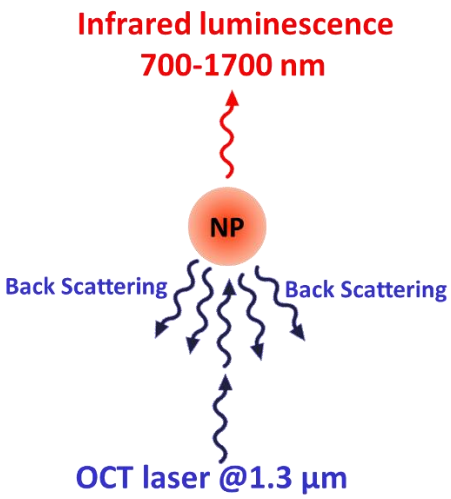


**Figure 6.1** Schematic representation of a NP capable of OCT+PL imaging under single laser line excitation at 1.3 µm.

In this chapter, the potential use of Infrared emitting Quantum Dots (IR-QDs) as OCT+PL multimodal intracoronary imaging agents under single line laser excitation was evaluated. The operating scheme is shown in **Figure 6.1.** Thus under OCT laser excitation, the IR-QDs can scatter the OCT laser light, the backscatter light can be collected by the IV-OCT catheter, and thus produces OCT signal. In addition, the IR emission of QDs can be generated under OCT laser excitation, and thus the fluorescence image produced by the IR-QDs can be obtained by using a near infrared camera. The simultaneous capacity of these dots for back-scattering and fluorescence generation in III-BW[52] under single 1.3 µm laser excitation was evaluated in aqueous suspensions, tissues and *ex vivo* aorta by using an IV-OCT clinical equipment.

## 6.2. Characterization of PbS QDs

The IR-QDs used all along this work were PbS QDs (CANdots® Series C with a nominal emission wavelength of 1600 nm), and they were surface-functionalized with a PEG-ligand (DSPE-PEG-amine) in order to achieve dispersability in water. A carton of PbS QDs with PEG is drawn in **Figure 6.2**. Details of surface functionalization can be found in the **Experimental techniques** section. A representative TEM image of the IR-QDs is shown as **Figure 6.2 (a)**. Statistical analysis of this and other TEM images reveals an average IR-QD size of 5.4 nm, with a size dispersion of ±2.3 nm, as can be appreciated from the size histogram included as an inset in

**Figure 6.2 (a)**. Therefore, taking into account the density of PbS (7.6 mg/cm$^3$) and the volume of each PbS QDs is $(4/3)\times\pi\times(2.7\times10^{-7})^3$ cm$^3$, the number of QDs per mL for initial content (0.6 mg/mL) is $9.21\times10^{17}$ NPs/mL. **Figure 6.2 (b)** shows the room temperature extinction cross section together with the emission spectrum of the IR-QDs. The extinction cross section clearly evidences the first exciton absorption peak at around 1420 nm. The non-negligible extinction at the OCT laser wavelength peak (also included in this figure) should also be noted. The OCT laser spectrum matches the extinction spectrum, and therefore, the PbS QDs can be excited by using a IV-OCT laser. The emission spectrum of IR-QDs is constituted by a single broad band centered at around 1.55 µm (III-BW), so that it can be easily spectrally isolated from the IV-OCT laser radiation by using long pass filters.

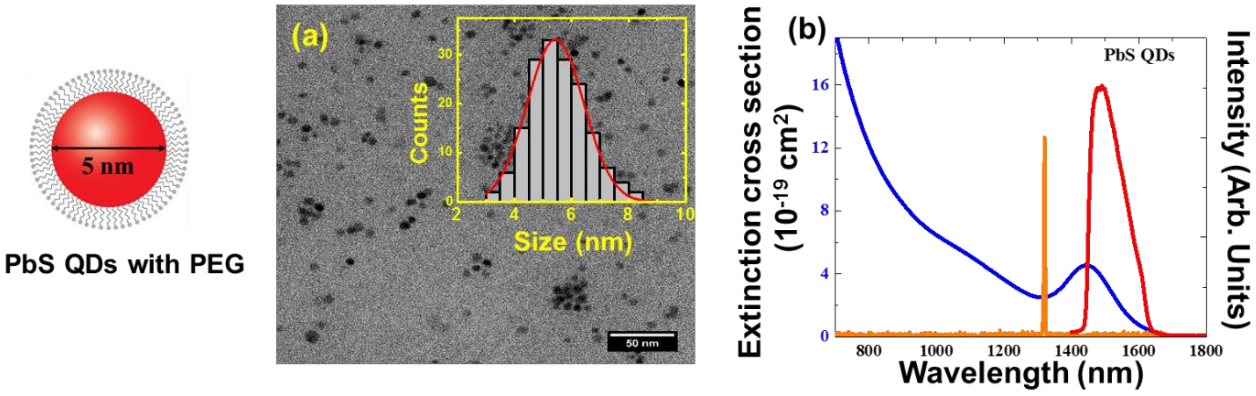


**Figure 6.2 (a)** Characteristic TEM image of the QDs used in this work. Inset shows the size histogram revealing an average size close to 5 nm. **(b)** Blue line corresponds to the extinction cross section of the QDs (Commercial PbS QDs without surface modification, the concentration of PbS is 10 mg/mL). The emission spectrum of the QDs is also included (red line). The orange line corresponds to the spectral distribution of the laser radiation generated by the IV-OCT catheter.

## 6.3. Bimodal OCT and fluorescence imaging of colloidal QDs

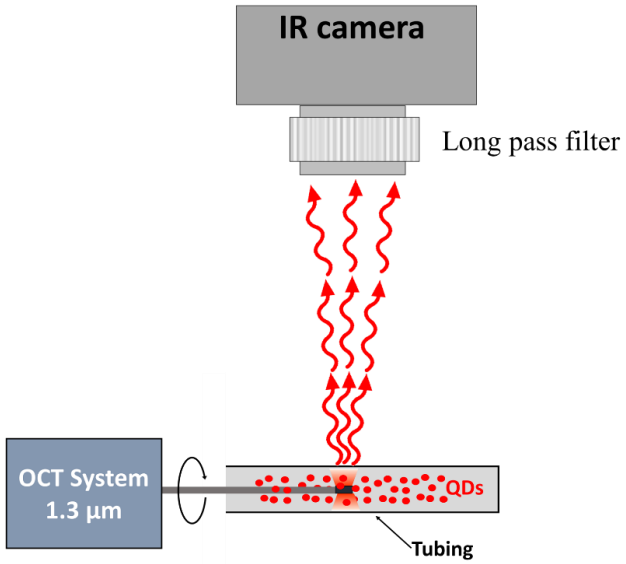


**Figure 6.3** Schematic representation of the experimental approaches used to test the capacity of IR-QDs for multimodal OCT+PL imaging in a fluid.

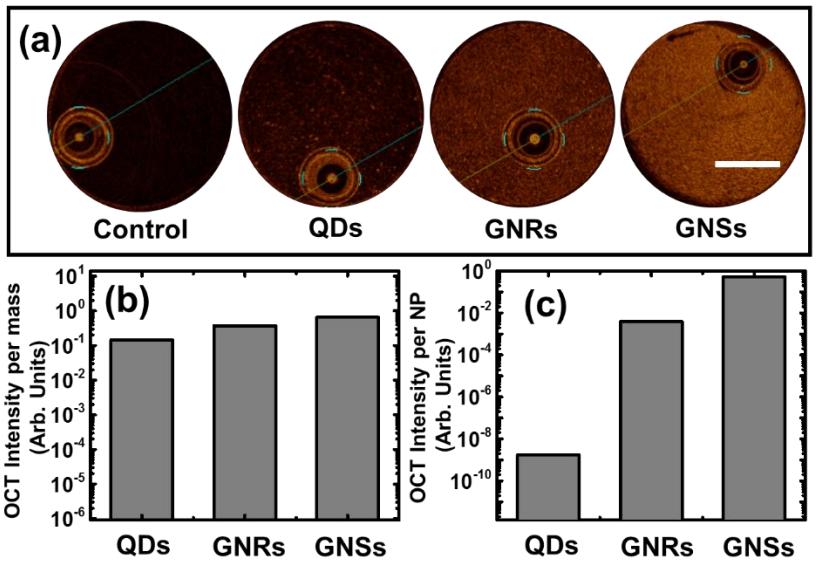


**Figure 6.4 (a)** Cross-sectional OCT images of the tubing in the presence of three aqueous solutions of IR-QDs, GNRs and GNSs. The cross sectional image in absence of any NPs is also included as "control image". Scale bar, 1 mm. **(b)** Integrated OCT intensity normalized by the total mass of NPs as obtained for IR-QDs, GNRs and GNSs. **(c)** Integrated OCT intensity normalized by the total number of NPs as obtained for IR-QDs, GNRs and GNSs.

The experimental arrangement depicted in **Figure 6.3** is used to evaluate the bimodal OCT+PL imaging of colloidal QDs introduced in a tubing (simulating an artery). The IR-QDs were injected in the tubing in which contains the IV-OCT catheter, the static OCT was operated to evaluate the OCT contrast produced by the IR-QDs. **Figure 6.4 (a)**, left side, shows the IV-OCT cross sectional image when the tubing was filled with a clean suspension of water, which was used as a control image for IV-OCT experiments. The cross sectional IV-OCT image obtained when the tubing was filled with an aqueous suspension of IR-QDs (0.06 mg/mL) is also included in **Figure 6.4 (a)**. The contrast enhancement produced by the suspended IR-QDs is clearly evidenced. This fact unequivocally reveals the capacity of individual IR-QDs (in spite of their small sizes) to backscatter the 1.3 μm OCT laser radiation. The scattering properties of QDs in the visible domain were already theoretically postulated and experimentally evidenced by dark field microscopy previously.[200] Nevertheless, this is the first time that such scattering ability is demonstrated in the infrared spectral region, and particularly under the IV-OCT excitation conditions. In order to compare the IV-OCT enhancement produced by IR-QDs in respect to that provided by metallic nanoparticles**, Figure 6.4 (a)** also includes cross sectional images obtained when the tubing was filled with an aqueous suspensions of GNPs. Two types of GNPs have been used here for comparison. GNRs (100 nm length and 10 nm width) with a plasmon resonance wavelength peak close to 1300 nm and GNSs (198 nm core and 16 nm shell) with a multimodal plasmonic band extending from 800 up to 1800 nm. Concentrations of the solutions of both GNRs and GNSs were 0.06 mg/mL. **Figure 6.4 (b)** shows the IV-OCT signal enhancement (in respect to the control) normalized by the mass of contrast agents, as obtained for the three particles investigated. **Figure 6.4 (b)** reveals that, for similar concentrations, IR-QDs show an IV-OCT contrast per mass unit enhancement smaller but comparable to that provided by GNPs. **Figure 6.4 (c)** shows the IV-OCT integrated intensity normalized to the number of particles. In this case, it is clear that the IV-OCT intensity generated by a single metallic nanoparticle is more than eight orders of magnitude larger than that provided by individual IR-QDs. Indeed, this was expected because of two main reasons. The first one is the large size difference: the volume of an individual GNS is more than four orders of magnitude larger than the volume of an individual IR-QDs. Secondly, for metallic nanoparticles the back-scattering is associated with the collective resonant excitations of charges (plasmon resonance overlaps with the IV-OCT laser radiation).[148, 201] As a consequence, the back-scattering cross section of, for instance, GNSs with enough plasmon resonance at OCT laser wavelength are

as large as $7\times10^{-11}$ $cm^2$ per nanoparticle.[179] The scattering cross section of IR-QDs has not been reported up to now, but theoretical studies predict that the scattering cross section of individual QDs is much smaller than the absorption cross section.[202] This applies when the QD's size is much smaller than the wavelength of the incident light, as it occurs in this work. The extinction cross section at 1.3 μm of our IR-QDs has been estimated to be close to $2.5\times10^{-19}$ $cm^2$.[203] This is, indeed, eight orders of magnitude smaller than the scattering cross section of GNSs, in good accordance with the eight orders of magnitude differences experimentally obtained between the IV-OCT intensity provided by individual IR-QDs ($1.8\times10^{-16}$) and individual GNSs ($5.4\times10^{-8}$) (see **Figure 6.4 (c)**). Despite the reduced IV-OCT signal, it is important to remark that the contrast generated by individual IR-QDs, although much weaker than that provided by individual metallic nanoparticles, is still well measurable by the clinical IV-OCT system.[21]

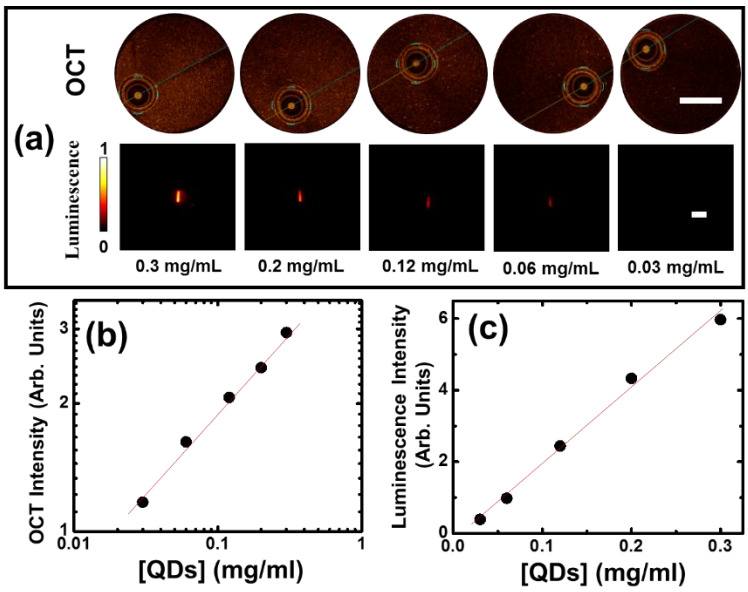


**Figure 6.5 (a)** Cross sectional OCT and infrared as obtained for different concentrations of IR-QDs in the tubing. Scale bar, 1 mm. **(b)** Integrated OCT intensity as a function of the concentration of IR-QDs. Scale bar, 4 mm. **(c)** Integrated infrared luminescence intensity as a function of the concentration of IR-QDs. In **(b)** and **(c)** dots are experimental data and solid line is a guide for the eyes.

Once the capacity of IR-QDs for providing IV-OCT contrast has been demonstrated, their ability to simultaneously produce PL contrast was evaluated by using an infrared fluorescence camera to image the tubing (see **Figure 6.3**). The infrared fluorescence camera was set above the tubing to take the infrared image, meanwhile, a long pass filter 1350 nm was put before the camera to

remove the OCT laser signal. The obtained infrared fluorescence images of a tubing filled with aqueous suspensions of IR-QDs at different concentrations are shown in **Figure 6.5 (a)**, from which the presence of IR-QDs is evidenced. This indicates efficient absorption and re-emission of the 1.3 μm OCT laser radiation by IR-QDs. At this point, it is important to remark that the data included in **Figure 6.4** and **Figure 6.5 (a)** clearly demonstrate the ability of our IR-QDs to produce, simultaneously, IV-OCT and IR luminescence images, all under just the single laser line excitation of the cardiovascular OCT system. The dependences of both integrated OCT and luminescence intensities ($I_{OCT}$ and $I_{lum}$, respectively) on the concentration of IR-QDs are shown in **Figure 6.5 (b)** and **(c)**. In both cases the integrated intensities increase monotonously with the IR-QD concentration, but with very different trends. On one hand, the IV-OCT intensity vs the IR-QDs' concentration shows a linear dependence in a Log-Log representation. This implies that the IV-OCT intensity ($I_{OCT}$) can be written as $I_{OCT} = [QDs]^n$, where $[QDs]$ is the concentration of IR-QDs. Linear fitting of experimental data in the Log-Log representation provides, for this particular case, a value of $n = 0.3$, so that the IV-OCT intensity increases with the concentration of IR-QDs following a sublinear trend. The reason explaining this sublinear trend is not clear at this point. Nevertheless it should be mentioned here that a similar trend was also observed for metallic nanoparticles,[179] so that it is likely that the sublinearity is related to the way in which the processing and quantification of IV-OCT images are performed by the clinical equipment. On the other hand, the luminescence intensity generated by IR-QDs (when optically excited with the IV-OCT laser) was found to follow a linear trend with the concentration of IR-QDs (see **Figure 6.5 (c)**), as it was indeed expected. This opens the door to straightforward determination and quantification of intracoronary accumulation of QDs by just monitoring the infrared luminescence generated from the analyzed arteria under excitation with the IV-OCT catheter.

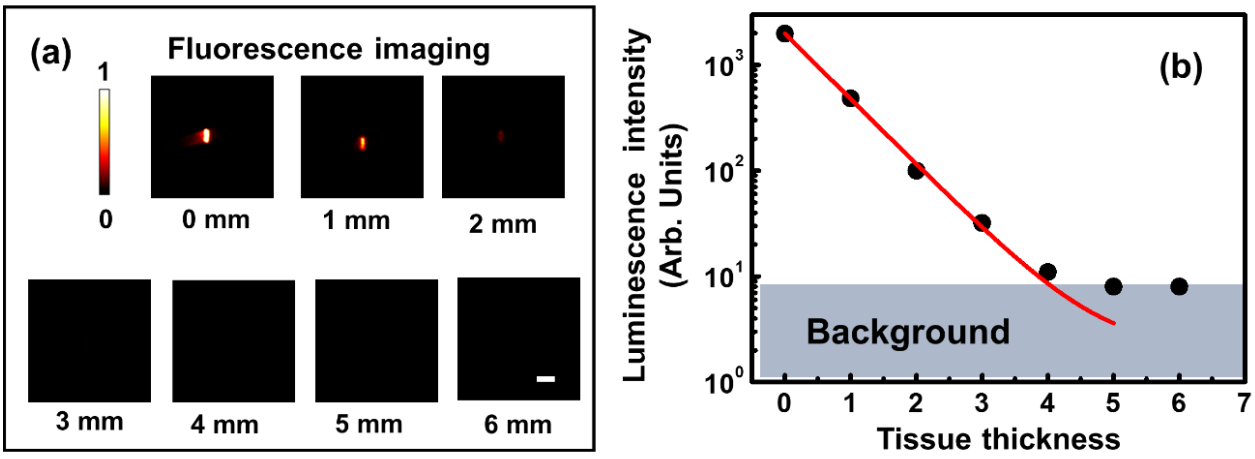


**Figure 6.6 (a)** Infrared fluorescence images of a catheter filled with an IR-QD suspension (0.6 mg/mL) as obtained for different tissue thickness. Scale bar, 4 mm. **(b)** Integrated infrared luminescence intensity as a function of the tissue thickness. Dots are experimental data obtained from the luminescence images in **(a)** and the red line is the best fit to an exponential decay. The penetration length provided by exponential fit is 0.8 mm.

The potential application of infrared fluorescence imaging for sub-tissue localization of QDs in arteries would be determined by the effective penetration length (under excitation with the IV-OCT catheter). In order to evaluate this important aspect, different thickness of the tissues varing from 0 up to 6 mm, were set above the tubing. Then the fluorescence images generated by the IV-OCT catheter from a tubing filled a QDs/water solution were obtained for different tissue thickness by the IR camera as shown in **Figure 6.6 (a)**, the fluorescence intensity decreases when increasing the tissue thickness, and the fluorescence image is almost invisible when the tissue thickness reached 3mm. The integrated fluorescence intensity ($I_{lum}$) as a function of the tissue thickness ($d$) is shown in **Figure 6.6 (b)**. According to previous stablished models of light propagation in tissues, the fluorescence intensity should follow a typical trend given by:

$$I_{lum} = I_0 exp[-d/l_p] \tag{6.1}$$

where $I_0$ is a constant and $l_p$ is the so-called optical penetration length. Experimental data fit well to this trend, providing an optical penetration length close to 0.8 mm. Indeed, this is quite close to the optical penetration lengths reported for different infrared emitting luminescence probes that

have been successfully used for high penetration and high resolution "*in vivo*" imaging.[204-206] Note that the maximum depth at which IR-QDs can be detected depends on the background level of the IR camera. In comparison to our camera, working at 0 ºC, the use of an IR camera working at -80 ºC (operating temperature of double Peltier cooled commercial cameras) would lead to a reduction in the background signal of more than one order of magnitude, and so making possible to detect IR-QDs at subcutaneous depths well in excess of 1 cm.

At this point it should be mentioned that future optimization of the fluorescence and the scattering efficiencies of a nanostructure for bimodal OCT+PL imaging is not an easy task as they are exclusive processes. In fact, if a nanoparticle shows high scattering cross sections, then the amount of absorbed light (that determines the fluorescence intensity) will be reduced. Thus, a compromise has to be reached. Such compromise could be obtained in the future by using hybrid nanostructures combining, into a single unit, highly scattering units and bright fluorescent units. This could also be achieved through core/shell engineering (by creating a thin metallic shell on the surface of IR-QDs) or, alternatively, by linking IR-QDs and metallic nanoparticles through surface modification. In addition, I would also like to note that, with the experimental data available now, I cannot disregard the contribution of absorption-reemission of pump photons to the overall back-scattering signal. Nevertheless, I consider that it would be a second order process when compared with the direct backscattering due to photon backscattering at the surface of IR-QDs. Furthermore, even in the case that these processes were taking place, they would not contribute to the observed OCT contrast due to the lack of coherence between pump and backscattered light.

## 6.4. OCT and fluorescence bimodal imaging in tissues

As commented in the introduction, one of the advantages of IV-OCT is its capacity to provide, in addition to a topographical image of an artery, information about tissue properties beyond the artery wall. Thus, a multimodal OCT+IR probe should be able not only to provide dual contrast when being in suspension (inside the artery) but it should also be capable of dual contrast when being located inside a tissue.[60, 106, 207] The ability of our IR-QDs for OCT+PL dual contrast imaging in tissues was, therefore, also explored.

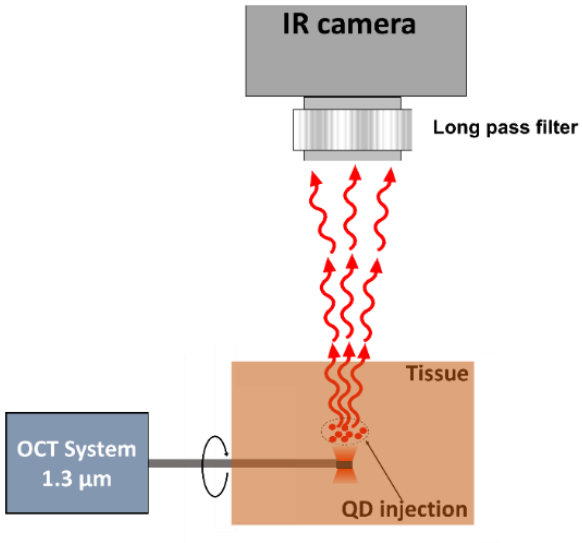


**Figure 6.7** Schematic representation of the experimental approaches used to test the capacity of IR-QDs for multimodal OCT+PL imaging in a fluid.

The experimental approach for dual contrast imaging in tissue is schematically drawn in **Figure 6.7**. Instead of using the tubing (see **Figure 6.3**), a muscular tissue was used. The IR-QDs were injected in the tissue but near the IV-OCT catheter in order to detect the OCT contrast enhancement in tissue produced by the IR-QDs and at the same time, making an efficient excitation of the IR-QDs by the OCT laser. A cross sectional IV-OCT image of the tissue before the QDs' injection is shown in **Figure 6.8 (a)**. It is constituted by a diffuse background, associated to the characteristic inhomogeneous refractive index of tissues. **Figure 6.8 (c)** shows the corresponding infrared fluorescence image of the tissue, demonstrating, as expected, no contrast at all. Indeed, this result indicates the negligible excitation of tissue auto-fluorescence by the 1.3 µm OCT laser. When IR-QDs were injected into the tissue both OCT and luminescence images change appreciably in the injection area in respect to the control (no IR-QDs). **Figure 6.8 (b)** shows the cross sectional OCT image of the tissue after the injection of 200 µL of an aqueous suspension of IR-QDs (0.6 mg/mL). The location of the injected IR-QDs is indicated by a red arrow. The presence of IR-QDs in the tissue is observed by a clear increment in the OCT intensity. This is further evidenced in **Figure 6.8 (e)** in which the OCT signal profile (obtained inside the tissue along the scan direction represented by the yellow arrows in **Figure 6.8 (a)** and **(b)**) was included. Comparison between the OCT intensity profiles obtained, before and after injection, clearly demonstrates a remarkable intensity enhancement at the location of the IR-QDs. Indeed, the OCT signal was increased by

almost 2.5 times due to the IR-QD induced backscattering. At the same time, the presence of IR-QDs was simultaneously monitored by their infrared luminescence, as it is demonstrated in the infrared fluorescence image included as **Figure 6.8 (d)**. Thus, the ability of IR-QDs for dual OCT+PL and fluorescence imaging inside tissues is clearly proved. This multimodal imaging capacity appears of special relevance for cardiovascular imaging, as it would allow for unequivocal identification of inner lesions beyond the artery contour by using adequately functionalized IR-QDs.

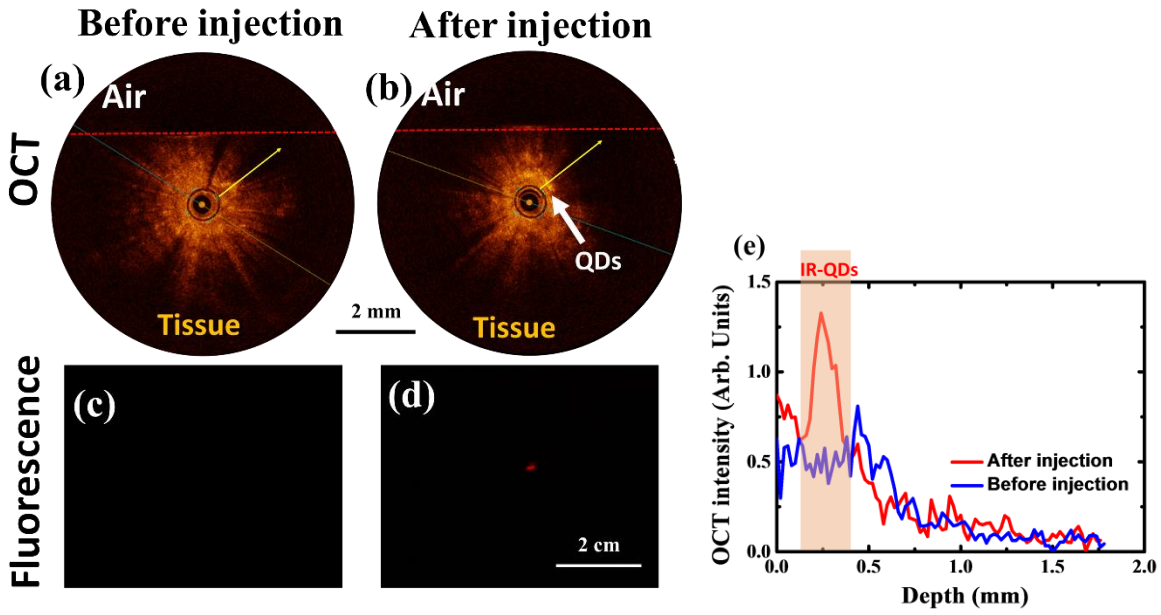


**Figure 6.8 (a)** Cross-sectional OCT image of a tissue before the injection of IR-QDs. Scale bar, 1 mm. **(b)** Cross-sectional image of the same tissue after the injection of IR-QDs. The location of the IR-QDs is indicated by the red arrow. The dashed red line indicates the position of the tissue-air interface. **(c)** Infrared fluorescence image of the tissue prior to the injection of IR-QDs. **(d)** Infrared fluorescence image of the tissue after the injection of IR-QDs. Scale bar, 4 mm. **(e)** OCT intensity profile as obtained along the yellow arrows indicated in **(a)** and **(b)**. Data obtained before and after injection are included denoting the enhancement in the OCT signal due to the presence of IR-QDs.

## 6.5. OCT and fluorescence bimodal imaging in rabbit artery

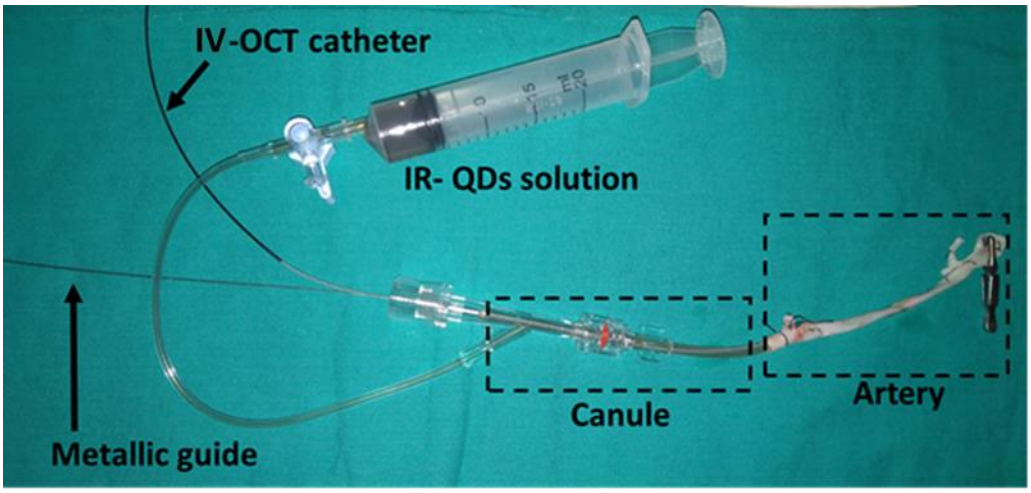


**Figure 6.9** shows an optical picture of the experimental set-up used for multimodal OCT+PL imaging of an artery excised from a rabbit. The different parts are indicated and labelled.

In order to finally test the potential application of our IR-QDs for multimodal cardiovascular imaging, *ex vivo* experiments were conducted. The aorta of a rabbit (whose dimensions are similar to human coronary arteries) was excised from a sacrificed rabbit. The branches were sealed by suture procedures and the IV-OCT catheter was introduced in the artery by using a cannula and metallic guide. Details about the experimental procedure can be found in **Figure 6.9**. The IR-QDs were injected in the artery by using a syringe, which connects to the cannula by a tubing. The IV-OCT catheter was introduced and was scanned along the artery with a speed of 10 mm/s. During the scanning of the IV-OCT catheter the fluorescence generated by the IR-QDs in the artery was detected by the same InGaAs infrared camera used in previous experiments. This simple experimental set-up made possible the simultaneous acquisition of the OCT and infrared fluorescence images of the artery in real time.

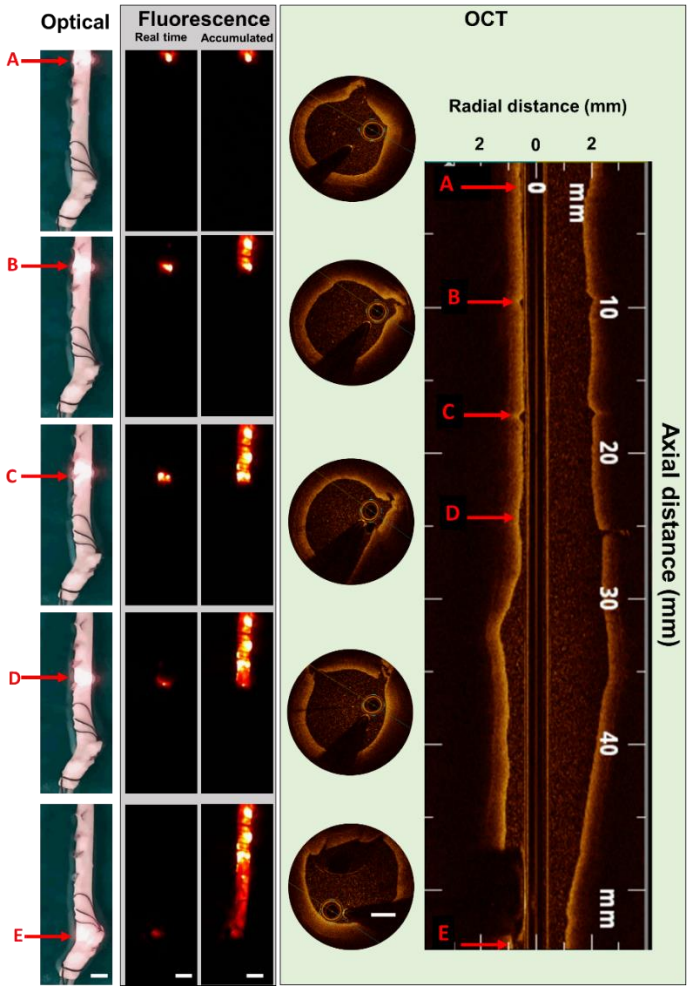


**Figure 6.10** Optical image of the aorta excised from a sacrificed rabbit. The position of the IV-OCT catheter during axial scanning is indicated by red arrow. The instantaneous (real time) and accumulative infrared fluorescence image generated by the IR-QDs inside the artery are also shown for the different positions of the IR-OCT catheter and named A, B, C, D and E. The corresponding OCT cross sectional images are also displayed together with the transverse OCT image of the artery. The shadow in OCT cross section images are due to the light blocked by the metallic guide. The scale bar for optical and fluorescence image is 4 mm, for OCT cross section image is 1 mm.

**Figure 6.10** shows the optical image of the rabbit aorta at different times during the IV-OCT scanning. The position of the OCT catheter at each time, which it is indicated by an arrow, can be elucidated thanks to a red laser (at 650 nm) that is integrated into the rotating fiber. The real time and accumulative fluorescence images obtained at different times are also included in **Figure 6.10**. In addition, for the sake of clarify, the accumulated fluorescence image are also include in this

figure. The fluorescence images are due to the emission of PbS QDs under excitation of IV-OCT catheter. IV-OCT cross-sectional images of the artery were simultaneously acquired, five representative OCT cross sectional images obtained at the different artery positions (indicated by A, B, C, D, E arrows) are also included in **Figure 6.10**. The shadow in the OCT cross section images are due to the OCT laser light blocked by the metallic guide. The OCT contrast in the artery indicated the existence of IR-QDs in the artery. In addition, an axial OCT image of the artery, which was obtained after the IV-OCT scanned the artery from 0 to 54 mm was included in **Figure 6.10**. This image shows the morphology of the artery used in this experiment, the indentations in the artery (as indicated by A, B, C, and D arrows) are supposed to help the accumulation of the IR-QDs in the artery. A video of the measuring process in which the translation of the IV-OCT and the simultaneous acquisition of fluorescence image can be found online

(https://drive.google.com/file/d/0B5z1PgUYHn1eaTV1b08zUjRrMGM/view?usp=sharing).

The fluorescence images clearly demonstrate how the PL generated by the IR-QDs inside the artery accurately reproduces its morphology. In addition, several bright spots (Indicated by A, B, C and D arrows) are observed, revealing the accumulation of IR-QDs inside the artery. When these images are compared with the OCT ones, it is possible to correlate these bright spots with the localization of the arterial branches that were clamped. This is evidenced by arrows in the OCT longitudinal image of the artery. Thus, I state that at these positions IR-QDs are accumulated. The experiments included in **Figure 6.10**, do not only reveal the potential use of IR-QDs for multimodal cardiovascular imaging, but also demonstrate that the synergy between fluorescence and OCT cardiovascular imaging could result in the appearance of advanced imaging and diagnosis tools.

## 6.6. Conclusions

In this section the capability of semiconductor quantum dots, emitting in the third biological window, for multimodal cardiovascular imaging has been demonstrated. Infrared emitting quantum dots were shown to be capable of providing simultaneous contrast in intracoronary optical coherence tomography and infrared fluorescence imaging all under 1.3 μm wavelength single beam laser excitation provided by a clinical catheter. It is demonstrated that , when a single infrared emitting quantum dot is optically excited by a 1.3 μm wavelength photon, the back-scattered

radiation is strong enough to produce a measurable contrast by a clinical OCT system. At the same time, the absorbed photons are efficiently re-emitted at 1.55 μm, making possible their simultaneous localization by fluorescence imaging. Dual fluorescence and optical coherence tomography imaging was demonstrated both in colloidal suspension and in tissues. Furthermore, a simple "proof of concept" demonstration at the *ex vivo* level showed the real potential of infrared emitting quantum dots for multimodal imaging of arteries, pointing out the synergy between fluorescence imaging and optical coherence tomography.

Consequently, infrared emitting quantum dots appear as the first dual contrast agents for intracoronary imaging based on the use of already established optical coherence tomography catheters. The possibility of acquiring multimodal intracoronary imaging opens a new avenue towards the development of new diagnostic techniques based on multimodal imaging.

# Chapter 7. Conclusions and perspectives

## 7.1. GNSs, best OCT contrast agent

Different kinds of GNPs show different OCT contrast enhancement due to their different scattering properties, as OCT is based on the analysis of backscattered signals. The GNSs with size around 220 nm show a higher scattering cross section at the OCT laser wavelength (1.3 μm) than GNSTs and GNRs, thus the GNSs investigated in my thesis are considered as the best contrast agents for IV-OCT.

## 7.2. Single GNSs visualization by IV-OCT

The IV-OCT can be used to track single GNSs due to the high sensitivity of IV-OCT system and high scattering cross section of GNSs.

## 7.3. GNSs can act as contrast agents for cell imaging and tissue contrast enhancement by IV-OCT

The analysis of the intensity histogram for IV-OCT cross-sectional images of GNSs incubated in the HeLa and Jurkat cells allows the detection of living cells with GNSs attached. The number of detected cells with GNSs by IV-OCT as function of GNSs concentration demonstrated a saturation trend in high GNSs concentration. The internalization of the GNSs in the cells have been confirmed by TEM and DFM.

The injection of GNSs in the tissue near the IV-OCT catheter shows a contrast enhancement, the OCT signal after subtract the background allow visualization of GNSs distribution in the tissue.

## 7.4. PbS QDs could act as a dual contrast for cardiovascular imaging

The broad absorption of PbS QDs allows the excitation of their luminescence by the OCT laser at 1.3 μm. After injection of PbS QDs in artery, their emission around the 1.55 μm after excitation by OCT laser could be used for fluorescence imaging of the artery in the third biological window. In addition, the assignable scattering properties of PbS QDs could be used for OCT contrast enhancement. The PbS QDs are thus promising contrast agents for fluorescence imaging and OCT of cardiovascular disease.

## 7.5. Future perspectives

During the doctoral thesis, the OCT setup has been mainly used for evaluating the potential application of the NPs for cardiovascular imaging. The DFM is home built for visualization of the NPs and cells, and in future, to see the internalized process of NPs in the cells.

In respect to the future work of contrast agent that have been used in my thesis, their basic properties have been demonstrated. The future work would be the functionalization of these contrast agents with special ligand so that they can be specially delivered to the cardiovascular disease sites, and the evaluation of these contrast agents for *ex* and *in vivo* imaging of the atherosclerosis process by OCT, fluorescence, and photoacoustic.

More contrast agent needs to be developed with higher scattering cross section than GNSs. In addition, due to the strong scattering properties of the artery, absorption contrast agents are also needed in order to create negative contrast in the artery, which could decrease the OCT signal and thus indicate the cardiovascular disease sites.

Due to the catheter based IV-OCT system, the functionalized fluorescence NPs could be used in the cardiovascular disease, as the catheter could not only introduce the light to the cardiovascular disease and also collect the light from these areas. Thus the limitation of the fluorescence NPs such as low penetration depth could be avoid. A combined OCT and fluorescence system needed to be widely used for cardiovascular disease research.

# Chapter 8. Conclusiones y Perspectivas futuras (ES)

## 8.1. GNSs, mejor agente de contraste para OCT

Los diferentes tipos de GNPs aumenta de forma distinta el contraste de OCT debido a sus diferentes propiedades de scattering, ya que el OCT se basa en el análisis de la señal de scattering. Los GNSs con un tamaño alrededor de 220 nm muestran una sección eficaz de scattering mayor que la de los GNRs y GNSTs a la longitud de onda del laser del OCT (1,3 μm), así que son los mejores agentes de contraste para OCT entre todas las partículas estudiadas en esta tesis.

## 8.2. Visualización de GNSs individuales por IV-OCT

El IV-OCT puede suarse para seguir GNSs individuales gracias a la alta sensibilidad del IV-OCT y a la alta sección eficaz de scattering de los GNSs.

## 8.3. Las GNSs pueden actuar como agentes de contraste para imagen celular y aumento del contraste en tejidos por IV-OCT

El análisis del hostograma de intensidades de imágenes de OCT de GNSs incubadas en células HeLa y Jurkat permite la detección de células vivas a las que se han adherido GNSs. El número de células adheridas en función de la concentración de GNSs demostró una tendencia a la saturación para dispersiones concentradas de GNSs. La internalización de las GNSs se ha confirmado por TEM y DFM.

La inyección de las GNSs en un tejido muestra el aumento de ocntraste en la señal de OCT una vez que se ha sustraído el fondo. Esto permite la visualización de la distribución de GNSs en el tejido.

## 8.4. QDs de PbS pueden actuar como agentes de contraste duales para imagen cardiovascular

La ancha banda de absorción de los QDs de PbS permiten la excitación de su luminiscencia con el laser del OCT a 1.3 μm. Tras inyectar los QDs de PbS en la larteria, su emisión a 1,55 μm puede usarse para obtener la imagen de fluorescencia en la tercera ventana biológica. Además, las destacables propiedades de scattering de los QDs de PbS puede usarse para obtener contraste por

OCT. Los QDs de PbS son, por tanto, unos prometedores agentes de contraste para imagen de fluorescencia y OCT en enfermedades cardiovasculares.

## 8.5. Perspectivas futuras

Durante la realización de esta tesis doctoral, la técnica de OCT se ha usado fundamentalmente para evaluar el potencial usal de NPs como agentes de contraste para imagen cardiovascular. Se ha desarrollado además un sistema de DFM para seguir el proceso de internalización de las NPs en las células.

Respecto a las futuras aplicaciones de los agentes de contraste que se han usado en esta tesis, sus propiedades fundamentales han sido demostradas. El trabajo futuro deberá estar encaminado a la funcionalización de estos agentes de contraste con ligandos específicos, de forma que se dirijan específicamente a regiones patológicas, y a la evaluación de dichos agentes de contraste en imágenes in vivo y *ex vivo* de procesos de ateroesclerosis con medidas de OCT, fluorescencia y fotoacústico.

Es necesario el desarrollo de más agentes de contraste con un scattering mayor que el de los GNSs. Además, debido al fuerte scattering que se produce en las paredes de la arteria, sería interesante el desarrollo de agentes e contraste basados en la absorción de luz, de forma que creen un contraste negativo en la arteria, disminuyendo la señal de OCT e indicando la localización de sitios patológicos en la arteria.

Debido al sistema de IV-OCT acoplado en un catéter, la fluorescencia de las NPs puede ser recogida por el mismo catéter. De este modo, el problema de la baja penetración de la fluorescencia puede resolverse. Un sistema combinado de OCT y fluorescencia debe ser usado para el estudio de enfermedades cardiovasculares.

# References


1. Development Organisation for Economic Co-Operation and. Health Status. 2018.http://stats.oecd.org/index.aspx?DataSetCode=HEALTH_STAT# (9 May 2018).

2. Libby Peter, Ridker Paul M and Hansson Göran K. Progress and challenges in translating the biology of atherosclerosis. *Nature*. 2011;473:317-325.

3. Moore Kathryn J and Tabas Ira. Macrophages in the pathogenesis of atherosclerosis. *Cell*. 2011;145:341-355.

4. Zhang Jia, Zu Yujiao, Dhanasekara Chathurika S, Li Jun, Wu Dayong, Fan Zhaoyang and Wang Shu. Detection and treatment of atherosclerosis using nanoparticles. *Wiley Interdiscip Rev: Nanomed Nanobiotechnol*. 2017;9:e1412.

5. Tabas Ira, Williams Kevin Jon and Borén Jan. Subendothelial lipoprotein retention as the initiating process in atherosclerosis. *Circulation*. 2007;116:1832-1844.

6. Sanz Javier and Fayad Zahi A. Imaging of atherosclerotic cardiovascular disease. *Nature*. 2008;451:953-957.

7. Mestas Javier and Ley Klaus. Monocyte-endothelial cell interactions in the development of atherosclerosis. *Trends in cardiovascular medicine*. 2008;18:228-232.

8. Tabas Ira. Macrophage death and defective inflammation resolution in atherosclerosis. *Nat Rev Immunol*. 2010;10:36-46.

9. Peiser Leanne, Mukhopadhyay Subhankar and Gordon Siamon. Scavenger receptors in innate immunity. *Curr Opin Immunol*. 2002;14:123-128.

10. Järveläinen Hannu, Sainio Annele, Koulu Markku, Wight Thomas N and Penttinen Risto. Extracellular matrix molecules: potential targets in pharmacotherapy. *Pharmacological reviews*. 2009;61:198-223.

11. Peng Wen-jia, Yan Jun-wei, Wan Ya-nan, Wang Bing-xiang, Tao Jin-hui, Yang Guo-jun, Pan Hai-feng and Wang Jing. Matrix metalloproteinases: a review of their structure and role in systemic sclerosis. *Journal of clinical immunology*. 2012;32:1409-1414.

12. Liu Jian, Sukhova Galina K, Sun Jiu-Song, Xu Wei-Hua, Libby Peter and Shi Guo-Ping. Lysosomal cysteine proteases in atherosclerosis. *Arterioscler, Thromb, Vasc Biol*. 2004;24:1359-1366.

13. Jones Charles B, Sane David C and Herrington David M. Matrix metalloproteinases: a review of their structure and role in acute coronary syndrome. *Cardiovasc Res*. 2003;59:812-823.

14. Hansson Göran K. Inflammation, atherosclerosis, and coronary artery disease. *N Engl J Med*. 2005;352:1685-1695.

15. Jaffer Farouc A and Weissleder Ralph. Molecular imaging in the clinical arena. *Jama*. 2005;293:855-862.

16. Wang Xiaowei and Peter Karlheinz. Molecular Imaging of Atherothrombotic DiseasesHighlights. *Arterioscler, Thromb, Vasc Biol*. 2017;37:1029-1040.

17. Schlesinger Martin and Bendas Gerd. Vascular cell adhesion molecule‐1 (VCAM‐1)—An increasing insight into its role in tumorigenicity and metastasis. *Int J Cancer*. 2015;136:2504-2514.

18. Han Sung Gu, Newsome Bradley and Hennig Bernhard. Titanium dioxide nanoparticles increase inflammatory responses in vascular endothelial cells. *Toxicology*. 2013;306:1-8.

19. Wen Song, Liu Dong-Fang, Cui Ying, Harris Steven Scott, Chen Yu-chen, Li King C, Ju Sheng-hong and Teng Gao-Jun. In vivo MRI detection of carotid atherosclerotic lesions and kidney inflammation in ApoE-deficient mice by using LOX-1 targeted iron nanoparticles. *Nanomedicine*. 2014;10:639-649.

20. Jaffer Farouc A, Libby Peter and Weissleder Ralph. Molecular and cellular imaging of atherosclerosis. *J Am Coll Cardiol*. 2006;47:1328-1338.

21. Huang D, Swanson EA, Lin CP, Schuman JS, Stinson WG, Chang W, Hee MR, Flotte T, Gregory K and Puliafito CA. Optical coherence tomography. *Science*. 1991;254:1178-1181.

22. Drexler Wolfgang, Morgner Uwe, Ghanta Ravi K, Kärtner Franz X, Schuman Joel S and Fujimoto James G. Ultrahigh-resolution ophthalmic optical coherence tomography. *Nat Med*. 2001;7:502-507.

23. Fujimoto James G. Optical coherence tomography for ultrahigh resolution in vivo imaging. *Nat Biotech*. 2003;21:1361-1367.

24. Bezerra Hiram G, Costa Marco A, Guagliumi Giulio, Rollins Andrew M and Simon Daniel I. Intracoronary optical coherence tomography: a comprehensive review: clinical and research applications. *JACC Cardiovasc Intv*. 2009;2:1035-1046.

25. Jia Yali, Bailey Steven T, Hwang Thomas S, McClintic Scott M, Gao Simon S, Pennesi Mark E, Flaxel Christina J, Lauer Andreas K, Wilson David J and Hornegger Joachim. Quantitative optical coherence tomography angiography of vascular abnormalities in the living human eye. *Proc Natl Acad Sci*. 2015;112:E2395-E2402.

26. Yabushita Hiroshi, Bouma Brett E, Houser Stuart L, Aretz H Thomas, Jang Ik-Kyung, Schlendorf Kelly H, Kauffman Christopher R, Shishkov Milen, Kang Dong-Heon and Halpern Elkan F. Characterization of human atherosclerosis by optical coherence tomography. *Circulation*. 2002;106:1640-1645.

27. Phipps Jennifer E, Hoyt Taylor, Milner Thomas E and Feldman Marc D. Translating intravascular optical coherence tomography from a research to a clinical tool. *Curr Cardiovasc Imaging Rep*. 2015;8:30.

28. Burke Allen P, Farb Andrew, Malcom Gray T, Liang You-hui, Smialek John and Virmani Renu. Coronary risk factors and plaque morphology in men with coronary disease who died suddenly. *N Engl J Med*. 1997;336:1276-1282.

29. Chia Stanley, Raffel Owen Christopher, Takano Masamichi, Tearney Guillermo J, Bouma Brett E and Jang Ik-Kyung. Association of statin therapy with reduced coronary plaque rupture: an optical coherence tomography study. *Coronary artery disease*. 2008;19:237-242.

30. Xu Chenyang, Schmitt Joseph M, Carlier Stephane G and Virmani Renu. Characterization of atherosclerosis plaques by measuring both backscattering and attenuation coefficients in optical coherence tomography. *J Biomed Opt*. 2008;13:034003.

31. Libby Peter, Ridker Paul M and Maseri Attilio. Inflammation and atherosclerosis. *Circulation*. 2002;105:1135-1143.

32. Tearney Guillermo J, Yabushita Hiroshi, Houser Stuart L, Aretz H Thomas, Jang Ik-Kyung, Schlendorf Kelly H, Kauffman Christopher R, Shishkov Milen, Halpern Elkan F and Bouma Brett E. Quantification of macrophage content in atherosclerotic plaques by optical coherence tomography. *Circulation*. 2003;107:113-119.

33. Di Vito Luca, Agozzino Manuela, Marco Valeria, Ricciardi Andrea, Concardi Monica, Romagnoli Enrico, Gatto Laura, Calogero Giordano, Tavazzi Luigi and Arbustini Eloisa. Identification and quantification of macrophage presence in coronary atherosclerotic plaques by optical coherence tomography. *European Heart Journal-Cardiovascular Imaging*. 2015;16:807-813.

34. Phipps Jennifer E, Vela Deborah, Hoyt Taylor, Halaney David L, Mancuso J Jacob, Buja L Maximilian, Asmis Reto, Milner Thomas E and Feldman Marc D. Macrophages and intravascular OCT bright spots: a quantitative study. *JACC Cardiovasc Imaging*. 2015;8:63-72.

35. Lowe Harry C, Narula Jagat, Fujimoto James G and Jang Ik-Kyung. Intracoronary optical diagnostics: current status, limitations, and potential. *JACC Cardiovasc Intv*. 2011;4:1257-1270.

36. Bouma B. E., Tearney G. J., Yabushita H., Shishkov M., Kauffman C. R., DeJoseph Gauthier D., MacNeill B. D., Houser S. L., Aretz H. T., Halpern E. F. and Jang I. K. Evaluation of intracoronary stenting by intravascular optical coherence tomography. *Heart*. 2003;89:317-320.

37. Xu Minghua and Wang Lihong V. Photoacoustic imaging in biomedicine. *Rev Sci Instrum*. 2006;77:041101.

38. Jansen Krista, van Soest Gijs and van der Steen Antonius FW. Intravascular photoacoustic imaging: a new tool for vulnerable plaque identification. *Ultrasound in medicine and biology*. 2014;40:1037-1048.

39. Luke Geoffrey P, Yeager Doug and Emelianov Stanislav Y. Biomedical applications of photoacoustic imaging with exogenous contrast agents. *Annals of biomedical engineering*. 2012;40:422-437.

40. Laufer Jan, Delpy Dave, Elwell Clare and Beard Paul. Quantitative spatially resolved measurement of tissue chromophore concentrations using photoacoustic spectroscopy: application to the measurement of blood oxygenation and haemoglobin concentration. *Phys Med Biol*. 2007;52:141-168.

41. Laufer J, Zhang EZABPC and Beard P. Quantitative in-vivo measurements of blood oxygen saturation using multiwavelength photoacoustic imaging. *Photons Plus Ultrasound: Imaging and Sensing 2007: The Eighth Conference on Biomedical Thermoacoustics, Optoacoustics, and Acousto-optics*. 2007;6437:64371Z.

42. Beard Paul. Biomedical photoacoustic imaging. *Interface Focus*. 2011:rsfs20110028.

43. Wang Lihong V. Prospects of photoacoustic tomography. *Medical physics*. 2008;35:5758-5767.

44. Kruger Robert A, Lam Richard B, Reinecke Daniel R, Del Rio Stephen P and Doyle Ryan P. Photoacoustic angiography of the breast. *Medical physics*. 2010;37:6096-6100.

45. Wang Bo, Su Jimmy L, Amirian James, Litovsky Silvio H, Smalling Richard and Emelianov Stanislav. Detection of lipid in atherosclerotic vessels using ultrasound-guided spectroscopic intravascular photoacoustic imaging. *Opt Express*. 2010;18:4889-4897.

46. Li Wanwan and Chen Xiaoyuan. Gold nanoparticles for photoacoustic imaging. *Nanomedicine*. 2015;10:299-320.

47. Sangha Gurneet S and Goergen Craig J. Photoacoustic tomography: applications for atherosclerosis imaging. *Journal of Optics*. 2016;18:084005.

48. Qin Huan, Zhao Yue, Zhang Jian, Pan Xiao, Yang Sihua and Xing Da. Inflammation-targeted gold nanorods for intravascular photoacoustic imaging detection of matrix metalloproteinase-2 (MMP2) in atherosclerotic plaques. *Nanomedicine*. 2016;12:1765-1774.

49. Hillman Elizabeth M. C., Amoozegar Cyrus B., Wang Tracy, McCaslin Addason F. H., Bouchard Matthew B., Mansfield James and Levenson Richard M. *In vivo* optical imaging and dynamic contrast methods for biomedical research. *Philosophical Transactions of the Royal Society A: Mathematical, Physical and Engineering Sciences*. 2011;369:4620-4643.

50. Ntziachristos Vasilis, Bremer Christoph and Weissleder Ralph. Fluorescence imaging with near-infrared light: new technological advances that enable in vivo molecular imaging. *European radiology*. 2003;13:195-208.

51. Jaque D, Maestro L Martinez, Del Rosal B, Haro-Gonzalez P, Benayas A, Plaza JL, Rodriguez E Martin and Sole J Garcia. Nanoparticles for photothermal therapies. *Nanoscale*. 2014;6:9494-9530.

52. Hemmer Eva, Benayas Antonio, Légaré François and Vetrone Fiorenzo. Exploiting the biological windows: current perspectives on fluorescent bioprobes emitting above 1000 nm. *Nanoscale Horiz*. 2016;1:168-184.

53. Frangioni John V. In vivo near-infrared fluorescence imaging. *Curr Opin Chem Biol*. 2003;7:626-634.

54. Rao Jianghong, Dragulescu-Andrasi Anca and Yao Hequan. Fluorescence imaging in vivo: recent advances. *Curr Opin Biotechnol*. 2007;18:17-25.

55. Hong Guosong, Antaris Alexander L and Dai Hongjie. Near-infrared fluorophores for biomedical imaging. *Nat Biomed Eng*. 2017;1:0010.

56. Jaffer Farouc A, Vinegoni Claudio, John Michael C, Aikawa Elena, Gold Herman K, Finn Aloke V, Ntziachristos Vasilis, Libby Peter and Weissleder Ralph. Real-time catheter molecular sensing of inflammation in proteolytically active atherosclerosis. *Circulation*. 2008;118:1802-1809.

57. Jaffer Farouc A, Calfon Marcella A, Rosenthal Amir, Mallas Georgios, Razansky R Nika, Mauskapf Adam, Weissleder Ralph, Libby Peter and Ntziachristos Vasilis. Two-dimensional intravascular near-infrared fluorescence molecular imaging of inflammation in atherosclerosis and stent-induced vascular injury. *J Am Coll Cardiol*. 2011;57:2516-2526.

58. Dweck Marc R, Doris Mhairi K, Motwani Manish, Adamson Philip D, Slomka Piotr, Dey Damini, Fayad Zahi A, Newby David E and Berman Daniel. Imaging of coronary atherosclerosis—evolution towards new treatment strategies. *Nature Reviews Cardiology*. 2016;13:533-548.

59. Vinegoni Claudio, Botnaru Ion, Aikawa Elena, Calfon Marcella A, Iwamoto Yoshiko, Folco Eduardo J, Ntziachristos Vasilis, Weissleder Ralph, Libby Peter and Jaffer Farouc A. Indocyanine green enables near-infrared fluorescence imaging of lipid-rich, inflamed atherosclerotic plaques. *Science translational medicine*. 2011;3:84ra45.

60. Yoo Hongki, Kim Jin Won, Shishkov Milen, Namati Eman, Morse Theodore, Shubochkin Roman, McCarthy Jason R, Ntziachristos Vasilis, Bouma Brett E and Jaffer Farouc A. Intra-arterial catheter for simultaneous microstructural and molecular imaging in vivo. *Nat Med*. 2011;17:1680-1684.

61. Padmanabhan Parasuraman, Kumar Ajay, Kumar Sundramurthy, Chaudhary Ravi Kumar and Gulyás Balázs. Nanoparticles in practice for molecular-imaging applications: An overview. *Acta Biomaterialia*. 2016;41:1-16.

62. Brigger Irene, Dubernet Catherine and Couvreur Patrick. Nanoparticles in cancer therapy and diagnosis. *Adv Drug Delivery Rev*. 2012;64:24-36.

63. Saraste Antti, Nekolla Stephan G and Schwaiger Markus. Cardiovascular molecular imaging: an overview. *Cardiovasc Res*. 2009;83:643-652.

64. Chen Ian Y and Wu Joseph C. Cardiovascular molecular imaging: focus on clinical translation. *Circulation*. 2011;123:425-443.

65. Sinusas Albert J, Bengel Frank, Nahrendorf Matthias, Epstein Frederick H, Wu Joseph C, Villanueva Flordeliza S, Fayad Zahi A and Gropler Robert J. Multimodality cardiovascular molecular imaging, part I. *Circ Cardiovasc Imaging*. 2008;1:244-256.

66. Nguyen Luong TH, Muktabar Aristo, Tang Jinkai, Dravid Vinayak P, Thaxton C Shad, Venkatraman Subbu and Ng Kee Woei. Engineered nanoparticles for the detection, treatment and prevention of atherosclerosis: how close are we? *Drug Discovery Today*. 2017;22:1438-1446.

67. Mulder Willem JM, Jaffer Farouc A, Fayad Zahi A and Nahrendorf Matthias. Imaging and nanomedicine in inflammatory atherosclerosis. *Science translational medicine*. 2014;6:239sr1.

68. Cicha Iwona, Lyer Stefan, Alexiou Christoph and Garlichs Christoph D. Nanomedicine in diagnostics and therapy of cardiovascular diseases: beyond atherosclerotic plaque imaging. *Nanotechnol Rev*. 2013;2:449-472.

69. Varna Mariana, Xuan Hoa V and Fort Emmanuel. Gold nanoparticles in cardiovascular imaging. *Wiley Interdiscip Rev: Nanomed Nanobiotechnol*. 2018;10:e1470.

70. Liz-Marzán Luis M. Nanometals: formation and color. *Mater Today*. 2004;7:26-31.

71. Link Stephan, Mohamed MB and El-Sayed MA. Simulation of the optical absorption spectra of gold nanorods as a function of their aspect ratio and the effect of the medium dielectric constant. *The Journal of Physical Chemistry B*. 1999;103:3073-3077.

72. Mayer Kathryn M and Hafner Jason H. Localized surface plasmon resonance sensors. *Chem Rev*. 2011;111:3828-3857.

73. Mie Gustav. Beiträge zur Optik trüber Medien, speziell kolloidaler Metallösungen. *Annalen der physik*. 1908;330:377-445.

74. Gans R. Über die form ultramikroskopischer silberteilchen. *Annalen der Physik*. 1915;352:270-284.

75. Zhao Jing, Pinchuk Anatoliy O, McMahon Jeffrey M, Li Shuzhou, Ausman Logan K, Atkinson Ariel L and Schatz George C. Methods for describing the electromagnetic properties of silver and gold nanoparticles. *Acc Chem Res*. 2008;41:1710-1720.

76. Draine Bruce T and Flatau Piotr J. Discrete-dipole approximation for scattering calculations. *JOSA A*. 1994;11:1491-1499.

77. Jain Prashant K, Lee Kyeong Seok, El-Sayed Ivan H and El-Sayed Mostafa A. Calculated absorption and scattering properties of gold nanoparticles of different size, shape, and composition: applications in biological imaging and biomedicine. *The journal of physical chemistry B*. 2006;110:7238-7248.

78. Dykman Lev and Khlebtsov Nikolai. Gold nanoparticles in biomedical applications: recent advances and perspectives. *Chem Soc Rev*. 2012;41:2256-2282.

79. Huang Xiaohua, Neretina Svetlana and El ‐ Sayed Mostafa A. Gold nanorods: from synthesis and properties to biological and biomedical applications. *Adv Mater*. 2009;21:4880-4910.

80. Amendola Vincenzo, Pilot Roberto, Frasconi Marco, Maragò Onofrio M and Iatì Maria Antonia. Surface plasmon resonance in gold nanoparticles: a review. *J Phys: Condens Matter*. 2017;29:203002.

81. Zerda Adam, Prabhulkar Shradha, Perez Victor L, Ruggeri Marco, Paranjape Amit S, Habte Frezghi, Gambhir Sanjiv S and Awdeh Richard M. Optical coherence contrast imaging using gold nanorods in living mice eyes. *Clin Exp Ophthalmol*. 2015;43:358-366.

82. Chen Jingyi, Saeki Fusayo, Wiley Benjamin J, Cang Hu, Cobb Michael J, Li Zhi-Yuan, Au Leslie, Zhang Hui, Kimmey Michael B and Li Xingde. Gold nanocages: bioconjugation and their potential use as optical imaging contrast agents. *Nano Lett*. 2005;5:473-477.

83. Gao Xiaohu, Cui Yuanyuan, Levenson Richard M, Chung Leland WK and Nie Shuming. In vivo cancer targeting and imaging with semiconductor quantum dots. *Nat Biotech*. 2004;22:969.

84. Michalet X, Pinaud FF, Bentolila LA, Tsay JM, Doose SJJL, Li JJ, Sundaresan G, Wu AM, Gambhir SS and Weiss S. Quantum dots for live cells, in vivo imaging, and diagnostics. *Science*. 2005;307:538-544.

85. Valizadeh Alireza, Mikaeili Haleh, Samiei Mohammad, Farkhani Samad Mussa, Zarghami Nosratalah, Akbarzadeh Abolfazl and Davaran Soodabeh. Quantum dots: synthesis, bioapplications, and toxicity. *Nanoscale Res Lett*. 2012;7:480.

86. Wolfbeis Otto S. An overview of nanoparticles commonly used in fluorescent bioimaging. *Chem Soc Rev*. 2015;44:4743-4768.

87. Burda Clemens, Chen Xiaobo, Narayanan Radha and El-Sayed Mostafa A. Chemistry and properties of nanocrystals of different shapes. *Chem Rev*. 2005;105:1025-1102.

88. Koole Rolf, Groeneveld Esther, Vanmaekelbergh Daniel, Meijerink Andries and de Mello Donegá Celso. Size effects on semiconductor nanoparticles *Nanoparticles*: Springer; 2014: 13-51.

89. Efros Al L and Rosen M. The electronic structure of semiconductor nanocrystals. *Annu Rev Mater Sci*. 2000;30:475-521.

90. Chukwuocha Ephrem O, Onyeaju Michael C and Harry Taylor ST. Theoretical studies on the effect of confinement on quantum dots using the brus equation. *World Journal of Condensed Matter Physics*. 2012;2:96-100.

91. Krauss Todd D. and Peterson Jeffrey J. Electronic structure and optical transitions in colloidal semiconductor nanocrystals. In: E. H. Sargent and G. Konstantatos, eds. *Colloidal Quantum Dot Optoelectronics and Photovoltaics* Cambridge: Cambridge University Press; 2013: 59-86.

92. Madelung Otfried. *Semiconductors: data handbook.* 3rd ed. New York: Springer Science & Business Media; 2012.

93. Algar W. Russ, Susumu Kimihiro, Delehanty James B. and Medintz Igor L. Semiconductor Quantum Dots in Bioanalysis: Crossing the Valley of Death. *Anal Chem*. 2011;83:8826-8837.

94. Cheng Cheng, Li Jiejie and Cheng Xiaoyu. Photoluminescence lifetime and absorption spectrum of PbS nanocrystal quantum dots. *J Lumin*. 2017;188:252-257.

95. Wegner K David and Hildebrandt Niko. Quantum dots: bright and versatile in vitro and in vivo fluorescence imaging biosensors. *Chem Soc Rev*. 2015;44:4792-4834.

96. Zhou Juan, Yang Yong and Zhang Chun-yang. Toward biocompatible semiconductor quantum dots: from biosynthesis and bioconjugation to biomedical application. *Chem Rev*. 2015;115:11669-11717.

97. Kobayashi Hisataka, Hama Yukihiro, Koyama Yoshinori, Barrett Tristan, Regino Celeste AS, Urano Yasuteru and Choyke Peter L. Simultaneous multicolor imaging of five different lymphatic basins using quantum dots. *Nano Lett*. 2007;7:1711-1716.

98. Wu Chenxin, Zhang Yejun, Li Zhen, Li Chunyan and Wang Qiangbin. A novel photoacoustic nanoprobe of ICG@ PEG-$Ag_2S$ for atherosclerosis targeting and imaging in vivo. *Nanoscale*. 2016;8:12531-12539.

99. Hong Guosong, Robinson Joshua T, Zhang Yejun, Diao Shuo, Antaris Alexander L, Wang Qiangbin and Dai Hongjie. In Vivo Fluorescence Imaging with $Ag_2S$ Quantum Dots in the Second Near‐Infrared Region. *Angew Chem*. 2012;124:9956-9959.

100. Kelley William J, Safari Hanieh, Lopez‐Cazares Genesis and Eniola‐Adefeso Omolola. Vascular‐targeted nanocarriers: design considerations and strategies for successful treatment of atherosclerosis and other vascular diseases. *Wiley Interdiscip Rev: Nanomed Nanobiotechnol*. 2016;8:909-926.

101. Blanco Elvin, Shen Haifa and Ferrari Mauro. Principles of nanoparticle design for overcoming biological barriers to drug delivery. *Nat Biotech*. 2015;33:941-951.

102. Nel Andre E, Mädler Lutz, Velegol Darrell, Xia Tian, Hoek Eric MV, Somasundaran Ponisseril, Klaessig Fred, Castranova Vince and Thompson Mike. Understanding biophysicochemical interactions at the nano–bio interface. *Nat Mater*. 2009;8:543-557.

103. Kanwar Rupinder K, Chaudhary Rajneesh, Tsuzuki Takuya and Kanwar Jagat R. Emerging engineered magnetic nanoparticulate probes for targeted MRI of atherosclerotic plaque macrophages. *Nanomedicine*. 2012;7:735-749.

104. Kooi ME, Cappendijk VC, Cleutjens KBJM, Kessels AGH, Kitslaar PJEHM, Borgers M, Frederik PM, Daemen MJAP and Van Engelshoven JMA. Accumulation of ultrasmall superparamagnetic particles of iron oxide in human atherosclerotic plaques can be detected by in vivo magnetic resonance imaging. *Circulation*. 2003;107:2453-2458.

105. Qiao Ruirui, Qiao Hongyu, Zhang Yan, Wang Yabin, Chi Chongwei, Tian Jie, Zhang Lifang, Cao Feng and Gao Mingyuan. Molecular imaging of vulnerable atherosclerotic plaques in vivo with osteopontin-specific upconversion nanoprobes. *ACS Nano*. 2017;11:1816-1825.

106. Jefferson Andrew, Wijesurendra Rohan S, McAteer Martina A, Digby Janet E, Douglas Gillian, Bannister Thomas, Perez-Balderas Francisco, Bagi Zsolt, Lindsay Alistair C and Choudhury Robin P. Molecular imaging with optical coherence tomography using ligand-conjugated microparticles that detect activated endothelial cells: rational design through target quantification. *Atherosclerosis*. 2011;219:579-587.

107. Jaffer Farouc A., Tung Ching-Hsuan, Gerszten Robert E. and Weissleder Ralph. In Vivo Imaging of Thrombin Activity in Experimental Thrombi With Thrombin-Sensitive Near-Infrared Molecular Probe. *Arterioscler, Thromb, Vasc Biol*. 2002;22:1929-1935.

108. Peters David, Kastantin Mark, Kotamraju Venkata Ramana, Karmali Priya P, Gujraty Kunal, Tirrell Matthew and Ruoslahti Erkki. Targeting atherosclerosis by using modular, multifunctional micelles. *Proc Natl Acad Sci*. 2009;106:9815-9819.

109. Wang Yabin, Chen Jiangwei, Yang Bo, Qiao Hongyu, Gao Lei, Su Tao, Ma Sai, Zhang Xiaotian, Li Xiujuan and Liu Gang. In vivo MR and fluorescence dual-modality imaging of atherosclerosis characteristics in mice using profilin-1 targeted magnetic nanoparticles. *Theranostics*. 2016;6:272-286.

110. Wu Chenxin, Zhang Yejun, Li Zhen, Li Chunyan and Wang Qiangbin. A novel photoacoustic nanoprobe of ICG@ PEG-Ag 2 S for atherosclerosis targeting and imaging in vivo. *Nanoscale*. 2016;8:12531-12539.

111. Qin Huan, Zhou Ting, Yang Sihua, Chen Qun and Xing Da. Gadolinium (III)-gold nanorods for MRI and photoacoustic imaging dual-modality detection of macrophages in atherosclerotic inflammation. *Nanomedicine*. 2013;8:1611-1624.

112. Kim Kang, Huang Sheng-Wen, Ashkenazi Shai, O'Donnell Matthew, Agarwal Ashish, Kotov Nicholas A, Denny Michael F and Kaplan Mariana J. Photoacoustic imaging of early inflammatory response using gold nanorods. *Appl Phys Lett*. 2007;90:223901.

113. Rouleau Leonie, Berti Romain, Ng Vanessa WK, Matteau‐Pelletier Carl, Lam Tina, Saboural Pierre, Kakkar Ashok K, Lesage Frédéric, Rhéaume Eric and Tardif Jean‐Claude. VCAM‐1‐targeting gold nanoshell probe for photoacoustic imaging of atherosclerotic plaque in mice. *Contrast Media Mol Imaging*. 2013;8:27-39.

114. Wang Bo, Yantsen Evgeniya, Larson Timothy, Karpiouk Andrei B, Sethuraman Shriram, Su Jimmy L, Sokolov Konstantin and Emelianov Stanislav Y. Plasmonic intravascular

photoacoustic imaging for detection of macrophages in atherosclerotic plaques. *Nano Lett*. 2009;9:2212-2217.

115. Ha Seunghan, Carson Andrew, Agarwal Ashish, Kotov Nicholas A and Kim Kang. Detection and monitoring of the multiple inflammatory responses by photoacoustic molecular imaging using selectively targeted gold nanorods. *Biomed Opt Express*. 2011;2:645-657.

116. Hu Jie, Ortgies Dirk H., Torres Rio Aguliar, Fernández Nuria, Porto Lucas, Rodríguez Emma Martín, Solé José García, Jaque Daniel, Alfonso Fernando and Rivero Fernando. Quantum Dots Emitting in the Third Biological Window as Bimodal Contrast Agents for Cardiovascular Imaging. *Adv Funct Mater*. 2017;27:1703276.

117. Paranjape Amit S, Kuranov Roman, Baranov Stepan, Ma Li Leo, Villard Joseph W, Wang Tianyi, Sokolov Konstantin V, Feldman Marc D, Johnston Keith P and Milner Thomas E. Depth resolved photothermal OCT detection of macrophages in tissue using nanorose. *Biomed Opt Express*. 2010;1:2-16.

118. Kim Jongsik, Ahmad Adeel, Li Joanne, Marjanovic Marina, Chaney Eric J, Suslick Kenneth S and Boppart Stephen A. Intravascular magnetomotive optical coherence tomography of targeted early ‐ stage atherosclerotic changes in ex vivo hyperlipidemic rabbit aortas. *J Biophotonics*. 2016;9:109-116.

119. Morishige Kunio, Kacher Daniel F, Libby Peter, Josephson Lee, Ganz Peter, Weissleder Ralph and Aikawa Masanori. High-Resolution Magnetic Resonance Imaging Enhanced With Superparamagnetic Nanoparticles Measures Macrophage Burden in AtherosclerosisClinical Perspective. *Circulation*. 2010;122:1707-1715.

120. Marrache Sean and Dhar Shanta. Biodegradable synthetic high-density lipoprotein nanoparticles for atherosclerosis. *Proc Natl Acad Sci*. 2013;110:9445-9450.

121. Yuan Hsiangkuo, Khoury Christopher G, Hwang Hanjun, Wilson Christy M, Grant Gerald A and Vo-Dinh Tuan. Gold nanostars: surfactant-free synthesis, 3D modelling, and two-photon photoluminescence imaging. *Nanotechnology*. 2012;23:075102.

122. Williams David B and Carter C Barry. The transmission electron microscope *Transmission electron microscopy*: Springer; 1996: 3-17.

123. Kregsamer Peter, Streli Christina and Wobrauschek Peter. Total reflection X-ray fluorescence. *PRACTICAL SPECTROSCOPY SERIES*. 2002;29:559-602.

124. Klockenkàmper Rinhold, Knoth Joachim, Prange Andreas and Schwenke Heinrich. Total-reflection X-ray fluorescence spectroscopy. *Anal Chem*. 1992;64:1115A-1123A.

125. del Rosal Blanca, Pérez ‐ Delgado Alberto, Carrasco Elisa, Jovanović Dragana J, Dramićanin Miroslav D, Dražić Goran, de la Fuente Ángeles Juarranz, Sanz ‐ Rodriguez Francisco and Jaque Daniel. Neodymium ‐ Based Stoichiometric Ultrasmall Nanoparticles for Multifunctional Deep-Tissue Photothermal Therapy. *Adv Opt Mater*. 2016;4:782-789.

126. Roper D Keith, Ahn Wonmi and Hoepfner M. Microscale heat transfer transduced by surface plasmon resonant gold nanoparticles. *J Phys Chem C*. 2007;111:3636-3641.

127. Izatt Joseph A, Choma Michael A and Dhalla Al-Hafeez. Theory of optical coherence tomography. In: W. Drexler and J. G. Fujimoto, eds. *Optical Coherence Tomography: Technology and Applications*: Springer, Cham; 2015: 65-94.

128. Jang Ik-Kyung, Bouma Brett E, Kang Dong-Heon, Park Seung-Jung, Park Seong-Wook, Seung Ki-Bae, Choi Kyu-Bo, Shishkov Milen, Schlendorf Kelly and Pomerantsev Eugene. Visualization of coronary atherosclerotic plaques in patients using optical coherence tomography: comparison with intravascular ultrasound. *J Am Coll Cardiol*. 2002;39:604-609.

129. Leggio Luca, Gallego Daniel, Arroyo Raul, Gawali Sandeep Babu, Rodriguez Sergio, Sánchez Miguel, Carpintero del Barrio Guillermo and Lamela Horacio. Accurate Determination of Gold Nanorods Concentrations from Optoacoustic Signals Detected at 870 nm and 905 nm by Using High-Power Diode Lasers with Fast Switching Electronics. *Prog Electromagn Res*. 2017;78:143-154.

130. Masters John R. HeLa cells 50 years on: the good, the bad and the ugly. *Nat Rev Cancer*. 2002;2:315-319.

131. Riss Terry L, Moravec Richard A, Niles Andrew L, Duellman Sarah, Benink Hélène A, Worzella Tracy J and Minor Lisa. Cell viability assays *Assay Guidance Manual* Bethesda: Eli Lilly & Company and the National Center for Advancing Translational Sciences; 2016: 355-386.

132. Ehlers Justis P, Gupta Preeya K, Farsiu Sina, Maldonado Ramiro, Kim Terry, Toth Cynthia A and Mruthyunjaya Prithvi. Evaluation of contrast agents for enhanced visualization in optical coherence tomography. *Invest Ophthalmol Visual Sci*. 2010;51:6614-6619.

133. Barton Jennifer Kehlet, Hoying James B and Sullivan Chris J. Use of microbubbles as an optical coherence tomography contrast agent. *Acad Radiol*. 2002;9:S52-S55.

134. Dreaden Erik C, Alkilany Alaaldin M, Huang Xiaohua, Murphy Catherine J and El-Sayed Mostafa A. The golden age: gold nanoparticles for biomedicine. *Chem Soc Rev*. 2012;41:2740-2779.

135. Pérez-Juste Jorge, Pastoriza-Santos Isabel, Liz-Marzán Luis M and Mulvaney Paul. Gold nanorods: synthesis, characterization and applications. *Coord Chem Rev*. 2005;249:1870-1901.

136. Van Hoecke Karen, De Schamphelaere KAC, Ali Zulqurnain, Zhang Feng, Elsaesser Andreas, Rivera-Gil Pilar, Parak WJ, Smagghe Guy, Howard CV and Janssen CR. Ecotoxicity and uptake of polymer coated gold nanoparticles. *Nanotoxicology*. 2013;7:37-47.

137. Rivera_Gil Pilar, Vazquez-Vazquez Carmen, Giannini Vincenzo, Callao M Pilar, Parak Wolfgang J, Correa-Duarte Miguel A and Alvarez-Puebla Ramon A. Plasmonic Nanoprobes for Real‐Time Optical Monitoring of Nitric Oxide inside Living Cells. *Angew Chem Int Ed*. 2013;52:13694-13698.

138. Zamora-Perez Paula, Tsoutsi Dionysia, Xu Ruixue and Rivera_Gil Pilar. Hyperspectral-Enhanced Dark Field Microscopy for Single and Collective Nanoparticle Characterization in Biological Environments. *Materials*. 2018;11:243.

139. Dionysia Tsoutsi, Marcos Sanles-Sobrido, Andreu Cabo and Pilar Rivera Gil. Common aspects influencing the translocation of SERS to Biomedicine. *Curr Med Chem*. 2018;25:1-15.

140. Hainfeld JF, Slatkin DN, Focella TM and Smilowitz HM. Gold nanoparticles: a new X-ray contrast agent. *Br J Radiol*. 2006;79:248-253.

141. Kim Dongkyu, Park Sangjin, Lee Jae Hyuk, Jeong Yong Yeon and Jon Sangyong. Antibiofouling polymer-coated gold nanoparticles as a contrast agent for in vivo X-ray computed tomography imaging. *J Am Chem Soc*. 2007;129:7661-7665.

142. Chhour Peter, Naha Pratap C, O'Neill Sean M, Litt Harold I, Reilly Muredach P, Ferrari Victor A and Cormode David P. Labeling monocytes with gold nanoparticles to track their recruitment in atherosclerosis with computed tomography. *Biomaterials*. 2016;87:93-103.

143. Oldenburg Amy L, Hansen Matthew N, Zweifel Daniel A, Wei Alexander and Boppart Stephen A. Plasmon-resonant gold nanorods as low backscattering albedo contrast agents. *Opt Express*. 2006;14:6724-6738.

144. Muskens Otto L, Bachelier Guillaume, Fatti Natalia Del, Vallee Fabrice, Brioude Arnaud, Jiang Xuchuan and Pileni Marie-Paule. Quantitative absorption spectroscopy of a single gold nanorod. *J Phys Chem C*. 2008;112:8917-8921.

145. Gudjonson Herman, Kats Mikhail A, Liu Kun, Nie Zhihong, Kumacheva Eugenia and Capasso Federico. Accounting for inhomogeneous broadening in nano-optics by electromagnetic modeling based on Monte Carlo methods. *Proc Natl Acad Sci*. 2014;111:E639-E644.

146. Oldenburg Steven J, Jackson Joseph B, Westcott Sarah L and Halas NJ. Infrared extinction properties of gold nanoshells. *Appl Phys Lett*. 1999;75:2897-2899.

147. Nehl Colleen L, Grady Nathaniel K, Goodrich Glenn P, Tam Felicia, Halas Naomi J and Hafner Jason H. Scattering spectra of single gold nanoshells. *Nano Lett*. 2004;4:2355-2359.

148. Agrawal Anant, Huang Stanley, Lin Alex Wei Han, Lee Min-Ho, Barton Jennifer Kehlet, Drezek Rebekah Anna and Pfefer Joshua. Quantitative evaluation of optical coherence tomography signal enhancement with gold nanoshells. *J Biomed Opt*. 2006;11:041121.

149. Gobin André M, Lee Min Ho, Halas Naomi J, James William D, Drezek Rebekah A and West Jennifer L. Near-infrared resonant nanoshells for combined optical imaging and photothermal cancer therapy. *Nano Lett*. 2007;7:1929-1934.

150. Maestro Laura Martínez, Haro-González Patricia, Coello Jose Garcia and Jaque Daniel. Absorption efficiency of gold nanorods determined by quantum dot fluorescence thermometry. *Appl Phys Lett*. 2012;100:201110.

151. Kah James Chen-Yong, Olivo Malini C, Chow Tzu Hao, San Song Kin, Koh Karen Zhen Yu, Mhaisalkar Subodh and Sheppard Colin. Control of optical contrast using gold nanoshells for optical coherence tomography imaging of mouse xenograft tumor model in vivo. *J Biomed Opt*. 2009;14:054015.

152. Yi Ji, Radosevich Andrew J, Rogers Jeremy D, Norris Sam CP, Çapoğlu İlker R, Taflove Allen and Backman Vadim. Can OCT be sensitive to nanoscale structural alterations in biological tissue? *Opt Express*. 2013;21:9043-9059.

153. Alexandrov Sergey, Subhash Hrebesh and Leahy Martin. Nanosensitive optical coherence tomography for the study of changes in static and dynamic structures. *Quantum Electron*. 2014;44:657.

154. Alexandrov Sergey A, Subhash Hrebesh M, Zam Azhar and Leahy Martin. Nano-sensitive optical coherence tomography. *Nanoscale*. 2014;6:3545-3549.

155. Liu Yang, Ashton Jeffrey R, Moding Everett J, Yuan Hsiangkuo, Register Janna K, Fales Andrew M, Choi Jaeyeon, Whitley Melodi J, Zhao Xiaoguang and Qi Yi. A plasmonic gold nanostar theranostic probe for in vivo tumor imaging and photothermal therapy. *Theranostics*. 2015;5:946-960.

156. Cheng Fong-Yu, Chen Chen-Tai and Yeh Chen-Sheng. Comparative efficiencies of photothermal destruction of malignant cells using antibody-coated silica@ Au nanoshells, hollow Au/Ag nanospheres and Au nanorods. *Nanotechnology*. 2009;20:425104.

157. Chen Huanjun, Shao Lei, Ming Tian, Sun Zhenhua, Zhao Chunmei, Yang Baocheng and Wang Jianfang. Understanding the photothermal conversion efficiency of gold nanocrystals. *Small*. 2010;6:2272-2280.

158. Pattani Varun P and Tunnell James W. Nanoparticle‐mediated photothermal therapy: A comparative study of heating for different particle types. *Lasers Surg Med*. 2012;44:675-684.

159. Wojtkowski Maciej, Kowalczyk A, Leitgeb R and Fercher AF. Full range complex spectral optical coherence tomography technique in eye imaging. *Opt Lett*. 2002;27:1415-1417.

160. Drexler Wolfgang and Fujimoto James G. State-of-the-art retinal optical coherence tomography. *Prog Retinal Eye Res*. 2008;27:45-88.

161. Cole Joseph R, Mirin Nikolay A, Knight Mark W, Goodrich Glenn P and Halas Naomi J. Photothermal efficiencies of nanoshells and nanorods for clinical therapeutic applications. *J Phys Chem C*. 2009;113:12090-12094.

162. Rodríguez-Oliveros R and Sánchez-Gil José A. Gold nanostars as thermoplasmonic nanoparticles for optical heating. *Opt Express*. 2012;20:621-626.

163. Rodríguez-Oliveros Rogelio, Paniagua-Domínguez Ramón, Sánchez-Gil José A and Macías Demetrio. Plasmon spectroscopy: Theoretical and numerical calculations, and optimization techniques. *Nanospectroscopy*. 2014;1:67-96.

164. Marciniak Lukasz, Pilch Aleksandra, Arabasz Sebastian, Jin Dayong and Bednarkiewicz Artur. Heterogeneously $Nd^{3+}$ doped single nanoparticles for NIR-induced heat conversion, luminescence, and thermometry. *Nanoscale*. 2017;9:8288-8297.

165. Hu Min, Novo Carolina, Funston Alison, Wang Haining, Staleva Hristina, Zou Shengli, Mulvaney Paul, Xia Younan and Hartland Gregory V. Dark-field microscopy studies of single metal nanoparticles: understanding the factors that influence the linewidth of the localized surface plasmon resonance. *J Mater Chem*. 2008;18:1949-1960.

166. Reid MT Homer and Johnson Steven G. Efficient computation of power, force, and torque in BEM scattering calculations. *IEEE Trans Antennas Propag*. 2015;63:3588-3598.

167. Ungureanu C, Gopal R Raja, van Leeuwen TG and Manohar Srirang. Optical properties of gold nanorods: towards contrast agents for Photoacoustic imaging. *Phys Rev B*. 1972;6:4370-4379.

168. Prodan E, Nordlander P and Halas NJ. Electronic structure and optical properties of gold nanoshells. *Nano Lett*. 2003;3:1411-1415.

169. Westcott S. L., Jackson J. B., Radloff C. and Halas N. J. Relative contributions to the plasmon line shape of metal nanoshells. *Phys Rev B*. 2002;66:155431.

170. Cunningham Vincent B, Lamela Horacio and Gallego Daniel C. Laser optoacoustic scheme for highly accurate characterization of gold nanostructures in liquid phantoms for biomedical applications. *J Nanophotonics*. 2013;7:073078.

171. Cox Benjamin T, Laufer Jan G, Beard Paul C and Arridge Simon R. Quantitative spectroscopic photoacoustic imaging: a review. *J Biomed Opt*. 2012;17:061202.

172. Kennedy Brendan F., Kennedy Kelsey M., Oldenburg Amy L., Adie Steven G., Boppart Stephen A. and Sampson David D. Optical Coherence Elastography. In: W. Drexler and J. G. Fujimoto, eds. *Optical Coherence Tomography: Technology and Applications* Cham: Springer International Publishing; 2015: 1007-1054.

173. Alfonso Fernando, Dutary Jaime, Paulo Manuel, Gonzalo Nieves, Pérez-Vizcayno Maria J, Jiménez-Quevedo Pilar, Escaned Javier, Bañuelos Camino, Hernández Rosana and Macaya Carlos. Combined use of optical coherence tomography and intravascular ultrasound imaging in patients undergoing coronary interventions for stent thrombosis. *Heart*. 2012;98:1213-1220.

174. Prati Francesco, Stazi Filippo, Dutary Jaime, La Manna Alessio, Di Giorgio Alessandro, Pawlosky Tomasz, Gonzalo Nieves, Di Salvo Maria Elena, Imola Fabrizio and Tamburino Corrado. Detection of very early stent healing after primary angioplasty: an optical coherence tomographic observational study of chromium cobaltum and first-generation drug-eluting stents. The DETECTIVE study. *Heart*. 2011;97:1841-1846.

175. Rivero Fernando, Bastante Teresa, Cuesta Javier, Benedicto Amparo, Restrepo Jorge A and Alfonso Fernando. Treatment of in-stent restenosis with bioresorbable vascular scaffolds: optical coherence tomography insights. *Can J Cardiol*. 2015;31:255-259.

176. Douma Kim, Prinzen Lenneke, Slaaf Dick W, Reutelingsperger Chris PM, Biessen Erik AL, Hackeng Tilman M, Post Mark J and van Zandvoort Marc AMJ. Nanoparticles for optical molecular imaging of atherosclerosis. *Small*. 2009;5:544-557.

177. Bibikova Olga, Popov Alexey, Bykov Alexander, Prilepskii Artur, Kinnunen Matti, Kordas Krisztian, Bogatyrev Vladimir, Khlebtsov Nikolai, Vainio Seppo and Tuchin Valery. Optical properties of plasmon-resonant bare and silica-coated nanostars used for cell imaging. *J Biomed Opt*. 2015;20:076017.

178. Skrabalak Sara E, Chen Jingyi, Au Leslie, Lu Xianmao, Li Xingde and Xia Younan. Gold nanocages for biomedical applications. *Adv Mater*. 2007;19:3177-3184.

179. Hu Jie, Rivero Fernando, Torres Rio Aguilar, Loro Ramírez Héctor, Rodríguez Emma Martín, Alfonso Fernando, García Solé José and Jaque Daniel. Dynamic single gold nanoparticle visualization by clinical intracoronary optical coherence tomography. *J Biophotonics*. 2017;10:674-682.

180. Skala Melissa C, Crow Matthew J, Wax Adam and Izatt Joseph A. Photothermal optical coherence tomography of epidermal growth factor receptor in live cells using immunotargeted gold nanospheres. *Nano Lett*. 2008;8:3461-3467.

181. Loo Christopher, Lowery Amanda, Halas Naomi, West Jennifer and Drezek Rebekah. Immunotargeted nanoshells for integrated cancer imaging and therapy. *Nano Lett*. 2005;5:709-711.

182. De León Y Ponce, Pichardo-Molina JL, Ochoa N Alcalá and Luna-Moreno D. Contrast enhancement of optical coherence tomography images using branched gold nanoparticles. *J Nanomater*. 2012;2012:128.

183. Adler Desmond C, Huang Shu-Wei, Huber Robert and Fujimoto James G. Photothermal detection of gold nanoparticles using phase-sensitive optical coherence tomography. *Opt Express*. 2008;16:4376-4393.

184. Fratoddi Ilaria, Venditti Iole, Cametti Cesare and Russo Maria Vittoria. How toxic are gold nanoparticles? The state-of-the-art. *Nano Res*. 2015;8:1771-1799.

185. Meng X., Yang J., Dong M., Zhang K., Tu E., Gao Q., Chen W., Zhang C. and Zhang Y. Regulatory T cells in cardiovascular diseases. *Nat Rev Cardiol*. 2016;13:167-79.

186. Libby P., Lichtman A. H. and Hansson G. K. Immune effector mechanisms implicated in atherosclerosis: from mice to humans. *Immunity*. 2013;38:1092-104.

187. Li Miao, Lohmüller Theobald and Feldmann Jochen. Optical Injection of Gold Nanoparticles into Living Cells. *Nano Lett*. 2015;15:770-775.

188. Cui Yi, Wang Xiaolei, Ren Wen, Liu Jing and Irudayaraj Joseph. Optical Clearing Delivers Ultrasensitive Hyperspectral Dark-Field Imaging for Single-Cell Evaluation. *ACS Nano*. 2016;10:3132-3143.

189. Xie Xueping, Liao Jinfeng, Shao Xiaoru, Li Qianshun and Lin Yunfeng. The Effect of shape on Cellular Uptake of Gold Nanoparticles in the forms of Stars, Rods, and Triangles. *Sci Rep*. 2017;7:3827.

190. Connor Ellen E., Mwamuka Judith, Gole Anand, Murphy Catherine J. and Wyatt Michael D. Gold Nanoparticles Are Taken Up by Human Cells but Do Not Cause Acute Cytotoxicity. *Small*. 2005;1:325-327.

191. Chithrani B Devika, Ghazani Arezou A and Chan Warren CW. Determining the size and shape dependence of gold nanoparticle uptake into mammalian cells. *Nano Lett*. 2006;6:662-668.

192. Schmitt Joseph M and Kumar Gitesh. Optical scattering properties of soft tissue: a discrete particle model. *Appl Opt*. 1998;37:2788-2797.

193. Hu Jie, Sanz-Rodríguez Francisco, Rivero Fernando, Rodríguez Emma Martín, Torres Río Aguilar, Ortgies Dirk H, Solé José García, Alfonso Fernando and Jaque Daniel. Gold nanoshells: Contrast agents for cell imaging by cardiovascular optical coherence tomography. *Nano Res*. 2018;11:676-685.

194. Hara Tetsuya and Jaffer Farouc A. Intravascular NIRF Molecular Imaging Approaches in Coronary Artery Disease. *Curr Cardiovasc Imaging Rep*. 2016;9:13.

195. Lee Sunki, Lee Min Woo, Cho Han Saem, Song Joon Woo, Nam Hyeong Soo, Oh Dong Joo, Park Kyeongsoon, Oh Wang-Yuhl, Yoo Hongki and Kim Jin Won. Fully integrated high-speed intravascular optical coherence tomography/near-infrared fluorescence structural/molecular imaging in vivo using a clinically available near-infrared fluorescence–emitting indocyanine green to detect inflamed lipid-rich atheromata in coronary-sized vessels. *Circulation: Cardiovascular Interventions*. 2014;7:560-569.

196. Kim Ji Bak, Park Kyeongsoon, Ryu Jiheun, Lee Jae Joong, Lee Min Woo, Cho Han Saem, Nam Hyeong Soo, Park Ok Kyu, Song Joon Woo and Kim Tae Shik. Intravascular optical imaging of high-risk plaques in vivo by targeting macrophage mannose receptors. *Sci Rep*. 2016;6:22608.

197. Diao Shuo, Blackburn Jeffrey L, Hong Guosong, Antaris Alexander L, Chang Junlei, Wu Justin Z, Zhang Bo, Cheng Kai, Kuo Calvin J and Dai Hongjie. Fluorescence imaging in vivo at wavelengths beyond 1500 nm. *Angew Chem*. 2015;127:14971-14975.

198. Robinson Joshua T, Hong Guosong, Liang Yongye, Zhang Bo, Yaghi Omar K and Dai Hongjie. In vivo fluorescence imaging in the second near-infrared window with long circulating carbon nanotubes capable of ultrahigh tumor uptake. *J Am Chem Soc*. 2012;134:10664-10669.

199. Antaris Alexander L, Chen Hao, Cheng Kai, Sun Yao, Hong Guosong, Qu Chunrong, Diao Shuo, Deng Zixin, Hu Xianming and Zhang Bo. A small-molecule dye for NIR-II imaging. *Nat Mater*. 2016;15:235-242.

200. Bu Xiaobing, Chen Huaping, Gai Hongwei, Yang Ronghua and Yeung Edward S. Scattering Imaging of Single Quantum Dots with Dark-Field Microscopy. *Anal Chem*. 2009;81:7507-7509.

201. Schmitt Joseph M. Optical coherence tomography (OCT): a review. *IEEE J Sel Top Quantum Electron*. 1999;5:1205-1215.

202. Leatherdale Catherine A, Woo W-K, Mikulec Frederic V and Bawendi Moungi G. On the absorption cross section of CdSe nanocrystal quantum dots. *The Journal of Physical Chemistry B*. 2002;106:7619-7622.

203. Yu Pingrong, Beard Matthew C, Ellingson Randy J, Ferrere Suzanne, Curtis Calvin, Drexler John, Luiszer Fred and Nozik Arthur J. Absorption cross-section and related optical properties of colloidal InAs quantum dots. *The Journal of Physical Chemistry B*. 2005;109:7084-7087.

204. Dong Ning-Ning, Pedroni Marco, Piccinelli Fabio, Conti Giamaica, Sbarbati Andrea, Ramírez-Hernández Juan Enrique, Maestro Laura Martínez, Iglesias-de la Cruz Maria Carmen, Sanz-Rodriguez Francisco and Juarranz Angeles. NIR-to-NIR two-photon excited $CaF_2$: $Tm^{3+}$, $Yb^{3+}$ nanoparticles: multifunctional nanoprobes for highly penetrating fluorescence bio-imaging. *ACS Nano*. 2011;5:8665-8671.

205. Rocha Ueslen, Kumar Kagola Upendra, Jacinto Carlos, Villa Irene, Sanz‐Rodríguez Francisco, Juarranz Angeles, Carrasco Elisa, van Veggel Frank CJM, Bovero Enrico and Solé José García. Neodymium‐Doped $LaF_3$ Nanoparticles for Fluorescence Bioimaging in the Second Biological Window. *Small*. 2014;10:1141-1154.

206. Ruiz Diego, del Rosal Blanca, Acebrón María, Palencia Cristina, Sun Chen, Cabanillas‐González Juan, López‐Haro Miguel, Hungría Ana B, Jaque Daniel and Juarez Beatriz H. $Ag/Ag_2S$ Nanocrystals for High Sensitivity Near‐Infrared Luminescence Nanothermometry. *Adv Funct Mater*. 2017;27:1604629.

207. Quillard Thibaut and Libby Peter. Molecular imaging of atherosclerosis for improving diagnostic and therapeutic development. *Circ Res*. 2012;111:231-244.